LOW FIELD NUCLEAR SPIN OPTICAL ROTATION

A Dissertation

by

YUE ZHU

Submitted to the Office of Graduate and Professional Studies of
Texas A&M University
in partial fulfillment of the requirements for the degree of

DOCTOR OF PHILOSOPHY

Chair of Committee,	Christian Hilty
Committee Members,	Dong Hee Son
	Matthew Sheldon
	Edward Fry
Head of Department,	Simon North

December 2020

Major Subject: Chemistry

ABSTRACT

The phenomenon of Nuclear Spin Optical Rotation (NSOR) is a member of the nuclear magneto-optic effects. This is a spectroscopic phenomenon based on observing the polarization state of a light beam after it interacts with nuclei of non-zero spin magnetization. The NSOR effect relies on the hyperfine interactions between nuclear spins and electrons. Therefore, it provides the ability to extract information on electronic states at the specific nuclear sites of the molecules in samples. The most critical challenge of the NSOR experiment is its intrinsic low signal-to-noise ratio (SNR). The most straightforward way of solving this problem is to increase the polarization level of nuclear spins. In this work, by using the dissolution dynamic nuclear polarization (DNP) technique, the polarization level is increased by the order of 10^4 compared to the polarization obtained in a superconducting magnet. This increase can potentially solve the low SNR problem.

A low field NMR instrument was constructed for observing NSOR in conjunction with a dynamic nuclear polarizer. Longitudinal relaxation rates of four different concentrations of radicals were determined, and paramagnetic relaxation enhancement was quantified. The concentration of radical affected the polarization level inside the DNP polarizer and the loss during sample transfer. An optimal concentration was found to be 30 mM, which resulted in a 5 % polarization level after optimizing the injection time. This polarization level was determined to be sufficient for a single scan NSOR experiment.

NSOR signals were then obtained with a circulation system by prepolarizing the sample inside a superconducting magnet. Multi-nuclear NSOR measurement and frequency-resolved NSOR at the low field were demonstrated for the first time. In a

sample of 1:1 trifluoroethanol (TFE), water mixture containing ^{19}F and ^{1}H NSOR signals were simultaneously obtained, and the fluorine NSOR constant was determined to be 46 times larger than the proton. Triplet fluorine NSOR signal was observed due to spin-spin interactions.

Finally, NSOR signals of proton and fluorine were obtained with the dissolution DNP technique. A bubble trap and a focusing lens system minimized the negative effects of gas bubbles and variations of the refractive index of the injected DNP sample, without which the optical signal strength would be reduced. The NSOR signal was for the first time observed in a single scan, with SNR of over 6. The signal from a more than 100-fold diluted DNP sample is over 30 times larger than the signal obtained with a pure sample prepolarized by a superconducting magnet. Further optimization of sample cell geometry with the help of flow dynamics could lead to even higher SNR. With such increased SNR, the NSOR effect can potentially be applied for a hybrid optical-NMR spectroscopy, which can be used to study the local electronic excitation around a specific nucleus.

DEDICATION

To my mother, my father, and my grandmother.

ACKNOWLEDGMENTS

I am especially indebted to Dr. Christian Hilty and Dr. Igor Savukov, for their guidance through each stage of the project. Without their insights into the project, it is impossible for me to get started with this complicated project which involves many aspects that I have no experience before, such as electronics and machine works.

I also would like to thank my committee members, Dr. Dong Hee Son, Dr, Matthew Sheldon and Dr. Edward Fry.

Additionally, I'd like to thank my group members. They made it easier for me to finish the project by helping me or giving insightful suggestions. Their valuable experience also helped me understand things one step earlier in stages of doctoral program. I also owe my thanks to them by helping adapt to the lifestyle in this foreign country.

Special thanks goes to my friends. They have helped me gain strength in the hard times. Conversations with them helped me understand the life in different countries and in turn helped me in deciding my career path.

Finally, I want to thank my family for their wholehearted support and unconditional love.

CONTRIBUTORS AND FUNDING SOURCES

Contributors

This work was supported by a dissertation committee consisting of Professor Christian Hilty, Professor Dong Hee Son and Professor Matthew Sheldon of the Department of Chemistry and Professor Edward Fry of the Department of Physics.

The experiments and data analysis in Chapter 2 were conducted with the help of Chia-hsiu Chen. The shimming coil was setup by Zechariah Wilson. Electronic devices in Chapter 3 were constructed with the help of Yuheng Gao and Shane Rodocker. The NMR instrument was setup with the help of Dr. Christian Hilty and Dr. Igor Savukov. The initial Labview program for controlling the electronics was provided by Dr. Christian Hilty.

All other work conducted for the dissertation was completed by the student independently.

Funding Sources

Graduate study and this dissertation was supported from National Science Foundation (CHE-1404548 and CHE-1404529) and the Welch Foundation (A-1658).

NOMENCLATURE

NMR	Nuclear Magnetic Resonance
NSOR	Nuclear Spin Optical Rotation
SNR	Signal-to-Noise Ratio
DNP	Dynamic Nuclear Polarization
D-DNP	Dissolution Dynamic Nuclear Polarization
LF	Low Field
FFT	Fast Fourier Transform
MRI	Magnetic Resonance Imaging
O-DNP	Overhauser effect Dymanic Nuclear Ploarization
NOE	Nuclear Overhauser Effect
ABS	Acrylonitrile Butadiene Styrene
PLA	Polylactic acid
TEMPOL	4-hydroxy-2,2,6,6-tetramethylpiperidine-1-oxyl
FID	Free Induction Decay
1D	One-Dimensional
2D	Two-Dimensional
PRE	Paramagnetic Resonance Enhancement
TFE	Trifluoroenthanl
RF	Ratio Frequency
CPMG	Carr-Purcell-Meiboom-Gill

DI	Deionized
LPB	linearly polarized beam
CPB	circularly polarized beam
lCPB	left circularly polarized beam
rCPB	right circularly polarized beam
FR	Faraday Rotation
UV	Ultraviolet
EMF	Electromagnetic Field
NSCM	Nuclear Spin-Induced Cotton–Mouton

TABLE OF CONTENTS

Page

LIST OF FIGURES

FIGURE Page

LIST OF TABLES

1. INTRODUCTION *

The Nuclear Magnetic Resonance (NMR) phenomenon was first measured under high vacuum in a molecular beam by Isidor Rabi in 1938. This achievement contributed to him winning 1944 Nobel Prize. NMR in bulk materials was later, in 1946 reported by Bloch *et al.* and by Purcell *et al.* Bloch and Purcell were awarded the Nobel Prize in 1952, when the importance of their discovery became recognized. Since then, NMR spectroscopy has evolved into a major tool in chemistry and physics, which is most widely applied to determine molecular structure and also to study phenomena from reaction kinetics to superconductivity. In structural biology NMR is a technique that rivals X-ray crystallography. Magnetic resonance imaging (MRI) has become a routine procedure in diagnostic radiology. It is applied as a way to study metabolic function in humans and animals, and an evolving method in materials science.[3]

Recently, NMR has been detected with optical magnetometers rather than with the conventional inductive pickup coils. Atomic magnetometers use the quantum states of electrons as probes. Valence electrons in alkali-metal vapors or defects in crystalline solids can detect the magnetic fields producing nuclear spins.[4–8] The alkali-metal atomic magnetometer uses one laser beam to polarize the alkali-metal spins in an atomic vapor cell and the second probe beam to detect the change in the spin state due to the interaction with magnetic field. The atomic cell is placed near the target NMR sample to detect nuclear spin precession. Nitrogen vacancy centers are probed with laser irradiation and the resulting fluorescence intensity correlates to the magnetic field around it.[9–11] Optical detection of NMR offers the possibility of a higher detection sensitivity, which in some

cases is increased by more than 10 orders of magnitude compared to the traditional NMR,[12] a higher time resolution, on the order of 10^{-14} s, or selection of a particular chemical environment.[13]

One interaction between light and NMR has attracted much interest since the 1990s.[14–17] It was predicted that circularly polarized light could raise NMR frequencies from the megahertz to gigahertz range,[16] which would be useful in that it can increase the chemical shift resolution. Later, however, both theories and experiments proved that the actual frequency shift is on the order of 10^{-5} Hz.[14,17] Although the NMR frequency shift created by the local magnetic field shift is too small to be observed, the complementary magneto-optic effect, the rotation of linearly polarized light by magnetization of nuclei, is measurable. This effect is described as Nuclear Spin Optical Rotation (NSOR).[18]

The NSOR effect can therefore serve as an alternative basis for optical detection of NMR. The motivation for measuring NSOR is not an increase in sensitivity as in other optical detection methods; the signal-to-noise ratio of many reported NSOR measurements is lower than that of a corresponding NMR measurement. Rather, the NSOR effect presents an opportunity to obtain additional spectroscopic information. Because NSOR is measured by exciting the electrons, the signal does not only contain information on nuclear spins as obtained in NMR, but it also includes information on the hyperfine interaction and localized electron configuration. In addition, the NSOR effect holds the promise for fast imaging. In conventional MRI, many scans are required to form an 3D image during which three sets of gradient coils are changed encoding spatial resolution by means of manipulating the frequencies and phases of MR signal. The NSOR effect on the other hand, requires only one gradient and one scan to produce a full 3D image in the area illuminated by the laser. It can also produce a 2D projection image without any gradient field, which is especially useful in studying long-range dipolar interactions.[19,20]

The phenomenon of NSOR is similar to the Faraday rotation, which is the rotation of light polarization by the external magnetic field component along the light propagation direction. Due to Zeeman splitting, such a component induces a difference in the refractive indices of the left and right circular polarizations. This difference results in the rotation of the plane of linear polarization, which is the sum of the two circular polarization components. NSOR is based on the same mechanism involving the interaction of light with electrons, but instead of the external field, the rotation of the polarization plane is caused by local magnetic fields generated by nuclear spin magnetic moments, or in the language of quantum mechanics, by the hyperfine interaction.

The NSOR effect depends strongly on the local electron structure. For example, the NSOR effect from water protons is comparable in magnitude to the Faraday rotation that would be induced by the spatially averaged magnetic field of the ^{1}H, while in liquid ^{129}Xe, the NSOR effect is 135 times larger compared to Faraday rotation.[18] This difference is due to stronger attraction by the Xe nucleus of the electrons that dominantly contribute to the Faraday rotation.

NSOR can be measured in a wide range of substances, as long as they are sufficiently transparent for the chosen wavelength of light. Since the NSOR effect detects the interaction of electrons and nuclear spins and is encoded in the frequency domain as NMR, it has the potential to measure the electronic states at specific chemical sites.

1.1 Theory

1.1.1 Light Propagation in Optically Isotropic and in Circularly Birefringent Media

The mathematical representation of a light beam in a homogeneous medium containing no free charge and having no conductivity can be obtained by solving the reduced Maxwell equations:

$$\nabla \cdot \boldsymbol{D} = 0 \tag{1.1a}$$

$$\nabla \cdot \boldsymbol{B} = 0 \tag{1.1b}$$

$$\nabla \times \boldsymbol{E} = -\frac{\partial \boldsymbol{B}}{\partial t} \tag{1.1c}$$

$$\nabla \times \boldsymbol{H} = -\frac{\partial \boldsymbol{D}}{\partial t} \tag{1.1d}$$

where the $\boldsymbol{D}$ and $\boldsymbol{H}$ fields are related to the $\boldsymbol{E}$ and $\boldsymbol{B}$ fields by the following expression:

$$\boldsymbol{D} = \epsilon_0 \boldsymbol{E} + \boldsymbol{P} \tag{1.2a}$$

$$\boldsymbol{H} = \frac{1}{\mu_0} \boldsymbol{B} - \boldsymbol{M} \tag{1.2b}$$

ϵ_0 and μ_0 are the permittivity and permeability of free space; $\boldsymbol{P}$ is the electric polarization in the medium; $\boldsymbol{M}$ is the magnetization of the medium.

For the purpose of this dissertation, only two special solutions of Equation 1.1 will be discussed: a linearly polarized beam (LPB) and a circularly polarized beam (CPB). In an LPB, the oscillating electric field is contained in a single plane. Typical sources of such beams are lasers, which are commonly used in optical spectroscopy.

The electric and magnetic fields of an LPB can be represented as the real part of the expression

$$\boldsymbol{E}_{\text{linear}} = \boldsymbol{E}^{(0)} \cdot e^{i(\boldsymbol{kr}-\omega t)} \tag{1.3a}$$

$$\boldsymbol{B}_{\text{linear}} = \boldsymbol{B}^{(0)} \cdot e^{i(\boldsymbol{kr}-\omega t)} \tag{1.3b}$$

where the components of $\boldsymbol{E}^{(0)}$ represent the amplitudes of the electric field in different directions; $\boldsymbol{k} = \omega \cdot \boldsymbol{n}/c$ is the propagation vector with magnitude corresponding to the refractive index n, ω is the angular frequency of the light, $\boldsymbol{r}$ is the position in space and t is time. Plane waves have $\boldsymbol{E}^{(0)}$, $\boldsymbol{B}^{(0)}$ and $\boldsymbol{k}$ mutually perpendicular.

A CPB is a superposition of two LPB with respective $\boldsymbol{E}^{(0)}$ in the perpendicular directions of unit vectors $\boldsymbol{i}$ and $\boldsymbol{j}$ (both orthogonal to $\boldsymbol{k}$) and phase difference of $\pm\pi/2$, as shown in Equation 1.4, written for an optically isotropic medium.

$$\boldsymbol{E}_{\text{L}} = \frac{E^{(0)}}{\sqrt{2}}(\boldsymbol{i} + i\boldsymbol{j})e^{i(\boldsymbol{kr}-\omega t)} \tag{1.4a}$$

$$\boldsymbol{E}_{\text{R}} = \frac{E^{(0)}}{\sqrt{2}}(\boldsymbol{i} - i\boldsymbol{j})e^{i(\boldsymbol{kr}-\omega t)} \tag{1.4b}$$

When viewed along the propagation direction, the electric field of a CPB traces a circle, and depending on the rotation direction, the beam can be either a left circularly polarized beam (lCPB) or right circularly polarized beam (rCPB). An LPB can in turn be viewed as a superposition of a lCPB and a rCPB (Figure 1.1. The representation of LPB as the sum of two CPB is illustrated in Figure 1.2a by viewing the electric field vectors in the plane perpendicular to the light propagation direction. From Equation 1.4, at a specific time, *e.g.* $t = 0$, $\boldsymbol{E}_{\text{linear}} = 1/\sqrt{2} \cdot (\boldsymbol{E}_{\text{L}} + \boldsymbol{E}_{\text{R}}) = E^{(0)}e^{i\boldsymbol{kr}}$, which means that $\boldsymbol{E}_0$ of the light will remain in the same linearly polarized direction over the entire space.

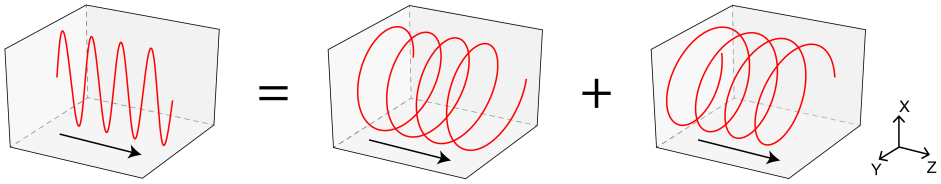

Figure 1.1: The illustration of decomposition of LPB on lCPB and rCPB; the red curves are the traces of electric field of the light; the arrows show the propagation direction.*

In a circularly birefringent medium, the refractive indices of lCPB and rCPB are different, requiring the replacement of the wave vector $\boldsymbol{k}$ in Equation 1.4 with vectors of different magnitude, $\boldsymbol{k}_{\mathrm{L}}$ and $\boldsymbol{k}_{\mathrm{R}}$ for $\boldsymbol{E}_{\mathrm{L}}$ and $\boldsymbol{E}_{\mathrm{R}}$, respectively. For linearly polarized light written as the superposition of the two circular polarizations, $\boldsymbol{E}_{\text{linear}} = \boldsymbol{E}^{(\mathbf{0})}[\boldsymbol{i}\cos((\boldsymbol{k}_{\mathrm{L}} + \boldsymbol{k}_{\mathrm{R}})\boldsymbol{r}/2) + \boldsymbol{j}\sin((\boldsymbol{k}_{\mathrm{L}} + \boldsymbol{k}_{\mathrm{R}})\boldsymbol{r}/2)] \cdot \exp[i(\boldsymbol{k}_{\mathrm{L}} - \boldsymbol{k}_{\mathrm{R}})\boldsymbol{r}/2]$. This sum results in a rotation of the optical polarization plane with an angle $\Delta\theta = (\boldsymbol{k}_{\mathrm{L}} - \boldsymbol{k}_{\mathrm{R}})\boldsymbol{r}/2 = (\omega l/2c)(n_{\mathrm{L}} - n_{\mathrm{R}})$, which depends on the spatial position l along the propagation direction through the medium (Figure 1.2b).

1.1.2 Faraday Rotation

Faraday Rotation (FR) was discovered by Michael Faraday in 1845 as the first experimental evidence that light and magnetic fields are related. This effect is due to circular birefrigence in a dielectric medium in the presence of an external magnetic field. This section outlines how FR arises from molecular properties and is intended to form a basis to understand the NSOR effect.

When an external magnetic field is applied to the medium, the molecular or atomic quantum states are slightly perturbed by the Zeeman effect, and the sublevels cause a

*Reprinted with permission from "Nuclear Spin Optical Rotation" by Zhu, Y.; Hilty, C.; Savukov, I. M., **2019**. *eMagRes*, *8*, 205-214, Copyright 2019 by John Wiley & Sons, Ltd.[2]

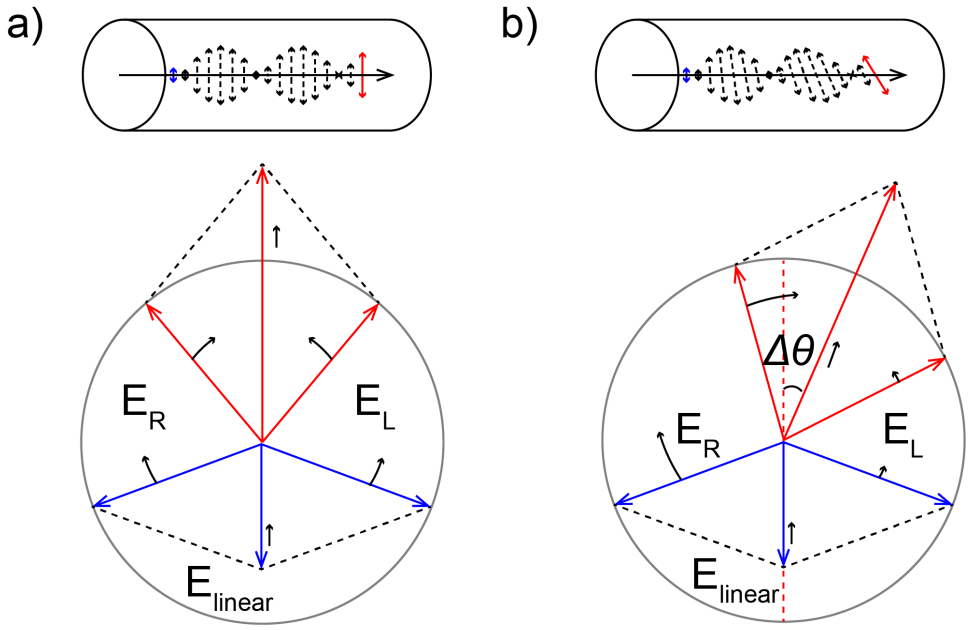

Figure 1.2: The electric field of a LPB and its circularly polarized components in the plane perpendicular to the propagation direction, for a) an optically isotropic medium and b) a circularly birefringent medium. The arrows indicate the change rate of the phases of the field when traveling along the sample.*

different effect for lCPB and rCPB. For example, for a system with electron orbital angular momentum $L = 0$, electron spin angular momentum $S = 1/2$ and nuclear spin angular momentum $I = 1/2$, the total angular momentum is $J = 1$. Therefore, there are two hyperfine energy levels without the magnetic field, namely $F = 0$ and $F = 1$. In the presence of an external magnetic field, the degeneracy of $F = 1$ states is lifted, and the three sublevels ($m_F = -1, 0, 1$) are separated by $\Delta E = m_{\mathrm{F}} g \mu_{\mathrm{B}} B$, where g is the Landé g-factor depending on the states of L, S, I and μ_{B} is the Bohr magneton. Photons also have angular momentum with angular momentum quantum numbers of $+1$ and -1 for lCPB and rCPB respectively. When transitions from $F = 1$ to $F = 0$ are considered, in order to conserve the total angular momentum, they must be circular-polarization selective. Since the magnetic sublevels are different, the transitions from the $F = 1$ to $F = 0$ states have

*Reprinted with permission from "Nuclear Spin Optical Rotation" by Zhu, Y.; Hilty, C.; Savukov, I. M., **2019**. *eMagRes*, *8*, 205-214, Copyright 2019 by John Wiley & Sons, Ltd.[2]

different resonance frequencies for lCPB and rCPB. The refractive index is dependent on the resonance frequency, as seen in the calculation of polarizabilities below. Therefore, the light polarization angle changes according to the analysis in the previous section. In the following, a more systematic derivation of Faraday Rotation for all the molecular states is outlined, according to Refs[21–23].

The bulk polarization can be expressed in terms of the statistical average molecular electric dipole moment $\boldsymbol{\mu}$: $\boldsymbol{P} = N\boldsymbol{\mu}$, where N is the number density of the molecules. If the molecular polarization is purely induced by the light wave, the molecular dipole moment can be represented as: $\mu_{\mathrm{u}} = \sum_{\mathrm{v}} \alpha_{\mathrm{uv}} E_{\mathrm{v}}$, where u, v can take values of x, y, z and α_{uv} is the polarizability in the direction u, induced by an electric field in the direction v.

The modified electric field in a medium perturbed by a light wave then becomes:

$$D'_{\mathrm{u}} = \epsilon_0 E_{\mathrm{u}} + N \sum_{\mathrm{v}} \alpha_{\mathrm{uv}} E_{\mathrm{v}} \tag{1.5}$$

A fundamental equation including D' derived from Maxwell's equations is:[24]

$$n_{\mathrm{u}} n_{\mathrm{v}} E_{\mathrm{v}} - n^2 E_{\mathrm{u}} + \mu_0 c^2 + D'_{\mathrm{u}} = 0 \tag{1.6}$$

By inserting the electric field of CPB (Equation 1.4) and Equation1.5 into this expression and assuming the propagation direction of z, two sets of equations can be obtained:

$$\begin{aligned} (n^2_{\substack{\mathrm{L}\\\mathrm{R}}} - 1) - \mu_0 c^2 N(\alpha_{\mathrm{xx}} \pm i\alpha_{\mathrm{xy}}) = 0 \\ (n^2_{\substack{\mathrm{L}\\\mathrm{R}}} - 1) - \mu_0 c^2 N(\alpha_{\mathrm{yy}} \mp i\alpha_{\mathrm{yx}}) = 0 \end{aligned} \tag{1.7}$$

which can be combined into:

$$(n^2_{\substack{\mathrm{L}\\\mathrm{R}}} - 1) - \frac{1}{2}\mu_0 c^2 N[\alpha_{\mathrm{xx}} + \alpha_{\mathrm{yy}} \pm i(\alpha_{\mathrm{xy}} - \alpha_{\mathrm{yx}})] = 0 \tag{1.8}$$

and therefore:

$$n_{\substack{\mathrm{L}\\\mathrm{R}}} \approx 1 + \frac{1}{4}\mu_0 c^2 N[\alpha_{\mathrm{xx}} + \alpha_{\mathrm{yy}} \pm 2\alpha'_{\mathrm{xy}}] \tag{1.9a}$$

$$\Delta\theta \approx \frac{1}{2}\omega\mu_0 c l N \alpha'_{\mathrm{xy}} \tag{1.9b}$$

where $\alpha'_{\mathrm{xy}} = \Im[(\alpha_{\mathrm{xy}} - \alpha_{\mathrm{yx}})/2]$.

The remaining question becomes how to calculate the polarizability. This can be achieved by solving the time dependent Schrodinger equation of the molecule with a perturbation of an oscillating electric and magnetic field from the light wave. With the molecular quantum states, *i.e.* eigenstates $|q\rangle$ [25] obtained, α'_{xy} can be represented as:

$$\alpha'_{\mathrm{xy}} = \frac{2}{\hbar} \sum_{|p\rangle \neq |q\rangle} \frac{\omega}{\omega^2_{pq} - \omega^2} \Im(\mu^{qp}_{\mathrm{x}} \mu^{pq}_{\mathrm{y}}) \tag{1.10}$$

where ω_{pq} is the transition frequency between $|p\rangle$ and $|q\rangle$ and $\mu^{pq}_{\mathrm{x}} = \langle p|\mu_{\mathrm{x}}|q\rangle$ is the element of the electric dipole matrix.

In the absence of other perturbations and far from the resonance frequency, α'_{xy} becomes

$$\alpha'_{xy} \approx \frac{2}{\hbar\omega} \sum_{|p\rangle \neq |q\rangle} \Im(\mu_{\mathrm{x}}^{qp} \mu_{\mathrm{y}}^{pq}) \tag{1.11}$$

It is zero due to the fact that $\sum |p\rangle \langle p| = 1$ (therefore $\sum_{|p\rangle \neq |q\rangle} \mu_{\mathrm{x}}^{qp} \mu_{\mathrm{y}}^{pq} = (\mu_{\mathrm{x}} \mu_{\mathrm{y}})^{qq} - \mu_{\mathrm{x}}^{qq} \mu_{\mathrm{y}}^{qq}$) and that μ_{x}, μ_{y} are commuting Hermitian operators.

By introducing an external magnetic field, the modified eigenstates and energies can be obtained with the time independent perturbation method:

$$|p'\rangle = |p\rangle - \frac{B_0}{\hbar} \sum_{|u \neq p\rangle} \frac{1}{\omega_{pu}} m_{\mathrm{x}}^{up} |u\rangle \tag{1.12}$$

$$\omega'_{pq} = \omega_{pq} - (m_{\mathrm{z}}^{pp} - m_{\mathrm{x}}^{qq}) B_{\mathrm{z}} \tag{1.13}$$

where the element of the magnetic dipole moment $m_{\mathrm{x}}^{pq} = \langle p | m_{\mathrm{x}} | q \rangle$.

Now the expression for the polarizability with perturbation from both the radiation field and external magnetic field can be obtained (in the following expression, eigenstates are the modified ones, $|p'\rangle$):[21,23,24]

$$\alpha'_{\mathrm{xy}}(\boldsymbol{B}) = \alpha'_{\mathrm{xy}} + \alpha'^{(\mathrm{D})}_{\mathrm{xy,z}} B_{\mathrm{z}} \tag{1.14}$$

$$\begin{aligned} \alpha'^{(\mathrm{D})}_{\mathrm{xy,z}} = & -\frac{2\omega}{\hbar^2} \sum_{|p\rangle \neq |q\rangle} \\ & \{ \frac{2\omega_{pq}}{(\omega_{pq}^2 - \omega^2)^2} (m_{\mathrm{z}}^{pp} - m_{\mathrm{z}}^{qq}) \mathrm{Im}(\mu_{\mathrm{x}}^{qp} \mu_{\mathrm{y}}^{pq}) + \frac{1}{\omega_{pq}^2 - \omega^2} \\ & [\sum_{|u\rangle \neq |q\rangle} \frac{1}{\omega_{uq}} \mathrm{Im}(m_{\mathrm{z}}^{uq} (\mu_{\mathrm{x}}^{qp} \mu_{\mathrm{y}}^{pu} - \mu_{\mathrm{y}}^{qp} \mu_{\mathrm{x}}^{pu})) \\ & + \sum_{|u\rangle \neq |p\rangle} \frac{1}{\omega_{up}} \mathrm{Im}(m_{\mathrm{z}}^{pu} (\mu_{\mathrm{x}}^{qp} \mu_{\mathrm{y}}^{uq} - \mu_{\mathrm{y}}^{qp} \mu_{\mathrm{x}}^{uq}))] \} \end{aligned} \tag{1.15}$$

Then Equation 1.9b can be written as:

$$\Delta\theta^{(\mathrm{D})} = \frac{1}{2}\omega\mu_0 clN\alpha'^{(D)}_{\mathrm{xy,z}}\boldsymbol{B}_0 \tag{1.16}$$

This equation represents the general form of Faraday rotation obtained in a nonmagnetized medium.

1.1.3 Nuclear Spin Optical Rotation

The NSOR effect can be considered as two different effects combined. One is the Faraday Rotation induced by the distant magnetic field created by nuclear spins ($\boldsymbol{B}_{\mathrm{d}}$), while the other is from the hyperfine interaction between a nuclear spin that provides a local field (B_{N}) and the electrons in the same molecule.

From Equation 1.16, the angle of polarization rotation created by the distant field is:

$$\Delta\theta_{\mathrm{d}} = \frac{1}{2}\omega\mu_0 clN\alpha'^{(\mathrm{D})}_{\mathrm{xy,z}}\boldsymbol{B}_{\mathrm{d}} \tag{1.17}$$

The hyperfine interaction part can be written as[21]:

$$\Delta\theta_{\mathrm{N}} = \frac{1}{2}\omega\mu_0 clN\alpha'^{(\mathrm{N})}_{\mathrm{xy,z}}B_{\mathrm{N}} \tag{1.18}$$

The polarizability $\alpha'^{(\mathrm{N})}_{\mathrm{xy,z}}$ can be obtained from Equation 1.14 by replacing the m_{z}^{pq} term with the hyperfine constant term a_{z}^{pq}:

$$a_{\mathrm{z}}^{pq} = \gamma\frac{\mu_0}{4\pi}g^*\mu_{\mathrm{B}}\hbar\sum_i\left\langle p\middle|\frac{L_{\mathrm{z}}}{r_j^3} - \frac{S_{\mathrm{z}}}{r_j^3} + \frac{3z(\boldsymbol{S}\cdot\boldsymbol{r_j})}{r_j^5} + \frac{8}{3}\pi\delta(r_j)S_{\mathrm{z}}\middle|q\right\rangle \tag{1.19}$$

where the sum is taken over all nuclei (with gyromagnetic ratio of γ_j) in the molecule;

μ_{b} is the Bohr magneton; g^* is the effective g-factor in the system; $\boldsymbol{L}$ is the electron orbital angular momentum; $\boldsymbol{S}$ is the electron spin angular momentum; $\boldsymbol{I}$ is the nucleus angular momentum. The enhancement from this hyperfine interaction compared to the FR from local nuclear field (B_{N}) can be represented as $\kappa = \alpha'^{(\mathrm{N})}_{\mathrm{xy,z}}/\alpha'^{(\mathrm{D})}_{\mathrm{xy,z}}$.

The $\alpha'^{(\mathrm{N})}_{\mathrm{xy,z}}$ (Equation 1.15) can be simplified to show that the NSOR signal depends on $\omega^2 \propto 1/\lambda^2$ when $\omega \ll \omega_{pq}$, which is often the case for ω in the visible range of the spectrum.

1.1.4 Unit Convention

FR signal is proportional to the length of sample the light traveled through l, and the external magnetic field strength B, the Verdet constant (V) in the unit of (rad T^{-1} m^{-1}) is defined as:

$$V = \frac{\Delta\theta}{Bl} \tag{1.20}$$

Similarly, the NSOR signal is proportional to the length of sample the light traveled through l, the polarization level of the sample (P proportional to the sample magnetization) and the concentration of the sample (N_{n}), in the literature the NSOR constant φ_{n} is defined as:

$$\varphi_{\mathrm{n}} = \frac{\Delta\theta}{N_{\mathrm{n}} P l} \tag{1.21}$$

where $\Delta\theta$ is the experimentally observed rotation angle of the sample. Due to the small number of the NSOR constant, the unit is often set to be $\mu\mathrm{rad}$ M^{-1} cm^{-1}.

1.2 General Experimental Setup

1.2.1 Optical Setup

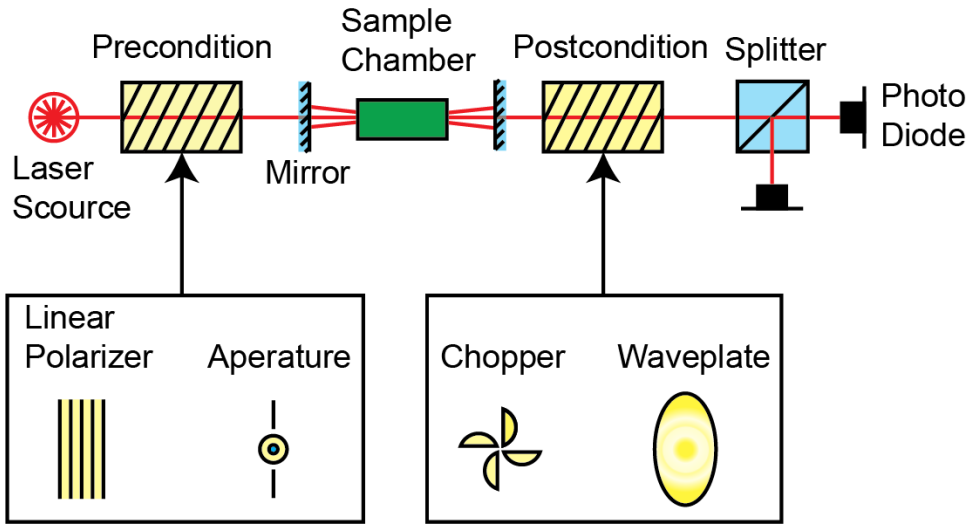

Figure 1.3: The general optical setup of the NSOR detection. The precondition and postcondition can include but are not limited to the elements shown in this figure.*

Since the principles of the detection of NSOR are similar to those of the Faraday Rotation, similar optical instruments as depicted in Figure 1.3 can be used to measure both effects. The laser beam is sent through the sample cell and divided into two beams of equivalent intensity with a beam splitter. The sum and difference of the intensities are taken for rotation angle calculation. For bulk measurements, the laser beam is usually conditioned before and after passing through the sample. For pre-conditioning, a linear polarizer may be used to improve the laser polarization purity. An aperture can improve the beam shape so that the laser beam can pass through small sample cells multiple times; a chopper has been utilized to modulate the light, differentiating the signal from electrical

*Reprinted with permission from "Nuclear Spin Optical Rotation" by Zhu, Y.; Hilty, C.; Savukov, I. M., **2019**. *eMagRes*, *8*, 205-214, Copyright 2019 by John Wiley & Sons, Ltd.[2]

coupling to the NMR subsystem. A half waveplate can serve as a way to rotate the polarization plane. One setup implemented with a high field NMR spectrometer used optical fibers to guide the laser light inside the bore of the magnet, where the sample was located and lenses were added for collimating the light beam.[26,27] In all implemented setups, the laser beam is split into two by a polarizing beam splitter. The two beams are balanced by rotating the incident beam's polarization plane to 45 degrees with respect to the splitting plane, which is important for suppressing intensity fluctuation noise. The two intensities can be represented in terms of the initial light intensity and the relative angle to the beam splitter, so:

$$\begin{aligned} I_1 &= I_0 \cos^2(\pi/4) = 1/2 I_0 \\ I_2 &= I_0 \sin^2(\pi/4) = 1/2 I_0 \end{aligned} \tag{1.22}$$

When there is FR or NSOR, the polarization angle of the laser beam relative to the beam splitter changes by a value θ, resulting a difference between the two laser beam intensities:[28]

$$\begin{aligned} I_1 &= I_0 \cos^2(\pi/4 - \theta) \\ I_2 &= I_0 \sin^2(\pi/4 - \theta) \\ \theta &\approx \frac{I_1 - I_2}{2(I_1 + I_2)} \end{aligned} \tag{1.23}$$

Thus, the polarization rotation angle can be extracted as the ratio of the difference and sum of the two photo diode signals. The rotation angle has a component that follows the nuclear spin magnetization, and it can be observed in the frequency domain, as is common

practice for the detection of NMR signals. Some modulations of the light or the magnetic field (B_0) further complicates the analysis,[1,18,26] but the general idea remains the same.

One common theme in many NSOR detection setups is to pass the beam multiple times through the sample.[1,29] Since the light polarization rotation angle does not change when the beam is reflected by a mirror, and the relative magnetic field direction changes relative to the direction of the light, the contribution to the rotation angle from each pass through the sample adds up. Optical cavity and multi-pass cell are two possible options for the NSOR experiment. While optical cavities have been used to amplify optical dispersion effects,[30,31] the simplicity and robustness of a multi-pass cell[32,33] has made it a common choice for NSOR experiments. There still is a limit on how many passes can enhance the optical signal. On the one hand, the optical rotation increases linearly with the light path length and is proportional to the number of passes. On the other hand, the light intensity can be lost every time the beam passes through the sample cell by reflections at the optical windows and absorption from the sample. Since the rotation angle signal-to-noise ratio (SNR) scales proportionally with the square root of the light intensity, with a number of passes n, SNR $\propto n \cdot 10^{-A_0 n/2}$. This expression indicates that a maximum of SNR depends on the single pass losses A_0, which includes absorption. For example, if $A_0 = 0.05$, the optimal number of passes is 17. However, in the regime where laser technical noise after substantial attenuation and ultimately the electronics noise dominate, the scaling can be quite different, but still the number of useful passes will be limited.[29]

Another parameter that could be adjusted to increase SNR is the wavelength of the laser. As can be seen in Equation 1.15, the NSOR constant becomes larger as the light frequency approaches the electronic absorption frequency and increases as the square of the frequency difference. However, as in the case of the multi-pass enhancement, the absorption can impose a limit: The closer the light approaches the electronic absorption

frequency, the higher will the absorption be, and the SNR should be optimized by taking this trade off into consideration. For most transparent liquids such as water and ethanol, the electronic absorption wavelengths in the UV region range from 150 nm to 350 nm, which are far from the wavelength (405 nm) of inexpensive diode lasers. When using these lasers, it is usually beneficial to implement multiple passes in the NSOR experiment.[1,29]

1.2.2 NMR Setup

Nuclear spin coherences naturally encode the NSOR signal in the frequency domain by modulating the nuclear magnetization. At the same time, NMR signal can be obtained to calibrate the NSOR signal. The nuclear spins are prepared by a polarization process, which increases the population difference of the nuclei. The nuclear spin polarization is defined as the fractional difference of the population of the two nuclear spin energy levels (α and β), $P = (n_\alpha - n_\beta)/(n_\alpha + n_\beta)$.

Since the NSOR signal is very small, it becomes beneficial to maintain the transverse magnetization of the sample by using a spin-lock pulse sequence. A spin-lock can be achieved by adiabatically inverting the spins with an oscillating magnetic field perpendicular to the main magnetic field.[34] This prolongs the averaging time and generally increases the SNR. However, it prevents free spin precession, and the chemical distinction is lost. In contrast, a Carr-Purcell-Meiboom-Gill (CPMG) pulse limits the signal average time within the spin-spin relaxation, but allows frequency resolution due to free precession of nuclei.[27,29]

One issue with inductive detection in NSOR experiments is the current produced in the pick up coil from EMF created by the NMR signal. Because the coil is oriented parallel to the propagation of the polarized light, this current results in a magnetic field, which induces the Faraday rotation of the light beam and mimics the NSOR signal. Because

both signals have the same frequency, they need to be differentiated. This issue becomes important when a tuned circuit is used, which increases EMF by the quality factor Q of the circuit. The most straightforward method to avoid this problem, which still provides sufficient SNR, is to detect NMR signals needed for calibration of the NSOR signal with an un-tuned coil. The un-tuned detection gives small NMR-induced Faraday rotation, usually less than 5% depending on the specific setup, stray capacitance of the coil, and the amplifier input impedance, and it can be neglected.[29]

1.3 Non-hyperpolarized NSOR approaches

Without a hyperpolarization technique, the preparation of a sample with sufficient magnetization for NSOR measurement is similar in both high field and low field experiments. Samples need to remain in a high magnetic field before being measured, which usually contain a superconducting magnet maintained with liquid helium.

In the high field experiment, samples are easily polarized inside the NMR spectrometer.[26] For measurement at a low field, the sample is often sent through a high magnetic field (> 1 T) for prepolarization, and then adiabatically transferred to the low field instrument.[1,29] The prepolarization step needs to consider both the field strength and transfer issues, such as transfer time and specific arrangement. Considerations include the tubing and the pump used. For example, using a superconducting magnet of a high field NMR spectrometer can result in a high initial polarization level, but the travel distance to the low field instrument will be long, resulting in a large relaxation loss. On the other hand, using a permanent magnet can produce a smaller initial polarization, but the polarized sample will travel a shorter distance to the detection region, resulting in a final polarization level still sufficient for NSOR detection in many liquids. The relaxation rate of the sample affects the effectiveness of the approach involving transferring of the sample. The faster

the relaxation becomes, the shorter the maximum permitted transfer time is.

1.3.1 Low field NSOR

Savukov *et al.* first demonstrated measurement of the NSOR signal of protons in water with the spin-lock method (shown in Figure 1.4). The B_0 field was modulated on and off at the frequency of about 8 Hz. In Figure 1.4b, the signals obtained at wavelengths used (532 nm and 1064 nm) for proton are compared with the theoretical FR signal. It can be seen that NSOR signals fits well with the FR curve. NSOR signal can be viewed as an addition of two parts, the FR due to bulk magnetization and hyperfine interaction in close range of the nucleus. A similar magnitude of NSOR and FR indicates that the proton NSOR signal in water has very little hyperfine interaction part.

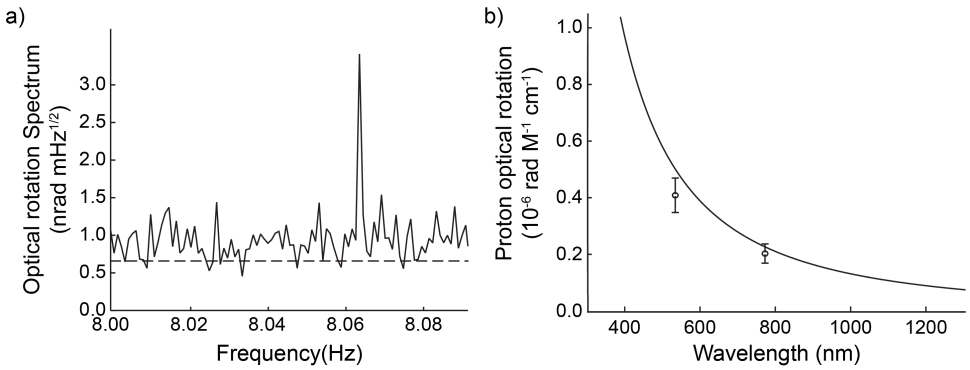

Figure 1.4: (a) Proton optical rotation obtained at a wavelength of 770 nm. The dashed line shows the shot noise level for 2.9 mW detected laser power. (b) Optical rotation angle per unit length for 1 M concentration of fully polarized liquid proton. The solid line is FR calculated for the distant magnetic field from the sample.*

Shi *et al.* have developed a multi-pass cell for NSOR detection using curved mirrors, creating 14 passes and a total laser path length of 3.15 m.[1] Combined with a shorter

*Reprinted with permission from "Optical Detection of Liquid-state NMR" by Savukov, I. M.; Lee, S.-K.; Romalis, M. V., **2006**. *Nature*, *442*, 1021-1024, Copyright 2006 by Springer Nature.

laser wavelength (405 nm), a SNR greater than 15 was achieved for many fluids using an averaging time of 1000 s. The NSOR and Verdet constants of compounds studied are shown in Table 1.1. It can be seen that the NSOR constant of fluorine in a liquid, perfluorohexane, is by far the largest. Protons were observed to have the largest NSOR constant in the aliphatic groups, while the $-$OH group appears to reduce the effect. It is expected that the electron density near the nucleus will affect the NSOR constant. In $-CH_2$ groups, the electrons are evenly distributed between carbon and proton due to a similar electronegativity, while the oxygen has a significantly higher electronegativity and attracts the electron from proton in an $-$OH group. Fluorine has a much larger NSOR constant than proton because it attracts electron density from the adjacent carbon atom due to its very high electronegativity.

Table 1.1: Measured NSOR constant and scaled Verdet constant of ^{1}H and ^{19}F. Verdet constants are scaled by classical magnetic field generated by 1 M of polarized nuclei in a long cylinder.*

Compound	NSOR Constant (μrad M^{-1} cm^{-1})	Verdet Constant (μrad M^{-1} cm^{-1})
Water	0.94 ± 0.05	0.88
Methanol	1.52 ± 0.08	0.62
Ethanol	1.96 ± 0.10	0.75
Propanol	1.97 ± 0.10	0.79
Isopropanol	1.93 ± 0.10	0.82
Hexene	1.96 ± 0.10	0.98
Hexane	2.25 ± 0.12	0.80
Cyclohexane	2.29 ± 0.11	0.82
Perfluorohexane	13.23 ± 0.67	0.23

In this project, the NSOR signal is also first measured with a similar setup but with a different pulse sequence. The change of pulse sequence made it possible to resolve two

*Reprinted with permission from "Observation of Optical Chemical Shift by Precision Nuclear Spin Optical Rotation Measurements and Calculations" by Shi, J.; Ikalainen, S.; Vaara, J.; Romalis, M. V., **2013**. *The Journal of Physical Chemistry Letters*, *4*, 437-441, Copyright 2013 by American Chemical Society.

different nuclei at the same time in frequency domain.

1.3.2 High field NSOR

At high field, chemical shift of the nuclei becomes available. Pagliero *et al.* have made a custom probe for a 400 MHz NMR system.[26,27] A cell with optical windows on both sides, optical fibers and mirrors allowed 532 nm laser light to pass through the cell. The laser beam was modulated with a chopper to avoid pick-up of electronic cross-talk. A CPMG sequence was utilized to measure chemical shift. For example, C_6F_6 and C_6F_{14} are shown to be at different chemical shift in both NMR and NSOR channel. As shown in Figure 1.5, relative signal strengths of H_2O, C_6H_5Br and $C_{10}H_7Br$ are different. While the NMR signals become smaller from left to right, the NSOR signals seem to be at similar level. The smaller NMR signal is due to the faster T_2 decay. The comparable NSOR signal arises from three possible factors. First, the electronic excitation wavelengths of the species on the right side are closer to the laser wavelength (see Equation 1.15). Second, molecules may contain larger hyperfine coupling constants. Since the spectral resolution is limited by the echo time, it is ambiguous which chemical group has a higher signal. Third, the electron density around the protons is higher in $C_{10}H_7Br$.

In Figure 1.6, the NSOR signal is shown for ^{13}C, ^{19}F and ^{31}P. Trends in the hyperfine coupling constant of these nuclei can be seen. The hyperfine coupling constant of ^{13}C appears to be significantly smaller than those of ^{19}F and ^{31}P.

1.4 Hyperpolarized NSOR Approaches

Hyperpolarization methods enhance NMR signals by preparing a non-equilibrium spin state prior to an NMR experiment.[35] The polarization of nuclei can be increased from typical values of $\sim 10^{-5}$ for conventional NMR using nuclear spins in a magnetic field to $\sim 10^{-1}$ or more when using hyperpolarization, translating into a signal gain of several

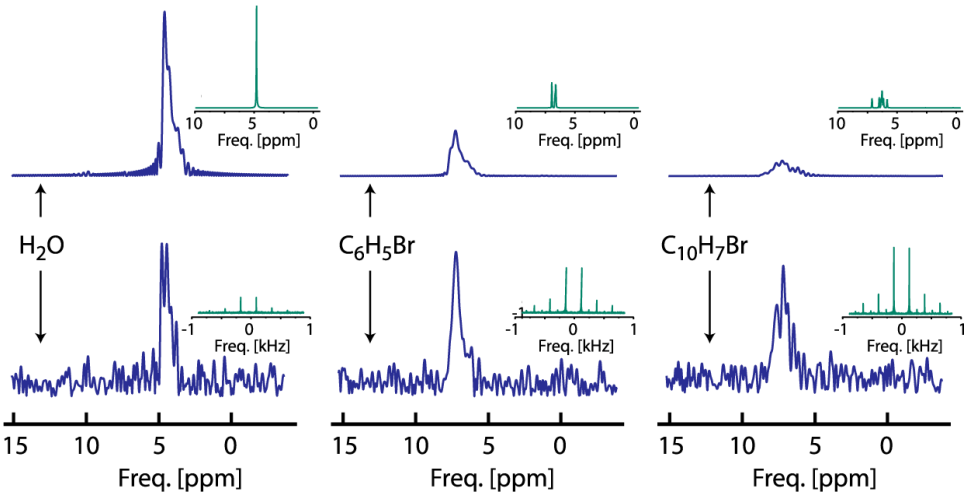

Figure 1.5: NMR and NSOR measurements at high field. Upper panels are the proton NMR spectra of the molecules noted on the side, while lower panels are NSOR spectra. The top insets are high resolution NMR spectra, and bottom insets are the modulated optical signals.*

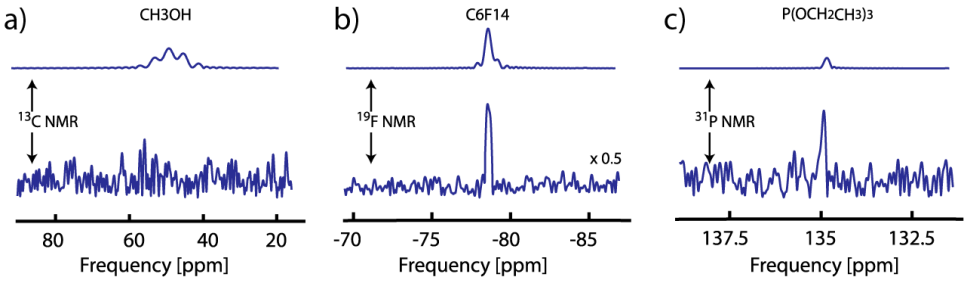

Figure 1.6: NSOR signals of several nuclei. Top and bottom show NMR signals and optical signals, respectively.*

orders of magnitude.[36–40]

Nuclear spin hyperpolarization can be produced by various techniques. One of the hyperpolarization technique polarizes noble gases such as xenon through optical pumping of an alkali vapor followed by spin exchange.[36] Using spin exchange optical pumping, it is possible to achieve near unity polarization in mixtures containing the noble gas in a buffer

*Reprinted with permission from "Magneto-optical contrast in liquid-state optically detected NMR spectroscopy" by Pagliero, D.; Meriles, C. A., **2011**. *Proceedings of the National Academy of Sciences*, *108*, 19510-19515, Copyright 2011 by National Academy of Sciences.

gas.[41]

Savukov *et al.* made use of hyperpolarized ^{129}Xe spins to demonstrate measurement of the NSOR effect at low field.[18] As shown in Figure 1.7a, the NSOR signal strength is proportional to the polarization of Xe, with a small offset within error range. The wavelength dependence is shown in Figure 1.7b. Since the wavelengths used (532 nm to 1064 nm) for Xenon are far longer than the electronic excitation wavelength, a $1/\lambda^2$ trend is observed in Xenon samples as seen in Equation 1.15.

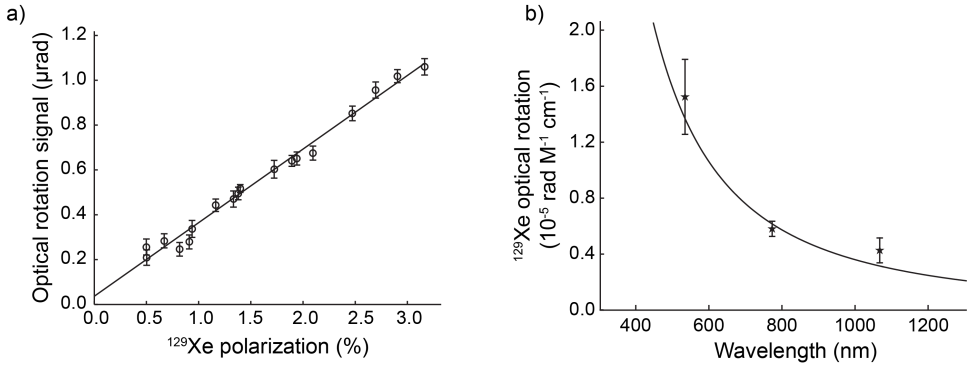

Figure 1.7: a) ^{129}Xe optical rotation as a function of polarization level at a wavelength of 770 nm. b) Optical rotation angle per unit length for 1 M concentration of fully polarized liquid ^{129}Xe. The solid line is a fit to the wavelength dependence of the NSOR effect for Xe with resonance wavelength $\lambda_k = 19.7$ nm.*

Another hyperpolarization technique is *para*-hydrogen induced polarization (PHIP),[39] where the ordered spin state of *para*-hydrogen is converted into spin alignment after hydrogenation of an unsaturated hydrocarbon. A variation of PHIP does not require a reaction forming covalent bonds. This technique, termed signal amplification by a reversible exchange (SABRE), relies on binding of *para*-hydrogen gas and the target molecule at a metal catalyst center, which facilitates transfer of spin order from

*Reprinted with permission from "Optical Detection of Liquid-state NMR" by Savukov, I. M.; Lee, S.-K.; Romalis, M. V., **2006**. *Nature*, *442*, 1021-1024, Copyright 2006 by Springer Nature.

para-hydrogen to the substrate.[42]

Petr *et al.* have taken advantage of a continuous flow SABRE hyperpolarization technique to measure the NSOR signal in pyridine and pyrazine. They also have used a low field setup for NSOR measurement. This method demonstrates that the NSOR signal can be obtained in dilute solutions instead of in neat compound (Figure 1.8).

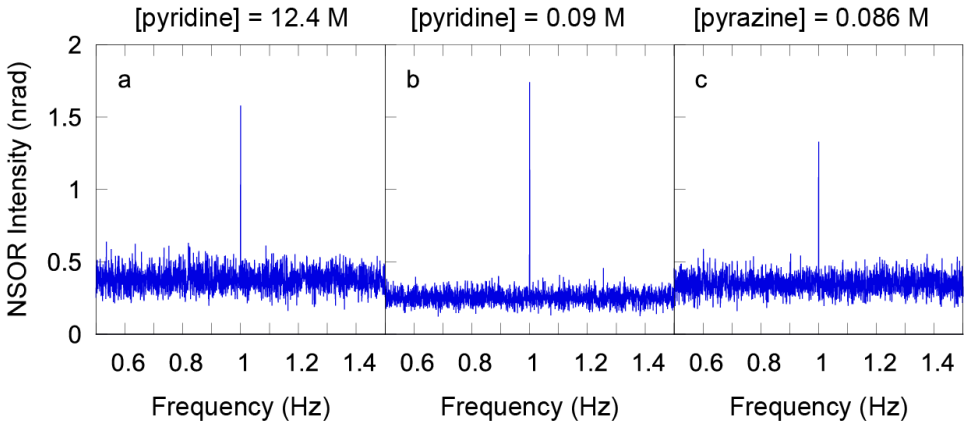

Figure 1.8: NSOR signal plots for a) Thermally polarized neat pyradine NSOR signal b) SABRE-polarized low concentration pyradine in methanol and c) SABRE-polarized low concentration of pyrazine in methanol.*

1.5 NSOR Computation and Theory

Substantial efforts have been devoted to the theory and calculation of the NSOR constants. Vaara group has used first-principle quadratic response theory calculations, which confirmed the $1/\lambda^2$ dependence for different nuclei in different molecules.[43] These calculations also showed that it is possible to discriminate different chemical groups in the same molecule using a wavelength corresponding to the specific transition frequency.

*Reprinted with permission from "Low-Concentration Measurements of Nuclear Spin-Induced Optical Rotation Using SABRE Hyperpolarization" by Štěpánek, P.; Kantola, A.M., **2019**. *The Journal of Physical Chemistry Letters*, *10*, 5458-5462, Copyright 2019 by American Chemistry Society.

Actual experiments with this goal would be challenging, because they would require a laser tunable to the transition frequency. At the transition frequency, absorption also increases, which leads to a decrease in the light intensity. Ikäläinen *et al.* calculated the NSOR constant for Xenon with both relativistic and non-relativistic corrections.[44] A comparison of the two sets of results showed that relativistic calculations differ by a factor of two from the non-relativistic ones, and are closer to the experimental results. Savukov has applied the atomic suite (relativistic configuration-interaction many-body-theory approach) to calculate NSOR in Xenon.[45] The atomic theory used includes a more advanced treatment of relativistic and other corrections compared to molecular calculations. The result showed good agreement with the experimental Verdet constant after replacing the calculated energy levels with the experimental ones. Pennanen *et al.* showed that in the liquid phase additional complexity in the calculation of the NSOR constant due to the extra factors of intramolecular motion, solvation effects on the single-molecule antisymmetric polarizability, local optical fields in the medium and bulk magnetization.[46]

While most of the theoretical work has been done using first principle calculations, an analytical method based on the experimental Verdet constant has also been described.[47] This simplified model based on the intermolecular and intramolecular hyperfine interaction gives a good agreement with the experimental result for the proton NSOR constant. Although the theory may not apply with the same accuracy to the other nuclei, it still provides insights into the basis of the NSOR effect.

Other physical effects that closely related to NSOR are the nuclear spin induced Cotton-Mouton effect (NSCM) and nuclear spin circular dichroism. NSCM is an effect that causes ellipticity in a linearly polarized beam perpendicular to the sample magnetic moment. It has the same explicit dependence on the bond lengths and angles, which means

a direct relationship between the NSCM and the molecular structure can be achieved. Lu *et al.* have derived an expression for the NSCM effect based on polarizability induced by nuclear moments disscussed in Ref[17,48] and theory of Cotton-Mouton effect.[49] The effect was estimated to be about two orders of magnitudes smaller than the corresponding NSOR effect. Yao *et al.* derived the NSCM expression for the total effect of a strong external magnetic field.[50] Fu *et al.* performed computations of NSCM for nobel gas atoms,[51] molecules[52,53] and molecules in a strong external magnetic field[54]. NSCD is in essence the same as NSOR, except that it is manifested by ellipticity instead of rotation of the light. Vaara *et al.* have formulated expressions describing NSCD based on a third order time dependent perturbation theory, and performed calculations for small organic molecules.[55] Štěpánek *et al.* calculated NSCD for cyrosines, thymines and nucleobases and demonstrated a relationship of NSCD with electronic excited states.[56]. However, no experimental results have been published for these two effects yet, despite that these signals are predicted to be comparable to or even larger than NSOR signals under certain conditions.[50,56]

1.6 Dynamic Nuclear Polarization

In this thesis, dissolution dynamic nuclear polarization (D-DNP) is employed as a way to increase polarization level of the nuclei.[57] As shown in figure 1.9, at low temperatures (about a few kelvins), the electron has almost unity polarization while nuclei has only a few percent. DNP increases the polarization of nuclei by transferring the polarization from electrons. There are four different mechanisms that DNP could occur, Overhauser effect, solid effect (SE), cross effect and thermal mixing (TM), depending on the experimental conditions. In D-DNP, SE and TM are the two possible transfer routes.[38]

The SE and TM typically happen in a glassy sample in the solid state, for example at

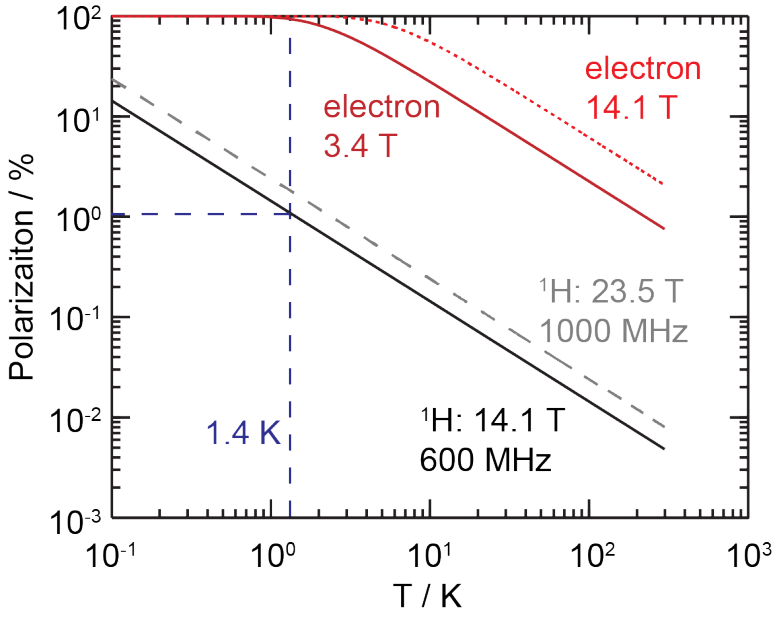

Figure 1.9: Polarization level of electron and nuclear spins as a function of temperature in different magnetic fields. In a 3.4 T magnetic field and at 1.4 K, the electron spins reach almost 100% polarization while the nuclear spins just hit the 1 % mark at 14.1 T. *

a temperature of 1.5 K. The SE occurs between an electron-nucleus pair. The energy level diagram for this process is shown in Figure 1.10. The forbidden W_0 or W_2 transition is driven by an external microwave source, at difference or sum of the Zeeman frequencies of the electron and nucleus $\omega_e \pm \omega_n$. If the microwave driven transition (W_0 or W_2) dominates the competing process of thermal relaxation (W_{1n}), the final polarization enhancement becomes γ_e/γ_n, where γ_e and γ_n are the gyromagnetic ratios of electron and nucleus.[58] Unlike in the SE, where the radical concentration is low, TM occurs when the electron concentration becomes high enough that the paramagnetic resonance (EPR) line is homogeneously broadened. TM involves many electrons in proximity and the electron spins can be considered as ensemble as opposed to electron-nuclear pairs. In practice, both effects can occur at once and it is difficult to distinguish SE from TM.[58]

*Reprinted with permission from "Dynamic Nuclear Hyperpolarization in Liquids" by Gunther, U. L., **2011**. *Topics in Current Chemistry*, *335*, 23-69, Copyright 2011 by Springer-Verlag Berlin Heidelberg.

After the sample is hyperpolarized, a dissolution process transfers the sample from the low temperature state to room temperature by dissolving it into a liquid by a hot stream of dissolution solvent. Although the dissolution process renders hyperpolarization non-repeatable, this technique is more versatile compared to hyperpolarized noble gas and PHIP since it can hyperpolarize almost any nuclei in any molecules.[59–62]

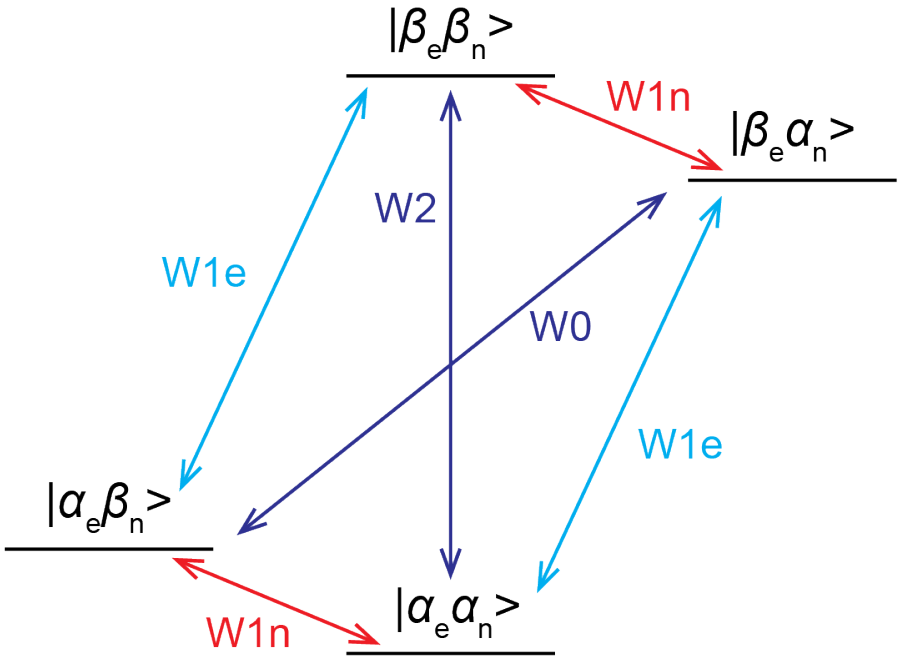

Figure 1.10: Energy level diagram for Solid Effect. The subscript 'e' represents the electron and 'n' a 1/2 spin nucleus. α and β represents the two energy levels caused by Zeeman effect. Ws are the transition probabilities.

2. MILLI-TESLA NMR AND SPECTROPHOTOMETRY OF LIQUIDS HYPERPOLARIZED BY DISSOLUTION DYNAMIC NUCLEAR POLARIZATION*

2.1 Introduction

Low field (LF) NMR holds the promise of solving a specific set of problems where the use of high fields is impossible or impractical, or where aspects of spin physics result in new information. Applied to in vivo magnetic resonance imaging (MRI), LF detection not only represents a low-cost modality, but also provides enhanced relaxation contrast.[64] At LF, the penetration depth of radio-frequency in metals is increased reducing imaging artifacts, further allowing MRI in the presence of metallic structures. In NMR spectroscopy, relaxation dispersion measurements can be used to obtain information on molecular dynamics on large time scales.[65–67] Spin relaxation measurements at low field have further been used in remote locations for the characterization of geological samples or even ice cores.[68,69] Although chemical shifts are collapsed at fields below 2 mT, it is still possible to observe and correlate nuclei of different type using *J*-couplings.[70] Line widths typically are narrower than at higher field, which enables resolving *J*-couplings when they are otherwise unobservable.[71,72] *J*-spectroscopy even at zero-field has been shown to contain chemical information alternative to the traditional spectra based on chemical shifts at high fields.[73,74] A major challenge in the application of LF NMR and MRI lies in the low obtainable signal strength compared to high-field NMR. The limitation in signal is first of all due to much smaller polarization, which is approximately proportional to the field strength B_0. In addition, the signal falls off as $B_0^{1/2}$, when it can be reasonably assumed that Q-factors of the high- and low-frequency detection coils

*Reprinted with permission from "Milli-tesla NMR and Spectrophotometry of Liquids Hyperpolarized by Dissolution Dynamic Nuclear Polarization" by Zhu, Y.; Chen, C.-H.; Wilson, Z.; Savukov, I. M.; Hilty, C., **2016**. *Journal of Magnetic Resonance*, *270*, 71-76, Copyright 2016 by Elsevier Inc.[63]

are comparable.[75] This latter sensitivity penalty at low field can be avoided by using ultra-sensitive non-inductive detectors, such as superconductive quantum interference devices and atomic magnetometers.[5,8,76,77] However, this is not sufficient for most applications, and LF NMR methods, especially at the extreme end of ultra-low field, rely on pre-polarization (switching on/off a stronger magnetic field and shuttling a sample through a region of higher field[78]) as well as hyperpolarization techniques. For example, optically hyperpolarized xenon was used for void space imaging, capitalizing on the ability of the low-frequency radiation to penetrate a metal enclosure,[79] and Overhauser effect dynamic nuclear polarization (O-DNP) in the liquid state was used to image plants[80] and other samples.[81–83] On the other hand, dissolution DNP (D-DNP), which over the past decade has become established as a versatile method for generating high polarization levels in liquid state NMR for many nuclei and chemical compounds, was not used in LF NMR. Thus in this paper, we propose and demonstrate the use of D-DNP as an alternative means for polarization enhancement in LF NMR. As immediate application, we apply D-DNP LF NMR to determine the polarization level and spin-lattice relaxation times of hyperpolarized samples containing free radicals under typical conditions encountered in D-DNP. In addition, we demonstrate nuclear Overhauser effect (NOE) measurements that can be used for the determination of intermolecular interactions.

2.2 Experimental Section

2.2.1 Experimental configuration

The experimental setup for LF NMR and optical measurements of D-DNP samples is schematically depicted in Figure 2.1. The LF NMR apparatus consists of an electro-magnet (a tetra-coil) to produce the main NMR field B_0 in the horizontal direction, a set of shim coils to cancel external gradients and to enable imaging, and two orthogonal

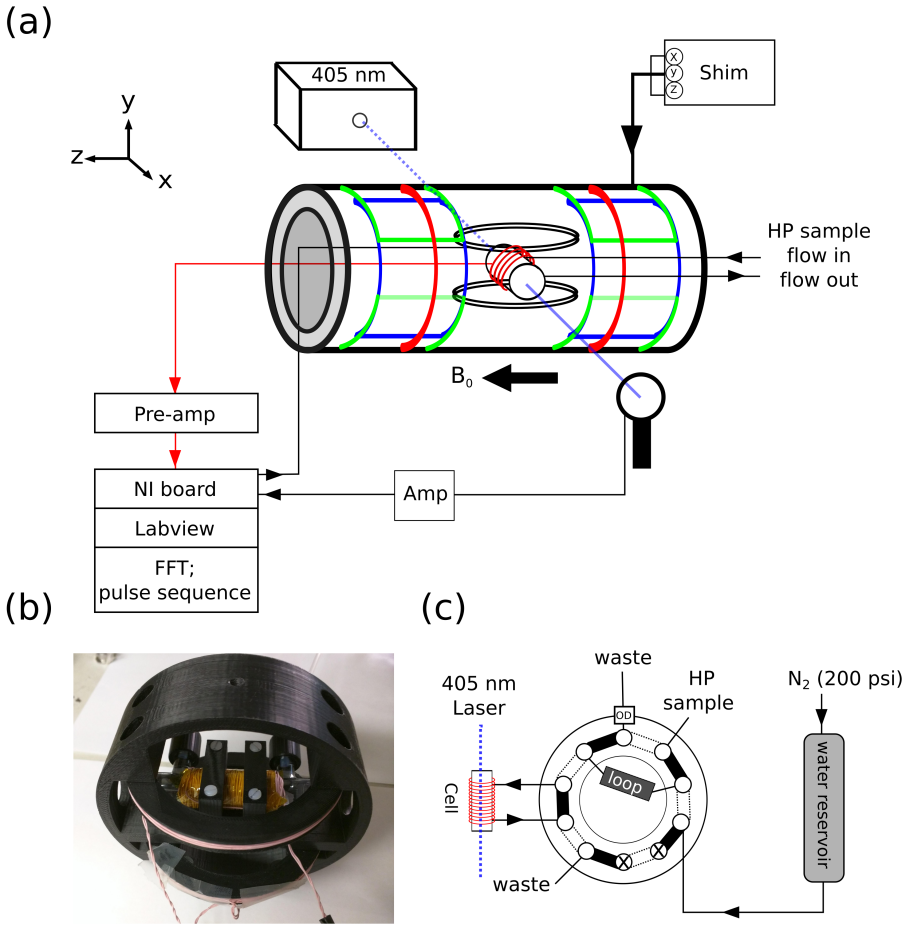

Figure 2.1: a) Configuration of the experiment. The flow cell, a small cylinder with the detection coil wound on its outer surface, is positioned in the center for simultaneous NMR and optical measurements. The excitation coil consists of two rings forming a Helmholtz arrangement with their axes perpendicular to that of the detection coil. Coils for shimming along three perpendicular axes x, y and z are wound on the large cylinder, and are drawn in blue, green and red, respectively. The laser beam intensity after the flow cell is measured with a photo-diode to monitor sample absorption. b) Geometry of core part of NMR spectrometer, including the flow cell with detection coil and excitation coil. c) Detail of the apparatus for sample transfer, consisting of an injection valve, a sample loop, and a reservoir containing pressurized water for driving the sample into the flow cell.*

rf coils to excite and detect nuclear spins (Figure 2.1a). The current for generating the B_0 field was provided by a digitally regulated linear power supply (XDL35-5TP, Xantrex,

*Reprinted with permission from "Milli-tesla NMR and Spectrophotometry of Liquids Hyperpolarized by Dissolution Dynamic Nuclear Polarization" by Zhu, Y.; Chen, C.-H.; Wilson, Z.; Savukov, I. M.; Hilty, C., **2016**. *Journal of Magnetic Resonance*, *270*, 71-76, Copyright 2016 by Elsevier Inc.[63]

Elkhart, IN). The shim coils, generating linear gradients in the *x*, *y* and *z*-directions, were positioned concentrically inside the tetra-coil. Shim currents were delivered using a dedicated shim power supply (Bruker Biospin, Billerica, MA). An aluminum shield between the shim coils and the rf coils was added to the setup to reduce electromagnetic interference from the environment. Separate sets of radio-frequency coils were used for NMR excitation and detection (Figure 2.1b) to reduce cross talk. The coils and flow cell were mounted on an insert printed from acrylonitrile butadiene styrene (ABS) plastic (Replicator 2X, MakerBot, Brooklyn, NY). The excitation coil was configured as Helmholtz pair ($r = 45$ mm, $n = 15 + 15$ turns) to produce a vertical field. This coil was driven directly by the output of a data acquisition board (PCIe-6259, National Instruments, Austin, TX). The detection coil wound around the flow cell (242 turns) was connected to a metallized polyester film capacitor to form a resonance circuit with a Q factor of 29. This resonant circuit was connected to the input of a pre-amplifier with adjustable gain and band-pass filter (SR-560, Stanford Research Systems, Sunnyvale, CA). After amplification, the signal was sent to the computer via data acquisition board for further signal processing. The flow cell was manufactured from Pyrex glass, fused with optical quality windows on both sides, for laser absorption measurements (Precision Glassblowing of Colorado, Centennial, CO).

For optical spectroscopy, a 3.5-mW laser with wavelength of 405-nm (Thorlabs, Newton, NJ) was mounted on a narrow optical bench attached below the electromagnet. Optical signal was detected using a photodiode (SMR1, Thorlabs) connected to a preamplifier built using a low-noise operational amplifier (OPA4131PJ, Texas Instruments, TX).

For hyperpolarization, the setup contained a HyperSense DNP polarizer (Oxford Instruments, Abingdon, UK). Dissolved samples were delivered through tubing (Teflon,

$1/8$" outer diameter, $1/16$" inner diameter) to a sample injection valve (Figure 2.1c), where they were loaded into a 3.0-mL loop. The configuration of the injection valve was similar to that described in ref[84]. Briefly, the completion of sample loading was sensed by an optical detector located at the outlet of the loop, which initiated switching of the injection valve (10W-0154L, VICI Valco, Houston, TX). A supply of water pressurized with nitrogen gas was then used for injecting the sample into the flow cell. The entire apparatus, including sample injection, pulse generation and data acquisition, was controlled using a LabView program (National Instruments, Austin, TX).[28]

2.2.2 Hyperpolarization

Samples for ^{1}H measurement were prepared by dissolving 15 – 60 mM 4-Hydroxy-TEMPO (TEMPOL) in a mixture of H_2O / ethylene glycol at 40/60 (v/v %) to produce a glass-forming matrix. The sample for ^{19}F measurement was prepared with 15 mM TEMPOL in trifluoroethanol. Samples were loaded into the variable temperature insert of the DNP polarizer, where they were held at a temperature of 1.4 K and irradiated with microwaves for 20 min at a frequency of 94.005 GHz and power of 100 mW. Subsequently, the samples were dissolved in a stream of 7.5 mL water, which had previously been heated in a closed vessel until a pressure of 10 bar was reached. The samples were taken into the loop of the injection device and driven into the flow cell using a pressure of 14 bar. For NMR measurements with stationary samples, the flow was stopped by simultaneous closure of inlet and outlet tubing. The injection valve was switched back to the original position following a pre-determined injection time of 700 ms. For experiments detecting flow, the valve was not switched back to the original position.

2.2.3 NMR Spectroscopy

The ^{1}H nuclei were detected in a static magnetic field of 0.7328 mT (1.899 A tetra-coil current) using thirty-five 31.2 kHz small flip angle $\pi/50.5$ pulses (each 0.16 ms) with the interval duration being 0.3 s. Signal acquisition was eight-fold oversampled. For determination of T_1, the spectrum obtained by performing Fourier transform on the time domain data was integrated to obtain the NMR amplitude for a given time. The spin-lattice relaxation time T_1 was found by fitting the amplitudes by the equation $a{\cdot}e^{-Rt}{+}c.$ with $R = R_1 + \ln(\cos\theta)/\tau$ to take into account the effects of multiple spin excitation; here, R_1 is the spin-lattice relaxation rate, θ is the flip angle and τ is the time interval between pulses.[85] In the present experiments, the contribution due to the RF pulses was negligibly small, $7 \cdot 10^{-3}$ s^{-1}, therefore R was equated to R_1 without losing accuracy. For quantification of the paramagnetic relaxation enhancement (PRE), the obtained relaxation rates R_1 were fitted to the equation

$$R_1 = R_1^0 + \epsilon c \tag{2.1}$$

where R_1^0 is the extrapolated relaxation rate in the absence of radical, ϵ is the paramagnetic relaxivity and c is the radical concentration.

In the imaging experiment, the x-gradient, together with the others tuned to compensate external gradients, was partially removed to introduce a frequency encoding gradient in the x direction, G_{x}. The gradient strength was estimated as $G_{\mathrm{x}} = 1.71 \cdot 10^{-4}$ mT/cm from the full width at half maximum of the signal spectrum and the detection coil length. Multiple delay times at $t = 5$, 10 and 15 s were applied before the acquisition for the observing time evolution of polarization distribution.

The experiment detecting ^{19}F was performed with a static magnetic field of 0.7559 mT (using a current of 1.937 A). After delay times of 2, 4, 6, or 8 s, a π/2 pulse was

applied, followed by ten second acquisition. The raw data were two-fold zero filled, Fourier transformed and phased. Data were processed using Matlab (Mathworks, Natick, MA).

2.2.4 Optical Measurements

The concentration of TEMPOL in a sample after its injection into the cell was determined from laser measurement of absorption $A = -\log_{10}(U_{\text{sample}} - U_{\text{dark}})/(U_{\text{blank}} - U_{\text{dark}})$, where U_{sample}, U_{blank} and U_{dark} are the output voltages observed in the output of the transimpedance amplifier proportional to the intensities of light in the presence of a DNP sample, without a DNP sample, and light blocked, respectively. The TEMPOL concentrations were calculated using $c = A/k$, where $k = 0.0669\,\text{M}^{-1}$ was determined using solutions of known concentration in a spectrophotometer (BioSpec-mini, Shimadzu, Columbia, MD). The dilution factor of the sample during dissolution d was then found from these concentrations as $d = c/c_{\text{DNP}}$, where c_{DNP} is the concentration of TEMPOL in the sample during DNP polarization known from sample preparation. The fraction of recovered sample was calculated as $r = V_{\text{cell}} \cdot d/V_{\text{DNP}}$, where V_{DNP} is the volume of the DNP polarized sample aliquot.

2.2.5 Determination of Polarization Level

Using theory developed in[28], we calculated bulk magnetization level from the measured voltage signal U_{observed} as

$$M_{\text{bulk}} = \frac{U_{\text{observed}}}{(2\pi^2 f) \cdot \mu_0 \cdot w \cdot a_{\text{c}}^2 \cdot Q \cdot g \cdot \sin(\theta)} \tag{2.2}$$

where f is the Larmor frequency, $\mu_0 = 4\pi \cdot 10^{-7}\,\text{H m}^{-1}$ is the vacuum permeability, $w = 242$ is the number of turns in the detection coil, $a_{\text{c}} = 4.41 \cdot 10^{-3}$ m is the radius of

the sample, $Q = 29$ is the quality factor of the resonator and $\theta = \pi/50.5$ is the flip angle of the excitation pulse. The preamplifier gain was $g = 500 \cdot 0.896$ (set to 500, reduced by 0.896 due to band-pass filtering). The polarization level of the sample in the measurement cell was then calculated using

$$P_{\text{bulk}} = \frac{M_{\text{bulk}}}{n \cdot \mu_{\text{I}}} \tag{2.3}$$

where $n = 5.814 \cdot 10^{28}\text{m}^{-3}$ is the number density of protons and $\mu_{\text{I}} = 1.4106 \cdot 10^{-26}$ J T^{-1} is the magnetic moment of the proton spin. Then the polarization level of spins before injection can be expressed as

$$P_{\text{DNP}} = P_{\text{bulk}}/d \tag{2.4}$$

The observed signal intensity is acquired from the complex Fourier transform of the time domain signal U_{time} as shown in the equation:

$$U_{\text{observed}} = \frac{1}{2\pi}\left[\left(\int A(\omega)d\omega\right)^2 + \left(\int D(\omega)d\omega\right)^2\right]^{\frac{1}{2}} \tag{2.5}$$

where $A(\omega) = \Re[\mathscr{F}(U_{\text{time}})]$ and $D(\omega) = \Im[\mathscr{F}(U_{\text{time}})]$. $\mathscr{F}$ denote Fourier Transform. This expression will remove the phase factor of the time domain signal. Assuming that the time domian signal has a phase factor of θ:

$$
\begin{aligned}
U'_{\text{time}} &= U_{\text{time}} \cdot e^{i\theta} \\
\mathscr{F}(U'_{\text{time}}) &= A'(\omega) + D'(\omega) \\
&= [A(\omega) + iD(\omega)] \cdot e^{i\theta} \\
&= [\cos\theta A(\omega) - \sin\theta D(\omega)] + \\
&\quad i[\sin\theta A(\omega) + \cos\theta D(\omega)]
\end{aligned}
$$

therefore:

$$
\begin{aligned}
A'(\omega) &= \cos\theta A(\omega) - \sin\theta D(\omega) \\
D'(\omega) &= \sin\theta A(\omega) + \cos\theta D(\omega)
\end{aligned}
$$

then,

$$
\int A'(\omega)d\omega = \cos(\theta)\int A(\omega)d\omega - \sin\theta\int D(\omega)d\omega \tag{2.6}
$$

$$
\int D'(\omega)d\omega = \sin(\theta)\int A(\omega)d\omega + \cos\theta\int D(\omega)d\omega \tag{2.7}
$$

if we calculate (Eq. 2.6)^2+(Eq. 2.7)^2:

$$
\begin{aligned}
&\left(\int A^{'}(\omega)d\omega\right)^2 + \left(\int D^{'}(\omega)d\omega\right)^2 \\
&= \cos^2\theta\left(\int A(\omega)d\omega\right)^2 + \sin^2\theta\left(\int D(\omega)d\omega\right)^2 - 2\sin\theta\cos\theta\int A(\omega)d\omega\int D(\omega)d\omega \\
&+ \sin^2\theta\left(\int A(\omega)d\omega\right)^2 + \cos^2\theta\left(\int D(\omega)d\omega\right)^2 + 2\sin\theta\cos\theta\int A(\omega)d\omega\int D(\omega)d\omega \\
&= \left(\int A(\omega)d\omega\right)^2 + \left(\int D(\omega)d\omega\right)^2
\end{aligned}
$$

and that

$$
\begin{aligned}
U_{\text{observed}} &= |U_{\text{time}}(0)| \\
&= \frac{1}{2\pi}\left|\int A(\omega) + iD(\omega)d\omega\right| \\
&= \frac{1}{2\pi}\left[\left(\int A(\omega)d\omega\right)^2 + \left(\int D(\omega)d\omega\right)^2\right]^{\frac{1}{2}}
\end{aligned}
$$

To conclude, the observed voltage can be calculated from time domain signals with any random phase as follows:

$$
\begin{aligned}
U_{\text{observed}} &= |U_{\text{time}}(0)| \\
&= \frac{1}{2\pi}\left[\left(\int A^{'}(\omega)d\omega\right)^2 + \left(\int D^{'}(\omega)d\omega\right)^2\right]^{\frac{1}{2}}
\end{aligned}
$$

2.3 Results and Discussion

Figures 2.2a and b illustrate very large enhancement of the LF NMR signal by D-DNP: the signal from a 160-fold diluted DNP sample in the cell tipped at a flip angle of $\pi/50.5$ is still much larger than the signal of the thermally polarized sample tipped by the $\pi/2$ flip angle. Because the D-DNP sample is hyperpolarized outside of the spectrometer, the optimization of transfer of the sample into the measurement cell is important. To this end, the time dependence of NMR signals obtained from the flow cell during the injection of the hyperpolarized sample was investigated (the upper panel of Figure 2.2c). It can be seen that the sample magnetization gradually increases and decreases as the hyperpolarized bolus flows through the cell. To monitor the concentration of radicals and dynamics of injection, an optical extinction measurement was also performed (the lower panel of Figure 22.2c) at the same time with the NMR measurement. The optical extinction indicated scattering in the sample caused by transiently appearing gas bubbles due to the use of pressurized gas for sample injection; however, after the sample had become stationary, its concentration was determined with good accuracy. NMR spectroscopy, on the other hand, was not affected by gas bubbles.

In addition to time-evolution measurements coming from the whole sample, the 1D distribution of polarized sample was measured using NMR with one constantly applied gradient along the axis of the cell (Figure 2.2d). It can be seen that the distribution of the polarized spins changed over a time of several seconds of sample injection, building up on one side of the cell and then spreading over the whole cell. More generally, this visualization can be used to study the dynamics of fluid motion in the cell resulting from high pressure injection.

From the analysis of the dynamics, we found that the sample volume yielding the

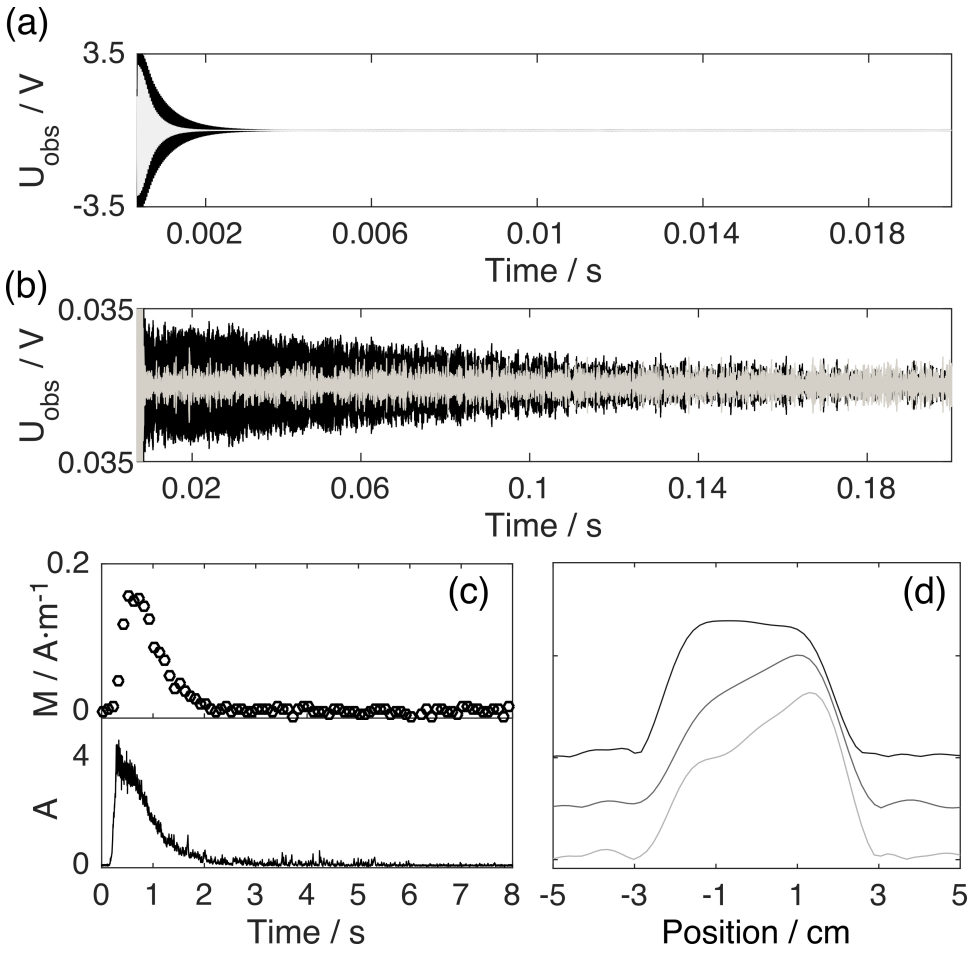

Figure 2.2: a) A single scan free induction decay (FID) from hyperpolarized water (15 mM TEMPOL during DNP polarization) excited with a π/50.5 pulse (black curve); b) FIDs averaged 2048 times from thermally polarized sample at $B_0 = 0.73281$ mT excited with π/2 pulses. Gray data lines represent the signal from background and pulse voltages in the absence of sample. c) Upper panel: Spin magnetization obtained from successive excitation during injection of samples into the flow cell acquired with 15 successive π/100 excitations in intervals of 0.1 s. Lower panel: A Optical extinction (A, defined in the text) measured during sample injection. d) Stopped-flow one-dimensional NMR images obtained along the cell that show the distribution of the polarization in the cell at different delay times, from bottom to top: 5 s, 10 s, 15 s.*

largest NMR signal can be captured in the flow cell by switching the injection valve after the optimal time determined from Figure 2.2c. Switching the injection valve pinches the flow at the inlet and the outlet of the cell, making the sample stationary. This

*Reprinted with permission from "Milli-tesla NMR and Spectrophotometry of Liquids Hyperpolarized by Dissolution Dynamic Nuclear Polarization" by Zhu, Y.; Chen, C.-H.; Wilson, Z.; Savukov, I. M.; Hilty, C., **2016**. *Journal of Magnetic Resonance*, *270*, 71-76, Copyright 2016 by Elsevier Inc.[63]

stopped-flow method can be used to characterize the hyperpolarized sample in terms of NMR signal frequencies, relaxation rates or other observable parameters. A sequence of NMR signals obtained from multiple small flip angle excitations can for example be used for measuring spin-lattice relaxation time.[86] Time-domain data, as well as integrals of the Fourier transformed NMR signals obtained from such a sequence are shown in the panels of Figures 2.3a and b, respectively.

From a fit of the time-domain signal (Figure 2.3a; the amplitude of $0.402V$ corresponds to a bulk magnetization of 0.186 Am^{-1} or a bulk polarization of $2.26 \cdot 10^{-4}$) or from the integrated peak areas in the spectrum (Figure 2.3b), the initial signal amplitude can be found, allowing for the determination of bulk magnetization and polarization according to Eq. 2.2 – 2.3. The resulting polarization values obtained at different radical concentrations are listed in Table 2.1. For comparison, data from the integrated area of the spectrum from Figure 2.2b's FID, the bulk polarization for water that has been thermally polarized in the measurement field was determined to be $2.41 \cdot 10^{-9}$, which is in good agreement with the expected value of $2.50 \cdot 10^{-9}$ at $T = 300$ K. Consequently, the hyperpolarization leads to a bulk signal enhancement of $9.4 \cdot 10^4$ even after the dilution of the originally polarized aliquot.

Since this data stems from hyperpolarized water, which has been further diluted with unpolarized water during sample injection, bulk polarization as discussed above represents a reasonable parameter to characterize the signal intensity. However, the D-DNP experiment allows hyperpolarization of a large number of different substances, not necessarily identical to the solvent used for dissolution, and with particular large signal enhancement, it becomes possible to study highly dilute analyte by LF NMR. Therefore it is of interest to consider the polarization level in the flow cell of the originally

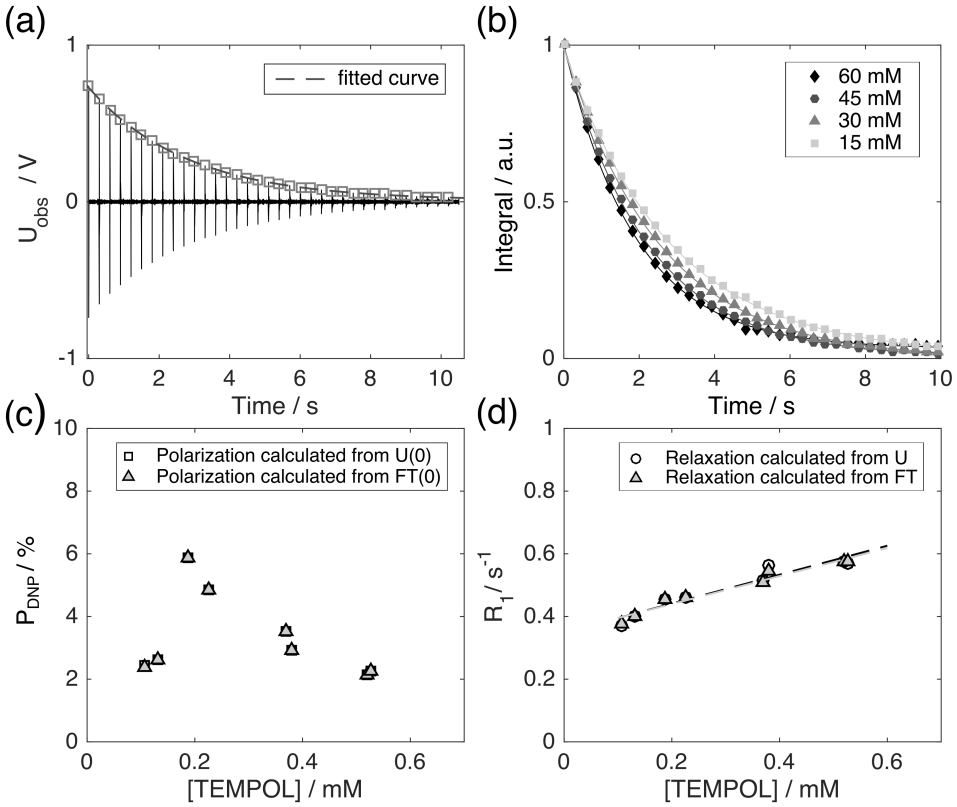

Figure 2.3: a) NMR time domain signal measured by successive $\pi/50.5$ pulses applied to the DNP hyperpolarized sample with 15 mM TEMPOL. Open squares indicate the maximum observed voltage from each scan. The electrical signal from rf pulses is removed by subtracting a scan when no sample was injected. b) integrated peak areas of the signal spectra obtained from hyperpolarized samples with different TEMPOL concentrations for measurement of spin-lattice relaxation time. Shown in the legend are TEMPOL concentrations during hyperpolarization, *i.e.* before dilution. c) Polarization of hyperpolarized sample as a function of TEMPOL concentration. d) Measured spin-lattice relaxation time as a function of the TEMPOL concentration as determined by the optical measurement.*

hyperpolarized sample material. This polarization level can be calculated from the bulk magnetization using the dilution factor determined by an optical measurement of TEMPOL concentration of the stationary sample in the flow cell. For the data from Figure 2.3a, the polarization level of the originally hyperpolarized component was 2.40 %, whereas at optimal radical concentration, it was increased to close to 6 % (Table 1).

*Reprinted with permission from "Milli-tesla NMR and Spectrophotometry of Liquids Hyperpolarized by Dissolution Dynamic Nuclear Polarization" by Zhu, Y.; Chen, C.-H.; Wilson, Z.; Savukov, I. M.; Hilty, C., **2016**. *Journal of Magnetic Resonance*, *270*, 71-76, Copyright 2016 by Elsevier Inc.[63]

Table 2.1: Calculated polarization levels and related data. Values in columns are: c_{DNP} — radical concentration in hyperpolarized aliquot, c — radical concentration in cell calculated from optical signal, U_{observed} — voltage observed from photodiode, M_{bulk} — bulk magnetization calculated based on Eq. 2.2, P_{DNP} — polarization level calculated based on Eq. 2.3. FID and Fourier Transform data gave essentially the same results.

c_{DNP} (mM)	c (mM)	U_{observed} (V) (FID)	U_{observed} (V) (FT)	M_{bulk} (Am^{-1}) (FT)	P_{DNP} (%) (FT)
15	0.130	0.402	0.403	0.187	2.64
15	0.107	0.304	0.302	0.140	2.39
30	0.187	0.646	0.649	0.300	5.9
30	0.227	0.648	0.651	0.301	4.85
45	0.379	0.434	0.435	0.201	4.85
45	0.370	0.514	0.514	0.238	3.54
60	0.519	0.323	0.326	0.151	2.14
60	0.526	0.352	0.351	0.163	2.26

In addition to the initial signal intensity, the same data allow the quantification of paramagnetic relaxation enhancement (PRE) under the low field measurement conditions. A plot of the relaxation rates obtained at different radical concentrations present in the cell after dilution of the sample is shown in Figure 2.3d. The resulting fitted line gives a relaxivity of $\epsilon = 0.45\ \text{s}^{-1}\text{M}{-1}$ under the conditions of measurement field of 0.7 mT, which is significantly larger than at high field, $\epsilon = 0.133\ \text{s}^{-1}\text{M}^{-1}$ at 300 K. The measurement field employed here corresponds closely to that encountered in the injection path between a DNP polarizer and a high-field NMR magnet.[87] The low field R_1 measurement can therefore serve as an indicator of signal loss due to relaxation during sample injection in a D-DNP experiment and can be used for the optimization of polarization transfer. Comparison of the ^{1}H data obtained here with ^{13}C relaxation data measured by Miéville *et al.*[87] suggests that low field relaxation plays an even more important role in the case of dissolution DNP experiments using ^{1}H.

The data in Figure 2.3c most interestingly illustrate substantial polarization gain at

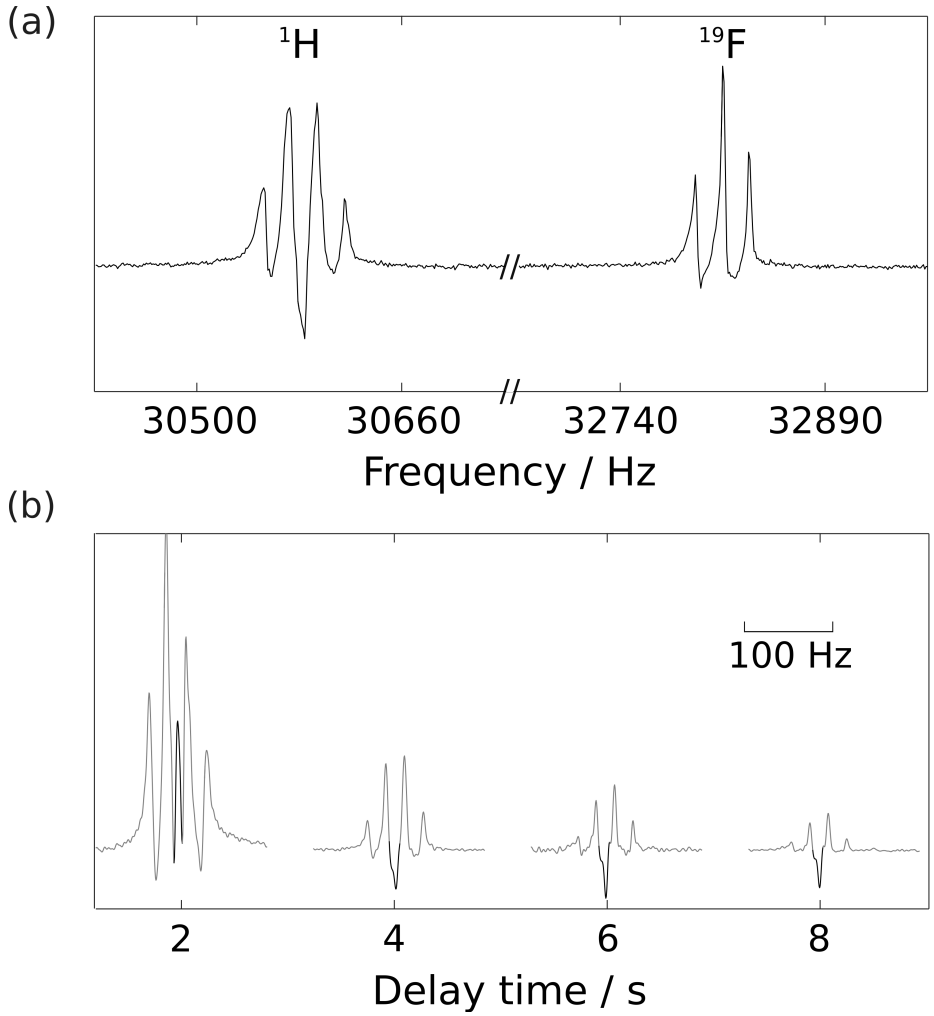

Figure 2.4: a) FT spectrum of hyperpolarized trifluoroethanol (TFE; CF_3CH_2OH) acquired $4s$ after injection into the low field NMR using presurrized water. b) Enlarged spectral region corresponding to proton signal, from separate experiments measured at different delay times. The central line corresponding to protons without observable J-coupling is highlighted with dark color.*

the optimal radical concentration, arising from a combination of solid state polarization efficiency and losses during sample injection. It can also be noted that under the conditions yielding highest polarization ($30mM$ during polarization, resulting in 0.2 mM after dissolution), the paramagnetic contribution to the overall relaxation rate of $R_1 = 0.46$ s^{-1}

*Reprinted with permission from "Milli-tesla NMR and Spectrophotometry of Liquids Hyperpolarized by Dissolution Dynamic Nuclear Polarization" by Zhu, Y.; Chen, C.-H.; Wilson, Z.; Savukov, I. M.; Hilty, C., **2016**. *Journal of Magnetic Resonance*, *270*, 71-76, Copyright 2016 by Elsevier Inc.[63]

is still modest.

In addition to the determination of T_1 relaxation and its effect on polarization of samples in the D-DNP experiment, LF NMR permits the study of other phenomena such as cross-relaxation. The large spin polarization produced by D-DNP can significantly enhance the otherwise weak signals due to the nuclear Overhauser effect. In high-field NMR, in particular for the determination of heteronuclear cross-relaxation, this measurement however requires specialized multi-channel detectors.[88] An interesting feature of LF NMR in this regard is the dramatically reduced frequency bandwidth, resulting in the ability to obtain signals from distinct nuclei in the same spectrum. In Figure 2.4, the signal evolution due to ^{1}H, ^{19}F-NOE effect is observed after injection of hyperpolarized 2,2,2-Trifluoroethanol (TFE) mixed with water. Although microwave frequency was adjusted for optimal ^{19}F polarization, the presence of ^{1}H polarization is also expected. Signals at the frequency of both nuclei are observable (Figure 2.4a) and are split with the respective *J*-coupling. The multiplet structures are a triplet for the CF_3 group of TFE coupled to CH_2, a quartet for the CH_2 group of TFE coupled to CF_3, and a singlet for the OH groups of TFE and water. Although in a spectrum acquired shortly after injection, hyperpolarized signals from all components are observed, the singlet signal becomes inverted at later time (Figure 2.4b). This behavior is explained by the NOE from hyperpolarized ^{19}F and ^{1}H spins of the CF_3 and CH_2 groups of TFE. Using D-DNP hyperpolarized NMR therefore allows the direct observation of NOE buildup curves at low field, which would otherwise be subject to prohibitive sensitivity limits. Such curves may in the future be used for determining the dynamics of intermolecular interactions and other physical properties of solvent-solute mixtures.

2.4 Conclusion

In summary, we have described a low field NMR experiment capable of characterizing compounds hyperpolarized by D-DNP. A combination of NMR signal acquisition with in situ concentration determination by laser based spectrophotometry allowed quantification of spin-lattice relaxation properties in relationship with the concentration of the free radical employed for DNP hyperpolarization. Since these relaxation rates contribute to the losses of hyperpolarization during sample injection in typical D-DNP experiments, the present measurement provides a basis for optimizing the high-field D-DNP experiment. Further, the nuclear Overhauser effect at low field can readily be observed between different nuclei or between the same nuclei with different coupling multiplicity. This observation opens a new NMR frequency regime for the determination of the dynamics of intermolecular interactions by cross-relaxation.

3. MULTINUCLEAR DETECTION OF NUCLEAR SPIN OPTICAL ROTATION AT LOW FIELD*

3.1 Introduction

Optical detection of nuclear magnetic resonance (NMR) is currently being proposed for applications that benefit from sensitivity enhancement at low field, such as enabling spectroscopy and imaging at low cost.[74,89,90] These detection methods are based on optical magnetometry, using nitrogen vacancy centers in diamond or optically pumped alkali vapor as sensitive probes for nuclear spin magnetization. A different magneto-optical effect, nuclear spin optical rotation (NSOR) exists, which is based on electronic transitions of a molecule. While not proposed for applications in sensitivity enhancement, this effect may instead be used to provide new spectroscopic information on the molecule.[1,18,26–28] NSOR is in essence a nuclear spin induced Faraday rotation. The Faraday effect itself describes the rotation of optical polarization in a medium induced by a magnetic field.[91,92] In case of a long cylindrical sample, The Faraday rotation induced by the magnetization of nuclear spins can be expressed as:

$$\Delta\theta = \varphi_{\text{fr}} \cdot B \cdot l = \varphi_{\text{fr}} \cdot \mu_0 \cdot N \cdot \mu_{\text{I}} \cdot l \tag{3.1}$$

where φ_{fr} is the Verdet constant, $\mu_0 = 4\pi \cdot 10^{-7}$ NA^{-2} is the vacuum permeability, $N \cdot \mu_{\text{I}}$ is the macroscopic nuclear spin magnetization in the propagation direction of the light, and l is the path length. The magnitude of the expected nuclear spin induced optical rotation can be estimated by considering the Faraday rotation that would be caused by the

*Reprinted with permission from "Multinuclear Detection of Nuclear Spin Optical Rotation at Low Field" by Zhu, Y.; Gao, Y.; Rodocker, S.; Savukov, I. M.; Hilty, C., **2018**. *The Journal of Physical Chemistry Letters*, *9*, 3323-3327, Copyright 2018 by American Chemical Society[29]

overall magnetization created by nuclear spins in the medium. However, more probable localization of electrons near the magnetic dipole moments of nuclear spins can result in an enhancement of the polarization rotation.[43,47] The polarization rotation angle can be written as:[18]

$$\Delta\theta = \varphi_{\text{nsor}} \cdot [C] \cdot P \cdot l \tag{3.2}$$

Here, $[C]$ is the nuclear spin concentration and P the nuclear spin polarization. The NSOR constant φ_{nsor} arises from the vector polarizability α_{v} of electrons interacting with nuclear spins.

$$\varphi_{\text{nsor}} = \frac{\pi\omega\hbar}{nc}\alpha_{\text{v}} \cdot N_m \tag{3.3}$$

The vector polarizability can be estimated using the following expression, which reveals its dependence on frequency similar to that of Verdet constant.

$$\alpha_{\text{v}} = \frac{2\omega r_{\text{e}} c^2}{\hbar} \sum_k \frac{f_k a_k}{\left(\omega_k^2 - \omega^2\right)^2} \tag{3.4}$$

The NSOR constant at the optical frequency ω depends on the transition frequency ω_k and oscillator strength f_k, in addition to the hyperfine interaction with a nuclear spin described by the hyperfine coupling constants $H_k^{\text{hf}} = a_k \text{L} \cdot \text{I}$. L is the orbital angular momentum of electrons, I the nuclear spin angular momentum, r_{e} the classical electron radius, and n the refractive index of the sample. N_{m} is a unit conversion factor equal to Avogadro's number per unit volume, and c the speed of light.

The NSOR effect can uniquely be used to probe excited electronic states and potentially offers new information on related molecular properties, which is not readily

available from other spectroscopic techniques.[17,93] Because of the dependence on the electronic polarizability, the NSOR effect is strongly enhanced for heavy atoms and ions, and also depends on chemical identity.

Methods to measure NSOR have been developed in several contexts. Most commonly, NSOR has been detected using a radio-frequency induced spin lock, which results in a continuously precessing nuclear spin magnetic moment, and concomitantly in an optical signal at the respective Larmor frequency.[1,18,28] This method conveniently works at low magnetic fields of low uniformity, which results from the use of long samples, and can be adapted to allow for measurement of precise NSOR constants. The use of spin lock in the case of non-uniform field at the same time prevents the detection of frequency resolved spectra. At high magnetic field, NSOR has been used with spin-echo pulse sequences to measure chemical shift resolved spectra of several compounds.[27] The main disadvantage of this method is various restrictions imposed on the sample geometry inside a standard spectrometer, which is designed to hold a standard NMR tube.

Frequency resolution at low field does not contain chemical shift information. However, it does allow for the simultaneous detection of multiple nuclei, and for obtaining chemical information by *J*-spectroscopy.[70,72,73]

Here, we describe a frequency resolved measurement of NSOR at low field, which distinguishes signals from nuclei of different types and demonstrates a possibility for localized optical spectroscopy. For this purpose, we adapt a recently described spectrometer capable of simultaneous low-field NMR and optical spectroscopy measurements.[63] Simultaneously measured NMR and NSOR of liquids containing ^{19}F and ^{1}H are obtained and NSOR constant are calculated.

3.2 Experimental Section

3.2.1 Experimental Setup

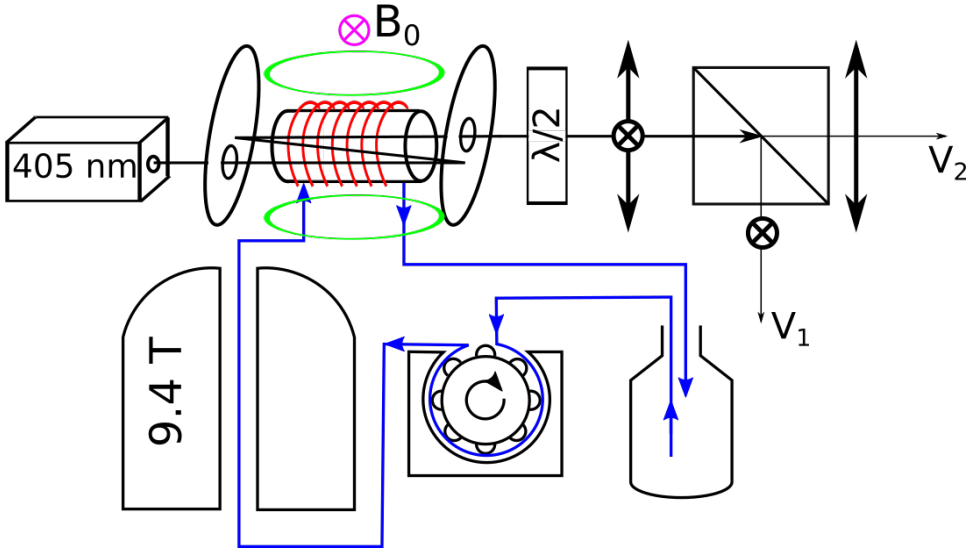

Figure 3.1: The experimental setup for low-field NSOR measurement. The sample cell, a small cylinder with two connections for in and out flow of sample on the side, is wounded with a receiver coil. A peristaltic pump causes flow from a sample reservoir through a 9.4 T superconducting magnet to the sample cell. A pair of excitation coils is enclosing the sample cell, with an axis perpendicular to the receiver coil. The main field B0 is homogenized by three pairs of shim coils (not shown in the figure). A 405 nm diode laser, two flat mirrors, the sample cell, a half-wave plate and a beam splitter are positioned on a straight line with sample cell in-between the mirrors. The split laser beams are detected using two photodiodes.*

The low field NSOR measurement was implemented as shown in Figure 3.1. A glass bottle served as the sample reservoir. Fluid flow was induced by a peristaltic pump head (Watson-Marlow, Wilmington, MA) powered by a DC power supply (6553A, Hewlett Packard, Palo Alto, CA). Sample was circulated through the glass bottle, the pump head, a 9.4 T magnet, the sample cell (Precision Glassblowing of Colorado, Centennial, CO) and

*Reprinted with permission from "Multinuclear Detection of Nuclear Spin Optical Rotation at Low Field" by Zhu, Y.; Gao, Y.; Rodocker, S.; Savukov, I. M.; Hilty, C., **2018**. *The Journal of Physical Chemistry Letters*, *9*, 3323-3327, Copyright 2018 by American Chemical Society[29]

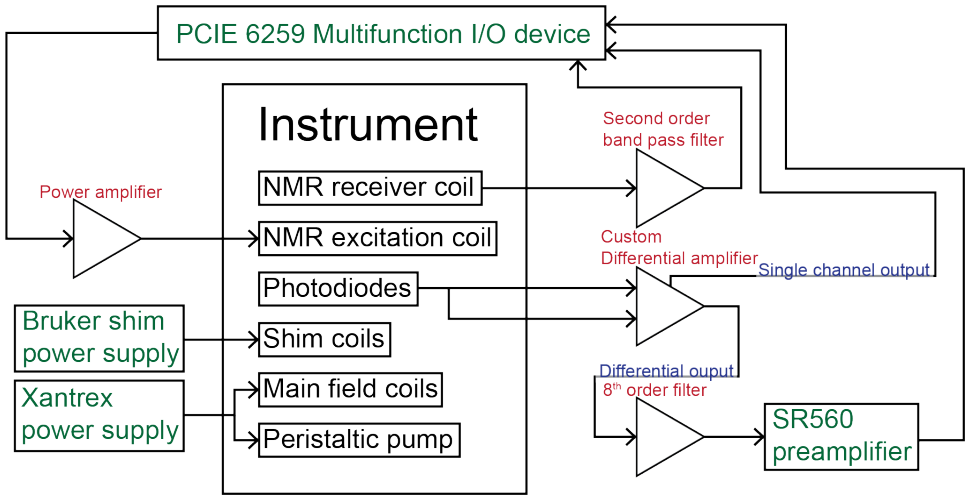

Figure 3.2: The connections in the instrument. Green texts represents the commercial devices; red texts represents the home-built circuits; blue texts represents the two different outputs from differential amplifier. The hardware signals are hubbed by a PCIE-6259 board, which is interfaced with a Labview program.

then returning to the glass bottle.

The NMR spectroscopy equipment was similar to that described previously.[63] Briefly, a tetra coil[94] was employed to generate the main magnetic field B_0. This coil was powered by a digitally regulated linear power supply (XDL35-5TP, Xantrax, Elkhart, IN). A set of shim coils in the x, y, and z direction was mounted concentrically with the tetra coil controlled by a dedicated shim power supply (Bruker Biospin, Billerica, MA). The excitation coils were arranged as a Helmholtz pair to provide a more homogeneous excitation field along the cell. The excitation waveform was first sent from a data acquisition board (PCIe-6259, Nation Instruments, Austin, TX) to a homemade amplifier based on a power operational amplifier (TCA0372DP1, Motorola, AZ) with a voltage gain of 2, and then delivered to the excitation coils. The receiver coils were wound on the sample cell, the axis of which was perpendicular to both the axis of the excitation coil and the axis of tetra coil. The received NMR signal was sent to the acquisition board via a homemade second order band-pass filter with a gain of 9.67 (first order high-pass filter

at 10 kHz and first order low-pass filter at 100 kHz) implemented using a high speed, precision operational amplifier (AD712JR, Analog Devices, Norwood, MA).

A 405 nm diode laser with adjustable intensity (L4405M-100-TE/2mm/ESYS, Micro Laser Systems, Garden Grove, CA) was used as the source of light for measuring the Faraday rotation. It was sent through the cell and two flat mirrors (Thorlabs, Newton, NJ) were used to reflect it two times to realize three passages. The outcoming laser beam was divided by a beam splitter (PBS121, Thorlabs) to create two linearly polarized beams. These beams were adjusted to equal intensity by rotating a half wave plate (WPH10E-405, Thorlabs) between the cell and the beam splitter. Two calibrated photodiodes (FDS100-CAL, Thorlabs) were used to measure the laser intensity in both beams. The photo-detector currents were transformed into voltages by a home-built transimpedance amplifier based on a low-noise operational amplifier (OPA4131PJ, Texas Instruments, Dallas, TX). One output was sent to the data acquisition board, while the difference between two photo-diode signals was further processed. It was filtered and amplified in three stages before being sent to the acquisition board. The first stage was amplification of adjustable gain in the range from 4 to 120 (circuit is based on AD712, Analog Devices). The second stage consisted of an 8^{th} order band pass filter (28 kHz to 34 kHz) with unity gain implemented with a continuous-time active filter chip (MAX274, Maxim Integrated, San Jose, CA). The third stage contained an adjustable gain and a band-pass filter (SR-560, Stanford Research Systems, Sunnyvale, CA).

The connections of the electronics are shown in Figure 3.2.

3.2.2 Electronics

The differential amplifier is shown in Figure 3.3. There are two inputs from the photodiodes. Since the photodiodes are current sources, a transimpedance stage is used to

convert current to voltage before taking the differential of the two. The photodiode can be viewed as a current source with a capacitor in parallel. Since oscillation can occur if the difference in phase between the input and output signals exceed 360 degrees, a bypass capacitor parallel with the feedback resistance is added for stabilization. The value of the capacitor can be calculated as:[95]

$$C_p = \frac{1 + \sqrt{1 + 8\pi R_F C_i f_{\text{GBWP}}}}{4\pi R_F f_{\text{GBWP}}}$$

where $R_F = 5$ kΩ is the feedback resistance, $C_i = 24$ pF the junction capacitance of the photodiode, $f_{\text{GBWP}} = 2.5$ MHz is the gain bandwidth product of the operational amplifier. After calculation, the bypass capacitance is determined to be $C_p = 25$ pF.

The second stage of this circuit is a standard differential amplifier, with the gain of 1. Since in the NSOR experiment the laser intensity is needed for calculation of light rotation angle, the voltage is detected immediately after one transimpedance amplification stage.

The 8$^{\text{th}}$ order band pass filter was designed based on a DOS progrom provided by Maxim Integrated. The MAX274 EV Kit was used for the layout of the chip. The chip contains 4 stages of a 2$^{\text{nd}}$ order band pass filter and therefore adding together to be 8$^{\text{th}}$ order. The four resistors in each stage determines the bandpass range and is listed in Table 3.1. The resulted response curve is shown in Figure 3.4. It is clear that the the 8$^{\text{th}}$ order filter is covering the intended frequency range from 29 kHz to 33 kHz and has a uniform gain of about 2.3. The curve was fit from a 8$^{\text{th}}$ order Gaussian function as follows:

$$\text{Gain} = a_1 \cdot e^{(-(f-f_0)^2/b_1)} + a_2 \cdot e^{(-(f-f_0)^4/b_2)} + a_3 \cdot e^{(-(f-f_0)^6/b_3)} + a_4 \cdot e^{(-(f-f_0)^8/b_4)}$$

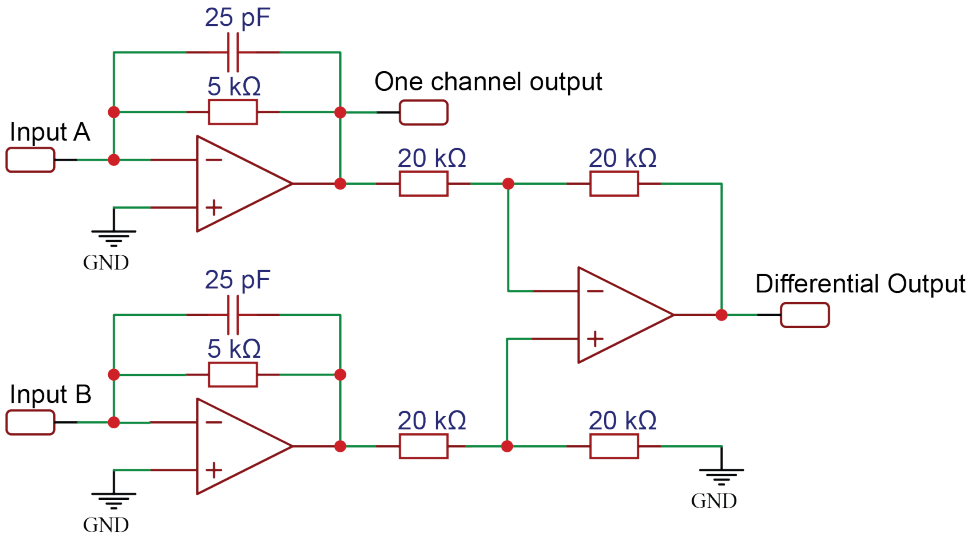

Figure 3.3: The Diagram of the differential amplifier. The resistance and capacitance values are shown above each element in blue color. The two inputs and two outputs are represented by round-corner squares.

The fit result is $f_0 = 31.360$, $a_1 = 2.0977$, $b_1 = 9.3125$, $a_2 = 2.1737$, $b_2 = 38.497$, $a_3 = -1.6804$, $b_3 = 50.273$, $a_4 = -0.29524$, $b_4 = 0.30641$.

Table 3.1: Resistor values used in the MAX 274.

Stages	R1 (kΩ)	R2 (kΩ)	R3 (kΩ)	R4 (kΩ)
A	86.6	69.8	226	63.4
B	82.5	66.5	88.7	60.4
C	76.8	61.9	84.5	57.6
D	75.0	59.0	196	54.9

3.2.3 NMR Spectroscopy

For water sample, the NMR signal was detected in a static magnetic field of 0.7328 mT (1.753 A current in the coil) using a Carr-Purcell-Meiboom-Gill (CPMG) pulse sequence

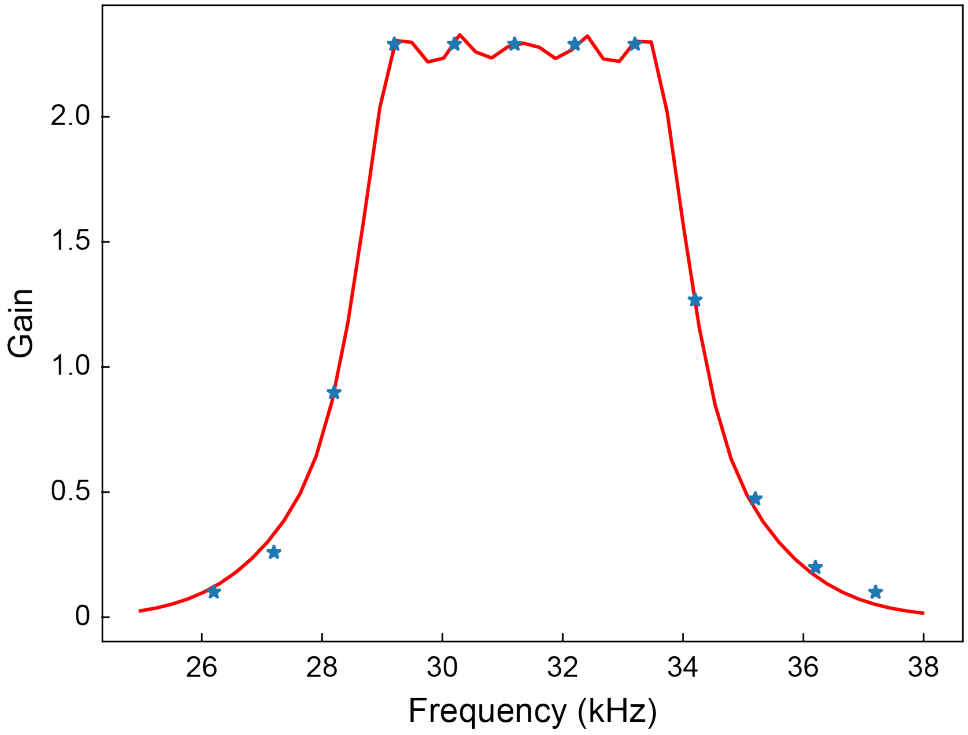

Figure 3.4: The response curve from the resulted 8th order filter. The tested data points are shown in blue stars and the red curve was a fit from 8th order Gaussian function.

p90$[-\tau$ − p180 $-\tau] \times n$ at the frequency of 31,200 Hz, where τ was 0.01 s. For trifluoroethanol (TFE) / water mixture, the field was changed to 0.7711 mT to fit both proton signal (32,832 Hz) and fluorine signal (30,869 Hz) into the spectrum. The duration of the 90° radio frequency (rf) pulse (p90) was 0.45 ms, and the duration of the 180° pulse (p180) was 0.9 ms. These pulse lengths were calibrated from a nutation curve experiment. In addition, τ was reduced to 0.005s in observation of a faster decay of TFE signals. Data acquisition occurred continuously during the entire pulse sequence, for a total of 305,382 data points acquired over a duration of 0.61 s. Four thousand averages were collected in each data set, and phase cycling of (x,-x) on p90 and receiver was employed in order to eliminate the signals from the 180° pulses in the final data. The time domain data was Fourier transformed and phased. Phasing was achieved by maximizing the peak amplitude by adjusting x in $\sin x \cdot \Re(FT) + \cos x \cdot \Im(FT)$, where FT is the complex valued Fourier transform of real time domain data. The peak was integrated to obtain the amplitude of the NMR signal, represented as U_{NMR}.

After integration, the polarization level of the sample was calculated based on the resulting signal voltage, following[28]

$$P = \frac{U_{\text{NMR}}}{[C]\mu_{\text{I}} 2\pi^2 f \mu_0 w a_{\text{c}}^2 g N} \tag{3.5}$$

where $[C]$ is the number density of nuclear of interest in the sample solution, μ_{I} the magnetic moment of the nuclear spin, f the signal frequency, μ_0 the vacuum permeability, w the number of detection coil turns, a_{c} the radius of sample, g the preamplifier gain, N the number of averages.

3.2.4 NSOR Detection

Photocurrent from one photodiode, U_{1ch}, was recorded to serve as a reference for total signal intensity. Since the two channels were adjusted to be of the same intensity, the total intensity of the signal was calculated to be two times the one channel signal. The amplified (with gain of $g_{\text{n}} = 7260$) and filtered differential intensity, U_{diff}, was recorded as the NSOR signal. This signal was processed the same way as the NMR signal (Fourier transform and integration over the signal peak). The resulting NSOR angle was calculated as

$$\Delta\theta = \frac{U_{\text{diff}}}{4 \cdot U_{\text{1ch}} \cdot g_{\text{n}}} \tag{3.6}$$

Using the known NSOR constant for water ($\varphi_{\text{water}} = 9.02 \cdot 10^{-7}\text{rad M}^{-1}\text{cm}^{-1}$) [19], the path length of the laser was calculated based on equation 2.2:

$$l = \frac{\Delta\theta}{\varphi_{\text{water}}[C]P} \tag{3.7}$$

The NSOR constants for other liquids were calculated using the same equation.

3.2.5 Light Path Length Calibration

The relationship between polarization level P calculated out of the NMR signal and flow rate Q measured by recording time required for filling a 100 mL graduated cylinder is determined by fitting the two with $P = P_0 \cdot (1 - e^{a/Q}) \cdot e^{b/Q}$, where $P_0 = 3.2 \cdot 10^{-5}$ is the equilibrium polarization level inside the 9.4 T magnet, a and b are the fitting parameters. The fit equation is derived from $P = P_0 \cdot (1 - e^{-t_1/T_{1\text{H}}}) \cdot e^{-t_2/T_{1\text{L}}}$, where $t_1 = V_1/Q$ is the residence time for water in the magnet, V_1 the fluid volume in the magnet, $T_{1\text{H}}$ the spin-lattice relaxation at 9.4 T, $t_2 = V_2/Q$ the travel time from the 9.4 T magnet to the cell,

V_2 the tubing volume between magnet and flow cell, and T_{1L} the spin-lattice relaxation at low field.

3.3 Results and Discussion

Simultaneously acquired NMR and NSOR signals of recirculated water with different flow rates are shown in Figure 3.5a. With a flow rate of 150 $\sim$ 300 mL·min^{-1} and a NMR sensitive volume of the detection region of 3.02 mL, the residence time of the liquid in the detection region is 0.6 $\sim$ 1.2 s. Because of the application of the CPMG pulse sequence, decay of the NMR signal in time domain is governed by this residence time, rather than by magnetic field inhomogeneity. For comparison, the signal lifetime of a free induction decay measured after a single 90° pulse without shimming was approximately 0.1 seconds under the same experimental conditions. The use of the CPMG pulse sequence therefore significantly prolongs the signal observation time for each scan and increases the signal-to-noise ratio (SNR) in the resulting spectrum. Although the time domain trace represents an uninterrupted acquisition, signals from the pulses themselves are not visible because of the phase cycling that was applied. A short duration of 20 ms between the 180° refocusing pulses for CPMG was chosen, such that the intensity variation at the beginning and end of each echo is not significant.

The lower SNR in the NSOR prevents direct observation of water in the time domain. However, after Fourier transform, a NSOR peak is clearly visible (Figure 2b). In this spectrum, we can see that the 8th order filter effectively removed noise outside of the desired spectral region, thereby allowing the use of a higher gain in the pre-amplification and resulting increase in SNR.

Because of the continuous nature of the resulting signal, the Fourier transform was performed of the entire echo train, as opposed to of a single echo. This procedure resulted

in a spectrum with a frequency resolution that is higher by a factor of the number of echoes, compared to the frequency resolution available from a single echo. The echo time of 20 ms then results in the observation of spectra with side-bands spaced every 50 Hz due to variation of the amplitude between echoes. The side bands are clearly visible in the NMR signal in Figure 2c, but are below the noise level in the NSOR spectrum in Figure 2d.

Since the weaker signal in the NSOR channel is at the same frequency as that in the NMR channel, we further acquired control experiments with the laser light blocked. In these experiments, shown as the solid trace in Figures 3.5 b, no signals in the NSOR channel were detectable. This result confirms the absence of observable crosstalk between the NMR and NSOR signal channels. Comparing the spectrum in Figure 3.5b also shows the increase in the noise that is due to the laser light itself. In the spectral region between 32,000 Hz and 33,000 Hz, which is not expected to contain signals, an increase in V_{rms} of $2.2 \cdot 10^{-4}$V Hz$^{-1/2}$ before amplification is observed.

Shot noise is independent of the temperature and frequency, unlike flicker noise and Johnson-Nyquist noise. Therefore, the it dominates the electronic noise in our circuit at 30 kHz and room temperature. The expected shot noise is usually calculated in time domain by using $I_{\text{rms}} = \sqrt{2 \cdot e \cdot I \cdot \Delta f}$ where e is the electron charge, I is the current level in the circuit, Δf is the bandwidth of the instrument.[96] Although a band-pass filter has been applied during the signal acquisition, the shot noise level will be the same in all spectral regions. It is useful to consider Parseval's theorem in the noise conversion from frequency domain to time domain. Parseval's theorem states that in the discrete Fourier Transform, $\sum x^2(t) = (1/N) \sum X^2(f)$, where $x(t)$ is the time domain data series and $X(t)$ is the corresponding Fourier Transformed frequency domain data series and N is the total number of data points. According to the definition of RMS current, $I_{\text{rms}} = \sqrt{\sum I(t)^2}$, which equals to $\sqrt{(1/N) \cdot \sum I(f)^2}$ according to Parseval's theorem. This

indicates that the RMS current noise in the frequency domain equals to the RMS current noise in time domain times a factor of $\sqrt{N}$. When calculating the theoretical noise level, the bandwidth Δf should be considered as the lower frequency of the sampling bandwidth of the analog to digital converter (ADC) or the photodiode. The photodiode's bandwidth can be calculated as $f_{\mathrm{BW}} = 1/(2\pi R_L C_J)$, where R_L is the load resistance and C_J is the junction capacitance of the capacitor. The photodiode we use has a junction capacitance of 24 pF and the load resistance is 5 kΩ, so the bandwidth is about 1.3 MHz and the ADC frequency is 480 kHz. The lower bandwidth of the ADC is taken for further calculation of theoretical shot noise level.

From the described calculation above, the noise level is 4.2 times larger than the theoretical shot noise of $5.3 \cdot 10^{-5}$V Hz$^{-1/2}$ from the 100 mW laser radiation calculated from the from the photo-detector current and adding the noise from two separate photodetectors quadratically.

The magnitude of optical rotation due to NSOR depends on the optical path length. The flow rate of the liquid can affect the velocity field inside of the cell, which ultimately changes the effective beam path length. This effect was quantified by measuring water NSOR signals at different flow rates. First, the flow rate dependence of the polarization level inside of the flow cell was determined (Figure 1d). Next, from the water NSOR signals and using Equation 2, the effective path length of the optical beam within the NMR excitation region was calculated as a function of the flow rate (Figure 1e). Within the parameter range investigated, the effective path length was found to linearly depend on the flow rate. At a low flow rate of 2.5 mL/s, the effective light path length is 20.5 cm, which is in good agreement with the three passages through the actual cell length of 7.5 cm. At higher flow rate, the effective path length decreases in an effect that could arise

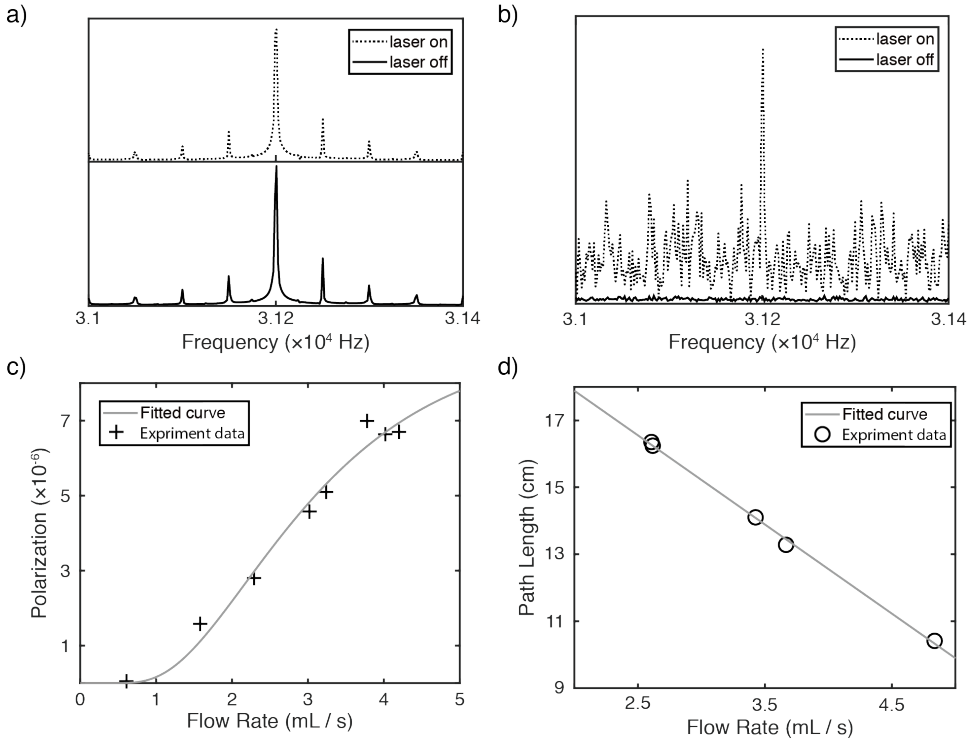

Figure 3.5: a) Expanded spectral region of water NMR signal with or without laser on and they show the same signal level from both measurements. b) Expanded spectral region of water NSOR signal with or without laser on and both a decrease in noise and signal disappearance is observed. c) Experimental data and fitted curve for the relationship of polarization levels with flow rate. The resulting fit curve is $P = 3.2 \cdot 10^{-5} \cdot (1 - e^{-5.99/Q}) \cdot e^{-5.264/Q}$. d) Calculated light path length correlated to flow rate. The flow rate calculation is based on the parameters obtained in (a) and the polarization level of the sample obtained from NMR spectrum. Path length is calculated based on the peak maximum of the NSOR spectrum and the known NSOR constant of water, and fitted with a linear equation $l = -3.35\text{cm s mL}^{-1} \cdot Q + 29.2\text{cm}$, where l is the effective path length and Q the volumetric flow rate.*

due to increased channeling of the flow field.

The capability for frequency resolved NMR/NSOR detection is demonstrated in Figure 3.6 with the acquisition of both proton and fluorine signals from a mixture of TFE and water at a mixing ratio of 1:1 v/v. Because of a shorter signal lifetime compared to DI water, a shorter echo time of τ = 10 ms was chosen. The phase cycling almost completely

*Reprinted with permission from "Multinuclear Detection of Nuclear Spin Optical Rotation at Low Field" by Zhu, Y.; Gao, Y.; Rodocker, S.; Savukov, I. M.; Hilty, C., **2018**. *The Journal of Physical Chemistry Letters*, *9*, 3323-3327, Copyright 2018 by American Chemical Society[29]

removes contributions from the pulses, which become invisible in the time domain signal in Figure 3.6a. In the magnetic field of 0.7711 mT, the two nuclei are detected with a frequency separation of 1963 Hz. This frequency range falls within the pass band of the 8^{th} order bandpass filter (see Methods section). Since the MAX274 device used in the filter is configurable with externally connected resistors, this frequency range can readily be adapted to the detection of other combinations of nuclei. The time domain signal of NMR (Figure 3.6a) shows an apparent decay of the signal in the detection period, which is faster than that of pure water. The spurious peaks in time domain are remainders of pulses that are not fully removed by phase cycling. In the real spectrum (Figure 3.6b), two peaks corresponding to fluorine (30869 Hz) and proton (32832 Hz) are seen. The ratio of the frequencies ($f_{\mathrm{H}}/f_{\mathrm{F}} = 1.0636$) reflects the relative magnitudes of the gyromagnetic ratios of the two nuclei. The expanded proton and fluorine NMR signals in Figure 3.7b clearly show the *J*-coupling multiplet structure. The $-CF_3$ peak appears as a triplet because of coupling to 2 protons, whereas $-CH_2$ is expected to be a quartet because of coupling to 3 fluorine atoms. However, only one major proton peak is seen. This peak does not show coupling, and therefore is attributed to OH of water and TFE. A lower signal strength of CH_2 protons may be caused by three factors: one, the low concentration of protons of TFE (22.6 M total in pure TFE and two thirds of that are $-CH_2$) compared to water (111 M in pure water); two, faster relaxation rate in $-CH_2$ group; three, quartet structure itself reduces the intensity of each signal in the pattern. A separate experiment using pure TFE as sample shows a similar feature, where only the center peak of $-$OH is visible, which indicates that relaxation is the major reason for the missing CH_2 peaks because proton signal can only be observed from $-$OH peak and $-CH_2$ peaks and the signal strength without considering relaxation is similar (OH: higher peak of CH_2 = 4:3).

For NSOR signal, the time domain signal of TFE can be observed (Figure 3.6c)

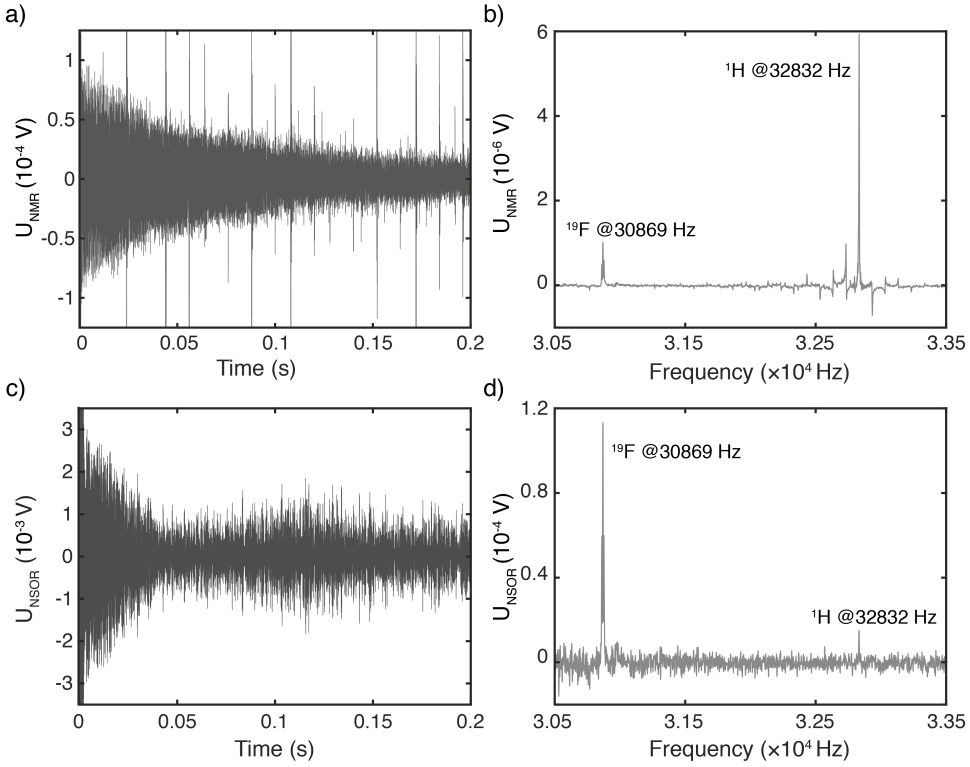

Figure 3.6: NMR and NSOR signals of recirculated trifluoroethanol/water mixture measured simultaneously from an experiment averaging 72,000 scans, each comprising 25 echoes with echo time $\tau = 10$ ms. a) Time domain NMR signals. b) Frequency spectrum of NMR signals. c) Time domain NSOR signals. d) Frequency spectrum of NSOR signals.*

although that of pure water was not observable. By examining the spectra of it (Figure 3.6d), It is clear that the time domain signal is mainly composed of F signal. Therefore, NMR time domain signal and NSOR time domain signal can to a certain extent be viewed as the spin-spin relaxation of proton and of fluorine respectively. Comparing Figure 4b and 4d, an opposite relative signal strength is observed between the H and F, which indicates that fluorine has a substantially higher NSOR constant compared to proton. The reason for this higher NSOR constant is in two fold: one is the stronger hyperfine interaction in heavier atoms[18] and the other is the high electronegtivity of fluorine.[1] The coupling

*Reprinted with permission from "Multinuclear Detection of Nuclear Spin Optical Rotation at Low Field" by Zhu, Y.; Gao, Y.; Rodocker, S.; Savukov, I. M.; Hilty, C., **2018**. *The Journal of Physical Chemistry Letters*, *9*, 3323-3327, Copyright 2018 by American Chemical Society[29]

patterns appeared in NMR spectrum are also reproduced in the NSOR signals. Therefore, chemical information through *J*-coupling would be available from NSOR measurements at low field even in the absence of simultaneous detection of NMR signals.

NSOR constants obtained from the individual signals of the fluorine and proton nuclei can also be obtained from this data (Table 3.2). The ratio of NSOR constants is obtained by using:

$$\frac{\varphi^{\mathrm{F}}_{\mathrm{NSOR}}}{\varphi^{\mathrm{H}}_{\mathrm{NSOR}}} = \frac{U^{\mathrm{F}}_{\mathrm{NSOR}}}{U^{\mathrm{H}}_{\mathrm{NSOR}}} \frac{U^{\mathrm{H}}_{\mathrm{NMR}}}{U^{\mathrm{F}}_{\mathrm{NMR}}} \left(\frac{\gamma^{\mathrm{F}}}{\gamma^{\mathrm{H}}}\right)^2 \tag{3.8}$$

which is obtained from Equations 3.2, 3.5 and 3.6. A potentially interesting feature of this measurement is the ability to obtain both of these constants from a single time domain trace. If the NSOR constant of H is assumed to be the same as pure water, which is a good approximation due to the relative proton concentration in the water/TFE mixture (containing 66.8 M of protons in water, and 11.3 M of proton in TFE with about 2/3 of the protons are not detectable), the fluorine NSOR constant can be calculated based on the relative NSOR constant ratio, which results in $\varphi^{\mathrm{F}}_{\mathrm{nsor}} = 4.15 \cdot 10^{-5}$rad M^{-1}cm^{-1}. This constant is about three times larger than the previously detected NSOR constant of F in C_6F_{14}, which was reported as $1.32 \cdot 10^{-5}$rad M^{-1}cm^{-1}.[1] It is possible considering that the proton NSOR constant can vary more than two times (water $9 \cdot 10^{-7}$rad M^{-1}cm^{-1}, cyclohexane $2.3 \cdot 10^{-6}$rad M^{-1}cm^{-1}). Further, it has previously been calculated that $-CF_3$ has a larger NSOR constant than $-CF_2$ in C_6F_{14} [12]. More than a half of the fluorine atoms in C_6F_{14} are $-CF_2$ while TFE has only a $-CF_3$ group. Additionally, the $\varphi^{\mathrm{F}}_{\mathrm{nsor}}/\varphi^{\mathrm{H}}_{\mathrm{nsor}}$ ratios were calculated by splitting the 18 batches of experiments into three consecutive groups, and the statistics show a variation of this ratio of 22%, mainly due to the SNR of the proton NSOR signal.

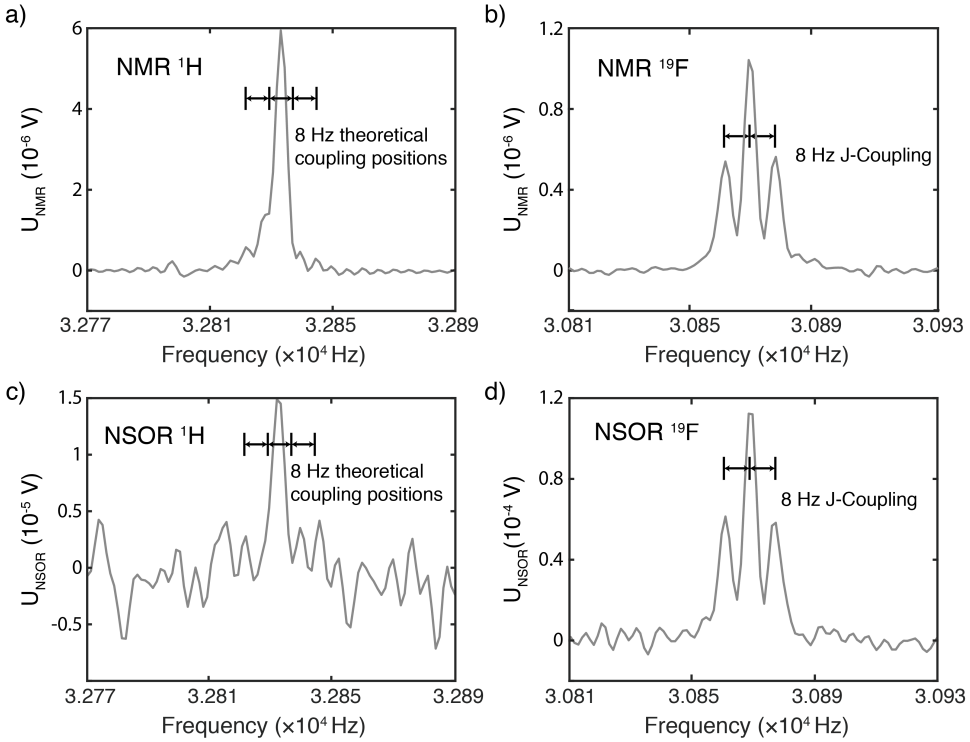

Figure 3.7: Expanded view of the peaks and designated coupling patterns. a) Proton NMR peak, b) Fluorine NMR peak, c) Proton NSOR peak, d) Fluorine NSOR peak.*

With the frequency dependent detection, and detection of two nuclei in the same spectrum, several features for the validation of signals become accessible. One possible artifact in the NSOR measurement is the Faraday rotation induced by radio-frequency pulses. The beginning 90 degree pulse is not eliminated by the phase cycling and thus there is indeed a large signal both in the NMR spectra and NSOR spectra. However, by cutting out this first pulse, the remaining NSOR spectrum shows no peak at the excitation frequency, which is in-between proton peak and fluorine peak. Since NSOR signals are weaker than the simultaneously detected NMR signals, another possible artifact would be due to instrumental crosstalk between the two channels. Although this can be ruled out

*Reprinted with permission from "Multinuclear Detection of Nuclear Spin Optical Rotation at Low Field" by Zhu, Y.; Gao, Y.; Rodocker, S.; Savukov, I. M.; Hilty, C., **2018**. *The Journal of Physical Chemistry Letters*, *9*, 3323-3327, Copyright 2018 by American Chemical Society [29]

by control experiments (Figure 3.5a, b), the different ratio of H/F signals in the NMR and NSOR spectra speak for the independent origin of the two signals. Here, the H/F signal ratio in the NSOR spectrum is about 50 times larger than in NMR spectrum than in the NSOR spectrum.

The NSOR constant depends on the hyperfine interaction and therefore on the properties of the electronic states coupled to the nucleus through Equation 3. Therefore, simultaneous measurements of multiple nuclei may enable the determination of properties of electronic states at multiple sites in the molecule, using the combination of optical detection with the localization to a nuclear spin resulting from the NSOR effect. Thereby, absolute values for NSOR constants can always be calculated by calibration with an internal standard consisting of a known substance. As shown here, internal calibration is especially useful when certain conditions are changing, such as the variation of effective light path length with flow rate.

Table 3.2: Calculation of NSOR constants.

	H	F
U_{NMR} (μV)	60.0	19.3
U_{NSOR} (mV)	0.131	2.17
$\Delta\theta$ (nrad)	1.41	23.0
γ (10^6 rad $\mathrm{s}^{-1}\mathrm{T}^{-1}$)	268	252
$\varphi^{\mathrm{F}}_{\mathrm{NSOR}}/\varphi^{\mathrm{H}}_{\mathrm{NSOR}}$	45.6	

Apart from resulting in chemical resolution through *J*-spectroscopy, an advantage of the CPMG based detection scheme compared to the application of a spin lock is that in the CPMG experiment, spins precess freely during the signal acquisition periods. The absence of an applied radio-frequency field eliminates the possibility for electrical cross-talk that could affect the detection of the small optical signals.

Further development of the experimental apparatus, including an improved laser arrangement with larger light path length,[13,32] and adjustments in circulation time, may in the future obviate the need for a superconducting magnet. The NSOR signal is indicative of the electron distribution around the atom. At low field, the *J*-coupling pattern along with the ability of detecting multiple nuclei at the same time could result in a means for identifying individual substances. Since the NSOR constants are typically higher in the larger molecules, such molecules could be observed selectively, in complement to the traditional NMR measurement. In this modality, NSOR could represent a low-cost alternative to traditional NMR for determining chemical identity.

3.4 Conclusion

In summary, we have demonstrated the ability to measure multinuclear, frequency resolved NSOR signals at low field. Using recirculating liquids in an optical cell containing NMR excitation and detection coils, we have determined the ratio between fluorine and proton NSOR constants in a mixture of DI water and trifluoroethanol. A CPMG based NMR pulse sequence maximized signal lifetime by refocusing spins dephased by magnetic field inhomogeneity, while at the same time retaining frequency resolution of pulsed NMR. High frequency resolution was further demonstrated in the observation of heteronuclear *J*-coupling multiplets. Since the NSOR constant depends on the hyperfine interaction, resolution of multiple nuclei potentially allows the characterization of electron configurations at multiple sites in a molecule, combining information on chemical and electronic structure.

4. DYNAMIC NUCLEAR POLARIZATION ENHANCED NUCLEAR SPIN OPTICAL ROTATION

4.1 Introduction

Observation of the nuclear spin optical rotation (NSOR) effect[18] and related magneto-optic nuclear-spin (MONS) phenomena inspire potential applications in a hybrid optical-NMR spectroscopy and magnetic resonance (MR) imaging. These effects would offer the possibility of probing excited electronic states with local nuclear markers, either by virtue of chemical shift, J-coupling, or multi-nuclear labeling.[26,29]

The NSOR effect is the only experimentally measured MONS phenomenon so far.[1,2,18,28] NSOR is basically the polarization plane change of a linearly polarized light caused by the photon-electron interaction, in which electronic states are perturbed by hyperfine interaction between short-ranged electron-nuclear pairs. Other MONS such as nuclear spin induced Cotton-Mouton effect (NSCM)[17,48,49,51–54] and nuclear spin circular dichroism (NSCD)[55,56] has also been theoretically estimated. NSCM holds promise to obtain signals directly dependent on the bond lengths and bond angles, but the signal was computed to be two orders smaller than NSOR. NSCD measures the ellipticity change, the other effect caused during the photon-electron interaction, but no experiment has been carried out to date. Although in specific situations, these effects can be comparable or larger than NSOR, they are much smaller in normal conditions.[50,56]

As the largest MONS, NSOR is proposed for the application as a combined NMR and optical spectroscopy. The NSOR constant φ is an indicator of how large the NSOR effect is. The frequency domain appearance of the NSOR signal relates to the chemical site by the same encoding as NMR, while NSOR constant measures the transition strength

of electrons from the ground state to excited state. A complete NSOR constant profile obtained by shifting the laser wavelength will help understand the electronic transitions at a specific nuclear site. The major difficulty for the measurement of NSOR or other MONS remains a low SNR. The NSOR constant can be calculated from the rotation angle $\Delta\theta$ for magnetization distribution $M(l)$ in the sample along the beam path:

$$\Delta\theta = \varphi \int M(l) dl \tag{4.1}$$

where φ is the NSOR constant. In the first NSOR measurement, water flowed through a 9 T superconducting magnet for prepolarization, and the light went through a 50-cm-long flow cell and obtained an SNR of 4.5 with 1000 s averaging.[18] Various methods were explored to improve the NSOR signal. These include a multi-pass strategy[1,28] to elongate the optical path length; optical detection inside a high field NMR spectrometer[26,27] , as well as hyperpolarization of nuclear spins,[18,97] to enhance the magnetization of the sample; measurements at a short wavelength,[1,28] which increases the NSOR constant. The experiments stopped using wavelengths below visible light region due to technical difficulties, but theoretical work predicted that by further decreasing the optical wavelength to near an absorption resonance, mostly in the vacuum ultra-violet (VUV) part of the spectrum, the NSOR signal could be enhanced by orders of magnitude.[43] Unfortunately, the resonance enhancement comes at a price of strong optical absorption, limiting the SNR enhancement obtained in this way. The NSOR signal is proportional to nuclear spin polarization, defined for spin–1/2 as the relative population difference of spin-up and spin-down states. Hyperpolarization methods can significantly increase the NSOR signal. The polarization level of nuclei is increased from typical values of $\sim 10^{-5}$ in superconducting magnets to $\sim 10^{-1}$ or more when using hyperpolarization, translating into a signal gain of several orders of magnitude. Nuclear

spin hyperpolarization can be produced by various techniques.[36–40] Savukov *et al.* made use of 129Xe spins hyperpolarized by spin exchange optical pumping to demonstrate measurement of the NSOR effect at low field.[18] Petr et al. took advantage of signal amplification by reversible exchange (SABRE) to measure the NSOR signal in pyridine and pyrazine under continuous flow conditions.[97]

Here, we demonstrate single scan NSOR measurements enabled through dissolution dynamic nuclear polarization (D-DNP). DNP is a quite universal method for the signal enhancement of most molecules and NMR active nuclei. DNP can be achieved in the frozen solid, making use of the hyperfine interaction between nuclear spins and electron spins of free radicals saturated by microwave radiation. In D-DNP, the sample is subsequently dissolved to result in a liquid containing highly spin-polarized solutes. With DNP achieving nuclear spin polarization at percent levels, the NSOR signal can be increased by orders of magnitude compared to that from thermal polarization. Besides, D-DNP also would solve the strong absorption problem for near resonance NSOR because a small quantity of absorbing molecules will be diluted in much less absorbing solvent.

4.2 Method

4.2.1 General experiment description

A tetra-coil produced the main magnetic field B_0 in the direction perpendicular to the plane of the figure.[94] A receiver coil was wound on the cylindrical portion of the sample cell for NMR detection. A pair of Helmholtz coils perpendicular to B_0 and the receiver coil was used for NMR excitation pulses. A 405 nm laser beam, redirected by a mirror, was sent through the sample cell to the polarizing beam splitter to analyze polarization. Lenses were used to focus the two beams after the beam splitter into the photodiodes. A half-wave plate was placed in front of the sample cell for adjusting the polarization plane,

so that the light intensity splits evenly.

A fast sample injection pneumatic module was implemented.[63] Briefly, the hyperpolarized sample was first loaded into a 5.6 mL loop. An optical sensor at the end of the sample loop triggered the switch of the injection valve when the sample loop was fully loaded. Subsequently, a syringe pump pushed the sample to the sample cell through a bubble trap, with a 400 mL/min stream of deuterated water. The injection valve switched back after a predetermined time to seal most of the sample inside the sample cell. The detection of NMR and NSOR signals started as soon as the valve switched back, after a total injection time of 0.7s.

Samples for ^{19}F were prepared by dissolving 45 mM 4-Hydroxy-TEMPO (TEMPO) in the pure trifluoroethanol (TFE). Samples for ^{1}H were prepared with 15 mM TEMPOL in dimethyl sulfoxide (DMSO) and heavy water mixture of a 4:1 volumetric ratio. 50 μL of samples were inserted into the DNP. Once samples had been polarized, heated pressured water was injected to dissolve the sample and push them into a sample loop. After that, a syringe pump sent the samples further into the sample cell for detection.

For the TFE sample, the NMR signal was detected in a static magnetic field of 0.7790 mT using a Carr-Purcell-Meiboom-Gill (CPMG) pulse sequence $p90\ [\text{-}\tau\text{-}p180\text{-}\tau]_{\times n}$ at the frequency of 31,200 Hz, where the pulse repetition time τ was 0.01 s. For DMSO sample, the field was adjusted to 0.7328 mT for the same frequency detection. The duration of the $\pi/2$ pulse was 0.48 ms and the duration of the π pulse was 0.96 ms. Data acquisition occurred continuously during the entire pulse sequence for 4 seconds at an acquisition rate of 499,200 Hz. Because of the continuous nature of the acquisition, the pulses are also collected. The pulses are removed before further analysis.

Polarization levels are calculated according to the following equation:[63]

$$P_{\text{DNP}} = \frac{U_{\text{observed}}}{2\pi^2 f n \mu_0 \mu_{\text{I}} w a_{\text{c}}^2} \tag{4.2}$$

where f is the NMR frequency adjusted to 31200 Hz to fit in the analog filter pass band we used; $\mu_0 = 4\pi \cdot 10^7$ H·m^{-1} is vacuum permeability; $w = 220$ is the number of receiver coil turns; $a_{\text{c}} = 4.5$ mm is the radius of the sample cell; n is nuclear spin number density; and μ_{I} is the magnetic moment of the nuclear spins.

Rotation angles are calculated using the following equations:[29]

$$\Delta\theta = \frac{U_{\text{diff}}}{4 \cdot U_{\text{1ch}} \cdot g_{\text{n}}} \tag{4.3}$$

$$\varphi = \frac{\Delta\theta}{l \cdot [C] \cdot P} \tag{4.4}$$

where $\Delta\theta$ is the NSOR angle, U_{1ch} is one channel photo-diode output voltage, $l = 3.41$ cm is the laser path length, and $[C]$ is the molar concentration of the nuclei in the liquid.

SNR is obtained by comparing the maximum signal height and the standard deviation of an adjacent noise region of the real spectrum.

4.2.2 Detailed detection part setup

The cross section view of the NMR detection and NSOR detection is shown in Figure 4.1.

The injector (Figrue 4.2) works by switching between two modes, 'inject' mode and 'load' mode. Initially, the injector stays in 'load' mode while waiting for the input of the sample. The hyperpolarized sample enters the injector from ① and fills the sample loop ②. A liquid detector at the end of the sample loop triggers the mode switch to

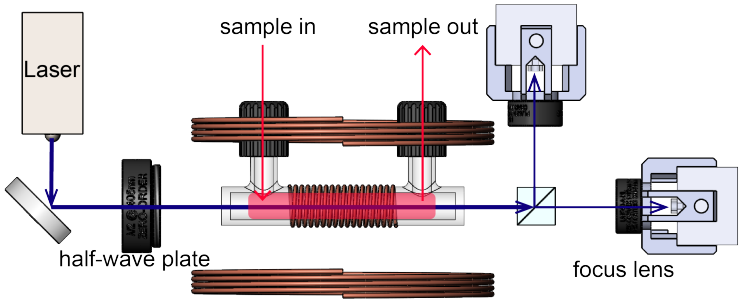

Figure 4.1: The setup of the NSOR experiments. The sample path is marked in red. Hyperpolarized liquid was injected into the sample cell and formed a mixture with the original water inside the cell. The laser beam path is marked in blue. The polarization plane of the beam rotated by the sample was detected by the balanced polarimeter, consisting of a polarizing beam splitter and two photodiodes.

'inject' when the sample loop is fully filled. A syringe pump ③ pushes then sample with a 400 mL/min stream of D_2O through a bubble trap ⑦ into the sample cell ⑥. After a predetermined time by injection tests, the injector switches mode back to 'load' and the NMR and NSOR signals are then measured from the sample.

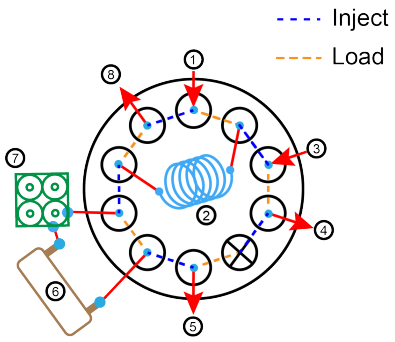

Figure 4.2: The diagram of the sample injector used in the D-DNP process. Red arrows represent the flow direction of the liquid. Dashed blue/orange lines indicate the connection of two adjacent ports in the inject/load mode. ①: DNP samples, ②: sample loop, ③: syringe pump, ④, ⑤, ⑧: waste, ⑥: sample cell, ⑦: bubble trap (c) Comparison of laser intensity during DNP injection of water for three different cases.

4.2.3 Laser stablization and fluid handling

One major challenge in DNP-NSOR experiments was the unstable laser beam path inside the sample cell, which led to reduction in light beam intensity and increase in optical noise. The small reception area of the photodiode (2.2 mm by 2.2 mm) combined with a long distance from the sample cell (50 cm) made the optical signal intensity extremely sensitive to the laser beam path perturbations inside the sample cell. The path perturbations were caused by two different factors. First, the gas bubbles formed during dissolution process inside DNP polarizer and scattered the beam. These gas bubbles were removed with a bubble trap that operated at a flow rate of 400 mL/min. A high flow rate was desired to reduce the relaxation losses of nuclear polarization during injection. A custom designed trap (Figure 4.3) containing four PTFE membranes in serial configuration were placed in-line with the sample stream. The second reason for the unstable laser beam path is the refractive index fluctuations along the laser beam due to turbulent mixing of the DNP sample and water. A different composition and temperature of the injected sample affected the refractive index, causing deflection of the laser beam. This issue was addressed by placing a plano-convex lens in front of each photodiode and focusing the beams to the centers of the photodiodes' detection regions. This way, the effective light reception area was made as large as the lens size. After these modifications, the detected laser beam became stable enough for reliable NSOR experiments. Figure 4.4 shows the optical intensity fluctuations for three cases: when pure water was injected and no modifications were made (top), when only the bubble trap was installed (middle), and when both the bubble trap and focusing lenses were installed (bottom).

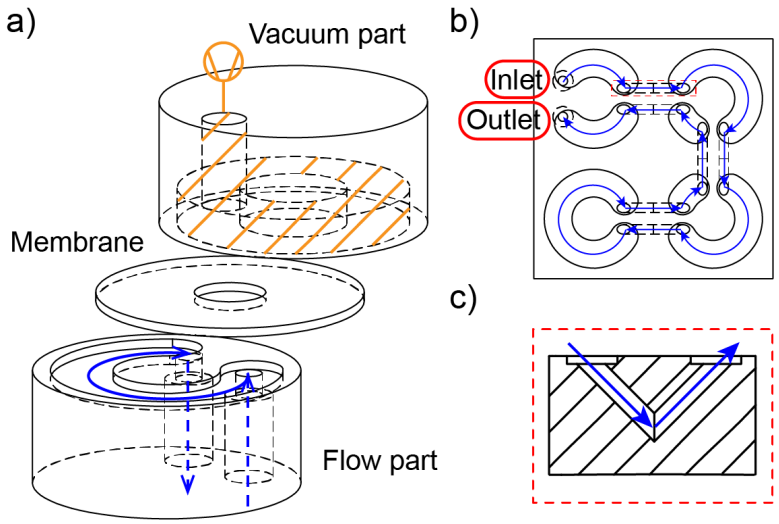

Figure 4.3: a) The general view of a one membrane bubble trap. It is composed of three parts, a vacuum part, a membrane and a flow part. The PTFE membrane's bore size is about 10 μm and allows the gas to go through but not liquid. The flow part allows the liquid to get broad contact with the membrane. The vacuum part is a vacuum chamber and encourages the gas bubble to go across the membrane. Blue lines represent liquid path and yellow lines represent vacuum. b) The design of the four-membrane bubble trap. The inlet and outlet are on the top left corner and the liquid travels through all four membranes before leaving the bubble trap. The channel between the membranes are shown in c).

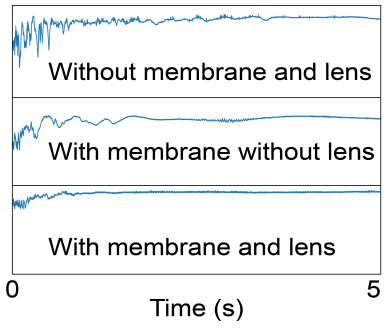

Figure 4.4: Comparison of laser intensity during DNP injection of water for three different cases.

4.2.4 Flow simulation

In ref,[29] a constant flow rate affected the light path length linearly, possibly due to differences in sample polarization distribution inside the cell at different flow rates. In the current experiment, turbulent mixing of sample caused differences in sample distribution at the time of detection. By comparing the NSOR signal of TFE obtained in the current experiment with that in the literature,[29] the effective path length was calculated to be l = 3.43 cm. Estimation of the light path length was also done by doing flow simulation using SolidWorks. As can be seen in Figure 4.5, the simulation of injected water was run at a flow rate of 200 mL/min, which is an average value between the full injection rate of 400 mL/min and stopped flow of 0 mL/min. The laser path was simulated at the center of the sample cell and the number of particles going through the center 1.5 mm diameter was collected for further computation. The length of the sample cell was divided into 300 segments and the percentage of particles in the laser path in each segment was shown in the lower graph. The average percentage of particles going through the laser path is p_1 = 1.27 %. If the flow is completely uniform, the percentage will be just the ratio of the cross-section area of the laser and the area of the sample cell, which is p_2 = 2.78. Therefore, the average laser path length should be $p_1/p_2 \times l_{\text{cell}}$ = 3.38 mm %. Since the simulation is under a constant flow condition instead of a injection-stop flow, the path length from TFE calculation was used to calculate NSOR constant of DMSO.

4.2.5 Verdet constant determination

Verdet constant determination was carried out with pure samples of water, TFE and DMSO. The setup is the same as NSOR but the receiver coil was connected to a function generator for producing the magnetic field along the laser beam. The function generator's output was a sine wave with voltage kept at 4 V_{pp}, 31.2 kHz. The background noise was

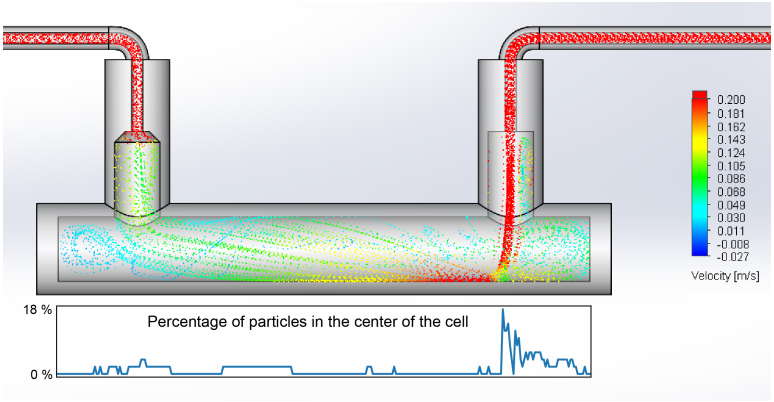

Figure 4.5: The water flow simulation with SolidWorks at a flow rate of 200 mL/min. The lower part of the figure indicates the percentage of simulated liquid particles intersecting with the laser path. (a cylinder in the center of the sample cell of 1.5 mm diameter)

Table 4.1: Verdet constant (V) calculation. * data is taken from ref. [1]

Sample	U_0 (V)	ΔU (μV)	angle (μrad)	V (μrad M^{-1} cm^{-1})
water	3.3	73	5.5	0.94*
DMSO	2.9	105	9.1	1.57
TFE	3.3	30	2.3	0.36
blank	3.1	3.1	0.25	N/A

calculated by measuring the Faraday Rotation with no sample inside the cell. Table 4.1 shows the results.

4.2.6 Discussion about SNR caused by shot noise

As shown in,[2] SNR $\propto l \cdot 10^{-A_0 l/2}$, where A_0 is the loss of laser intensity in a unit length and l is the path length. Taking the derivative of $l \cdot 10^{-A_0 l/2}$ we got $(10^{-A_0 l/2} - (\ln 10)/2 \cdot A_0 \cdot l \cdot 10^{-A_0 l/2})$. Equaling this to 0, we get $A_0 \cdot l = 2/\ln(10)$, which means the SNR reaches maximum when the laser loses about 86.8% of intensity due to absorption. Here we assumed photon shot noise limit when angle measurement accuracy scales as the square root of the number of photons and the NSOR angle is proportional to the path

length, while the intensity difference output is exponentially attenuated. Such increase in SNR can be interfered by electronic noise of the photo-diode amplifier, cross talk due to electrical coupling with other simultaneously acquired data and mechanical vibrations from environment.

4.2.7 Product Operator Demonstration of *J*-coupling Evolution

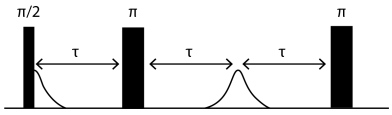

Figure 4.6: CPMG pulse illustration

$$
\begin{aligned}
I_z &\xrightarrow{(90^\circ_x)_I} -I_y \\
&\xrightarrow{\Omega_I\tau} -I_y\cos\Omega_I\tau + I_x\sin\Omega_I\tau \\
&\xrightarrow{\pi J_{IS}\tau} -I_y\cos\Omega_I\tau\cos\pi J_{IS}\tau + 2I_xS_z\cos\Omega_I\tau\sin\pi J_{IS}\tau \\
&\qquad + I_x\sin\Omega_I\tau\cos\pi J_{IS}\tau + 2I_yS_z\sin\Omega_I\tau\sin\pi J_{IS}\tau \\
&\xrightarrow{(180^\circ_y)_I} -I_y\cos\Omega_I\tau\cos\pi J_{IS}\tau - 2I_xS_z\cos\Omega_I\tau\sin\pi J_{IS}\tau \\
&\qquad - I_x\sin\Omega_I\tau\cos\pi J_{IS}\tau + 2I_yS_z\sin\Omega_I\tau\sin\pi J_{IS}\tau \\
&\xrightarrow{\Omega_1\tau} -I_y\cos\pi J_{IS}\tau - 2I_xS_z\sin\pi J_{IS}\tau \\
&\xrightarrow{\pi J_{IS}\tau} -I_y
\end{aligned}
$$

Product operator shows that the J-coupling will be refocused after a π pulse. I_n, S_n, $n = x, y, z$ is the magnetic moment of nucleus I, S in direction x, y, z. Ω_I is the Larmor

frequency of I. J_{IS} is the coupling frequency between nucleus I and nucleus S. τ is the time illustrated in Figure 4.6.

4.2.8 Assembly of a 1 T Magnet for NMR Calibration

Since the instrument needs to be adjusted in terms of nuclear frequency and shimming, a constant NMR signal is desired. The low field instrument itself has little polarization and NMR signal need to be averaged for long time to be visible. DNP hyperpolarizes the sample but the polarization level will drop at an exponential rate and lasts for only a few times of relaxation time of the molecule, usually a few seconds. A 1 T permanent magnet was constructed and used for calibration purpose. Figure 4.7 shows the general construction of the magnet. The N52 neodymium rare earth magnets (CMS Magnetics, TX) are blocks of 2" $\times$ 1" $\times$ 1" and the field is along the short side as displayed in arrows. This pseudo-Hallbach magnet design was attributed to ref.[98] Since the difficulty of assembling such a magnet increases linearly with the number of elements but the effective produced field only increases logarithmically, an element number of eight was chosen for our purpose.

Since each magnet has a strong field, they tend to align themselves in the same direction and a strong torsion was encountered during the assembly process. A safety jig was 3D printed for assembly assistance. A specific order of adding magnet was shown in Figure 4.8. Before adding any new magnet, the space inside the magnet box was filled with aluminum bars with the same dimensions. Each magnet was added step by step by replacing the aluminum bar with the help of the safety jig as illustrated as in Figure 4.9. The resulted magnet has its magnetic field mostly concentrated in the center where the liquid sample flow through. The inner magnetic field was tested to be about 1 T and is suitable for the purpose of prepolarization.

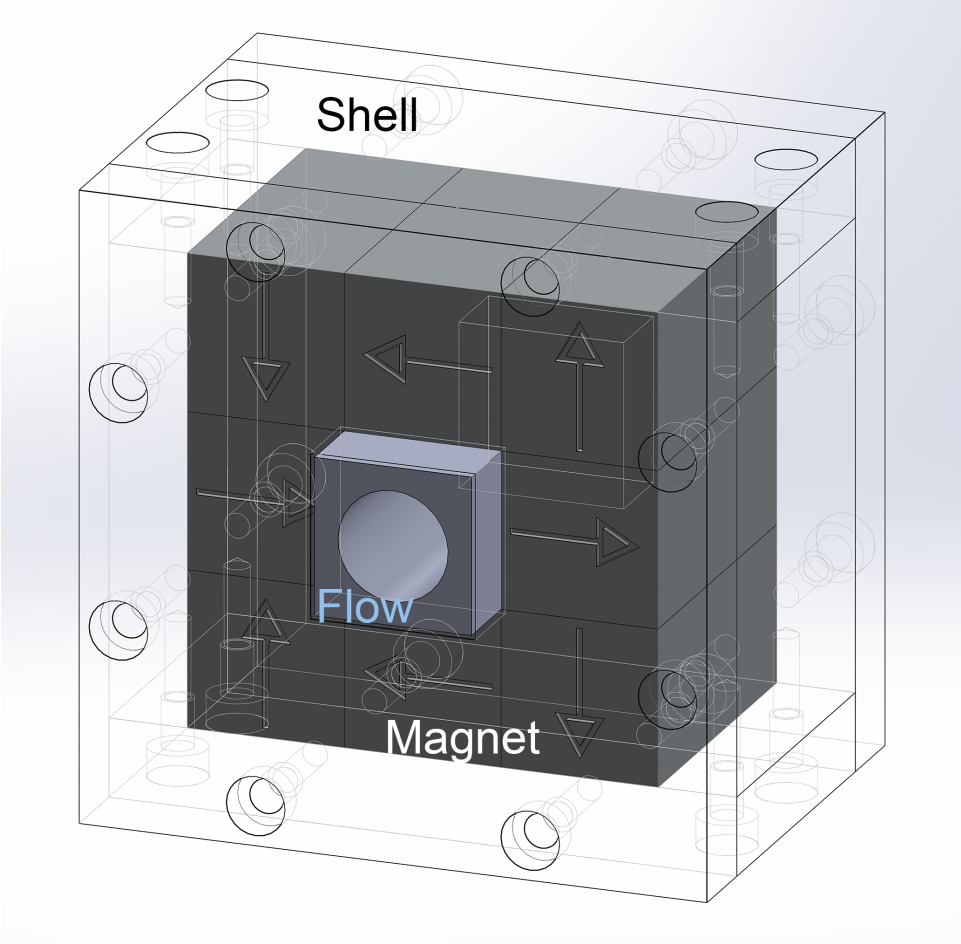

Figure 4.7: Whole view of the permanent magnet. The transparent part is the shell, the dark grey part are magnet elements and the center light grey hole was for flow of samples. The holes on the shell are spot for screws. The arrow mark on each magnet element represent their own direction of magnetic field.

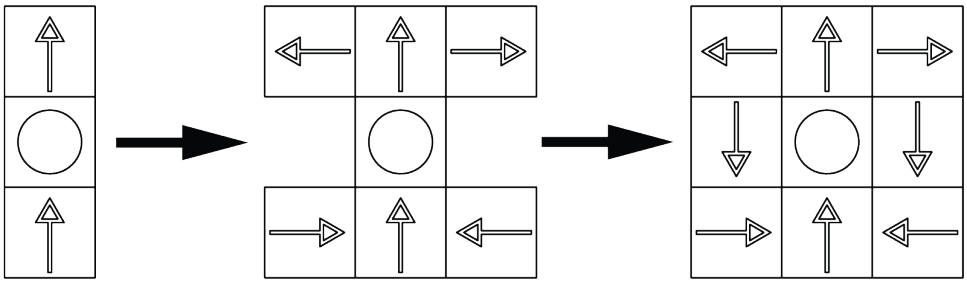

Figure 4.8: This order of adding magnets was determined to reduce the torque when placing a new magnet element.

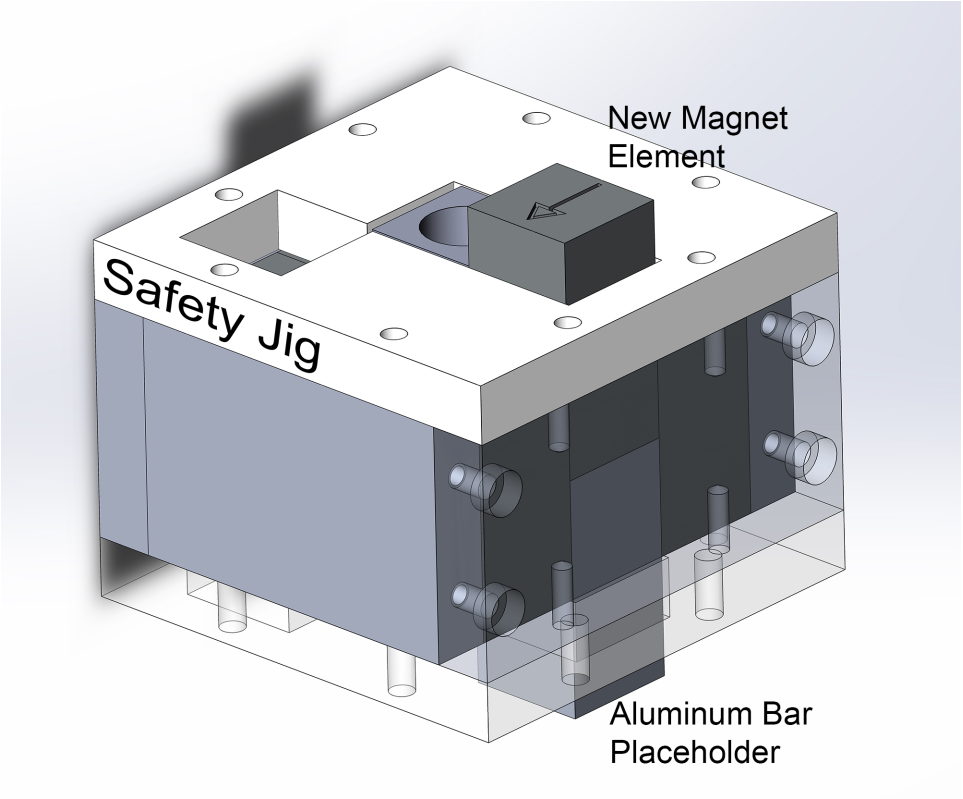

Figure 4.9: Demonstration of adding a new magnet element with the help of the safety jig.

4.3 Results and Discussion

DNP enhanced NSOR signals were acquired in a low-field NMR instrument (Figure 4.10). Unlike previous experiments, where signals were extensively averaged in stationary samples or under constant flow, D-DNP enabled the measurement of NSOR signals in single scans. The turbulent injection of diluted DNP hyperpolarized compounds presented challenges in the required delicate optical alignment. After stabilization of the laser beam by optical and fluid handling techniques, significant improvement was achieved, and a detectable signal was produced at the NMR frequency.

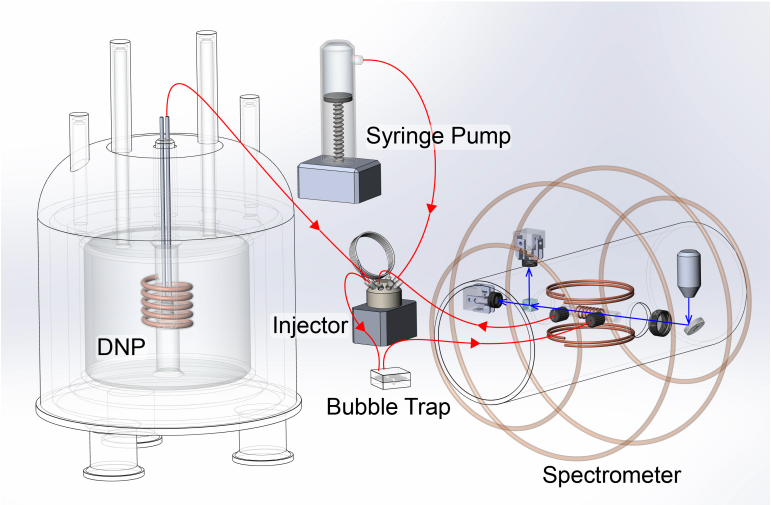

Figure 4.10: Setup of the D-DNP NSOR experiments. The hyperpolarized sample was sent into an injector, which was later pushed into the sample cell by a syringe pump and formed a mixture with the original liquid inside the cell. A bubble trap was installed inline to remove the gas bubble formed during the injection. The laser beam path is marked in blue. The polarization plane of the beam rotated by the sample was detected by the balanced polarimeter, consisting of a polarizing beam splitter and two photodiodes.

A DNP-NSOR spectrum of ^{19}F in 2,2,2-trifluoroethanol (TFE) (120-fold dilution in D_2O on average) is shown in Figure 4.11a. The signal-to-noise ratio (SNR) of the diluted sample is 6.1, which is about 33 times higher per scan than prepolarized 1:1 TFE water

mixture with a superconducting magnet, meaning it would take around 1100 scans for prepolarization experiment to achieve the same signal level.[29]

The NMR signal of ^{19}F is simultaneously acquired (Figure 4.11b) in order to obtain the magnetization level. The ^{19}F NMR and NSOR signals of TFE would feature a triplet due to the fluorine-proton *J*-coupling of 8 Hz.[29] However, for signal acquisition, a Carr-Purcell-Meiboom-Gill (CPMG) pulse sequence covering only the fluorine frequency was chosen. With a repetition rate of refocusing pulses that is larger than the *J*-coupling, the coupling is refocused, and the triplet signal is collapsed into a single peak. The signal intensity is thereby increased by a factor of two.

In order to exclude the possibility of unintentional signal in NSOR from NMR, two sets of control experiments were carried out, and the results are shown in the middle tab and bottom tab of Figure 4.11. In one control experiment (middle), the laser was turned off while samples were hyperpolarized using DNP to exclude the possibility of electrical coupling between NMR and NSOR channels. In the other control experiment (bottom), the laser was on, but the sample was not prepared with prepolarization. This one excluded the possibility of induced optical rotation by the NMR excitation pulse.

While ^{19}F is typically exhibiting a large NSOR constant because of a high electron density, D-DNP is broadly applicable to spin-1/2, and even some other nuclei. The DNP assisted detection of NSOR for ^{1}H of hyperpolarized dimethyl sulfoxide (DMSO) is demonstrated in Figure 4.11c while the simultaneous NMR detection in Figure 4.11d. Here, DMSO was hyperpolarized and diluted with D_2O to ~ 0.09 M during dissolution and injection into the measurement cell. As above, NSOR and NMR signals were shown side by side in the figure. The external magnetic field was adjusted for DMSO so that the precession frequency remains at 31200 Hz to fit in the narrow band-pass filter range.

Comparing Figure 4.11b and d, we can see the NMR signal of DMSO is about

two times larger than TFE. As shown in Equation 4.1, the rotation angle of the laser is proportional to the magnetization level of the sample. Although with a lower magnetization level, the NSOR voltage in TFE is about four times that of DMSO. One reason for this is the greater NSOR constant φ of TFE. Another contribution stems from the different laser intensities in two experiments. The same initial laser power was applied to both samples, but the difference in absorption caused a difference in the detected laser intensities. Rotation angles are calculated as $\Delta\theta = U_{\text{diff}}/4U_{\text{int}}$. For the same rotation angle $\Delta\theta$, if the detected laser intensity U_{int} drops down, the acquired signal U_{diff} becomes less as well.

The SNR of the NSOR signal in DMSO is 3.7, which is about two thirds of TFE. As discussed above, this was caused by a few factors combined, including the magnetization level, NSOR constant, and laser intensity. The control experiment results are similar to that of TFE, confirming the NSOR signal is not cross talks from other sources.

Apart from the confirmation of signal origination, the noise levels in control experiments also served to understand noises from the laser beam. The laser-off control experiment (middle) shows the dark current noise from the photodiodes is at a similar level. In TFE, the noise level in signal (top) is about three times larger than the dark current noise (middle), while DMSO is 1.5 times larger. The difference comes from the laser intensities. A stronger detected laser intensity in TFE experiment caused the higher shot noise level. Bottom tab shows the stationary sample noise level, which is greater than the top tab also due to laser intensity difference. The laser lost intensity during turbulent sample mixing. The bottom tab noises are just slightly greater than in top tabs, indicating the loss due to sample mixing is not significant compared to optical absorption.

For quantitative analysis, real spectra from multiple samples were averaged (Figure 4.12). In these spectra, the SNR for TFE and DMSO was determined to be 9.1 and

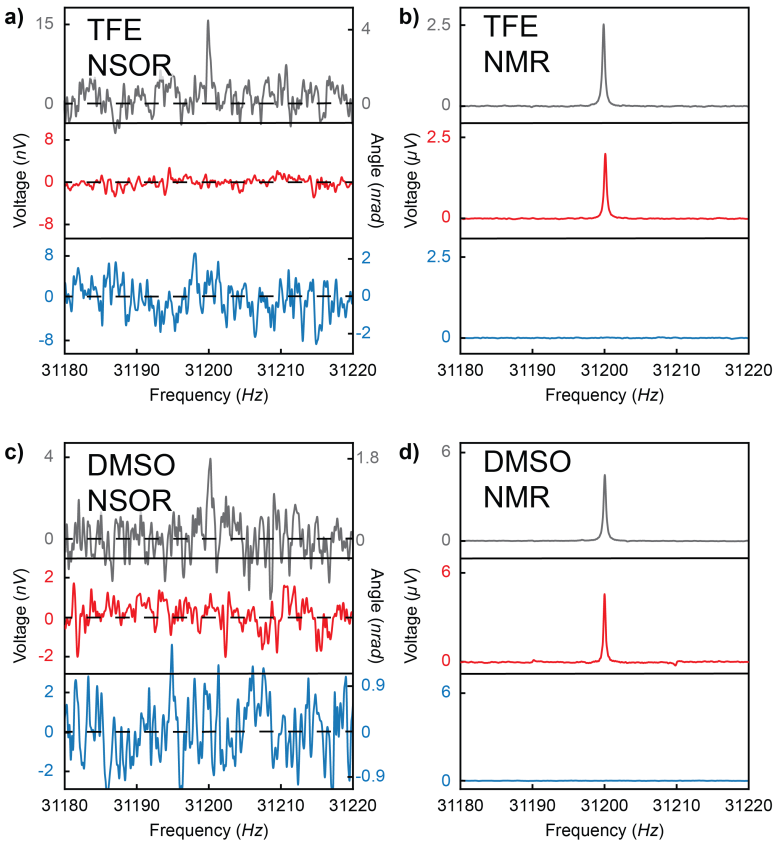

Figure 4.11: (a) The acquired TFE NSOR real spectrum acquired with a CPMG pulse sequence in the D-DNP experiment (top) and noise spectra in two control experiments (middle: laser off, hyperpolarized sample; bottom: laser on, stationary non-hyperpolarized sample). The rotation angle for laser off experiment is not calculated due to the lack of laser intensity. (b) Simultaneously acquired corresponding NMR spectra in the D-DNP experiment (gray) and the two control experiments (red and blue, the same as above). (c) Acquired DMSO NSOR signal and (d) Simultaneously acquired corresponding NMR signal in the D-DNP experiment.

6.3, respectively. The SNR scales a little less than the theoretical square root of the average number because of the varied dilution factors and laser intensities in individual experiments. The dilution factors affected the consistency in polarization levels while the laser intensity affected the rotation angle. An averaged polarization level and laser intensity are used in averaged calculations due to the linear relationship between the two parameters. The data is analyzed in Table 4.2 to calibrate the laser path length from TFE and calculate the NSOR constant for DMSO. The upper part of the table is a calculation of

the nuclear spin polarization levels P_{DNP} from the NMR signals. The lower part shows the calculated NSOR rotation constant of DMSO, which were are based on the difference voltages from photodiodes U_{diff} (see Methods). Based on equation 4.4, and knowing the NSOR constant (41.2 μrad M^{-1} cm^{-1}) from ref,[29] the effective light path length was calculated to be 3.43 ± 0.38 cm. A flow simulation (see supporting information) carried out supported the path length value calculated above. The effective laser path length is only about half of the total length of the sample cell because turbulent mixing of the sample caused sample distribution variations at the time of detection.

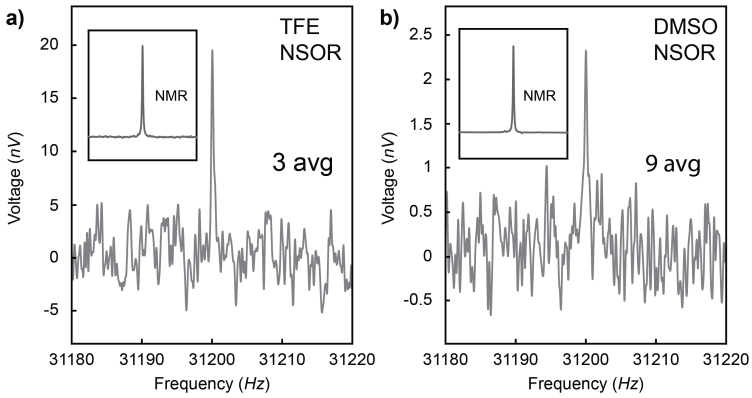

Figure 4.12: (a) TFE NMR signal of three D-DNP experiments averaged by adding the phased real spectra. (b) DMSO NMR signal of nine D-DNP experiments averages. The inset shows the corresponding NMR signal in both figures.

NSOR constant of DMSO is calculated to be 4.1 ± 0.7 μrad M^{-1} cm^{-1}, assuming that the laser path length is the same as in TFE experiments.Unreported before, this is the largest NSOR constant observed in protons so far. For comparison, the smallest NSOR constant is from water, 0.94μrad M^{-1} cm^{-1}, and largest from cyclohexane, 2.29μrad M^{-1} cm^{-1}.[1] Such an increase in the value of the NSOR constant of DMSO can be attributed to two factors. One is the methyl group has a larger hyperfine interaction than water. In

Table 4.2: Upper: NMR polarization levels P of fluorine in TFE and proton in DMSO; lower: calculated NSOR constant of proton in DMSO. U_{observed} is the detected voltage from the pickup coil; n is nuclear spin number density; μ_I is the magnetic moment of the nuclear spins. NMR calculation is based on Equation 4.2, and NSOR calculation is based on Equation 4.4

Nuclear Magnetic Resonance calculation				
compound	U_{observed} (V)	$n(\text{m}^{-3})$	$\mu_{\text{I}}(\text{J}\cdot\text{T}^{-1})$	P
TFE	$8.08\cdot10^{-5}$	$2.39\cdot10^{28}$	$1.33\cdot10^{-26}$	$7.38\cdot10^{-5}$
DMSO	$2.18\cdot10^{-4}$	$5.09\cdot10^{28}$	$1.41\cdot10^{-26}$	$8.79\cdot10^{-5}$

NSOR constant calculation of proton in DMSO			
U_{diff} (V)	U_{int} (V)	l (cm)	φ_{NSOR} (rad M^{-1} cm^{-1})
$2.2\cdot10^{-7}$	0.54	3.43	$4.0\cdot10^{-6}$

a molecule with most protons in the methyl group, the NSOR constant is about two times larger than that of water, as can be seen for ethanol, propranolol, isopropanol, hexane, and cyclohexane in ref.[1] On the other hand, the NSOR constant partially depends on the Faraday effect. The Verdet constant is calculated for the Faraday effect as in Equation 4.4, but by replacing the nuclear spin magnetization with the externally applied magnetic field. In DMSO, the Verdet constant was determined to be 2.03 μrad M^{-1} cm^{-1}, about two times larger than in water, where it is 0.94 μrad M^{-1} cm^{-1}. The increase of the Verdet constant and corresponding NSOR constant can be attributed to lower electronic excitation frequency ω_k, as can be seen in the formula below.[18]

$$\varphi \propto \frac{\omega^2}{(\omega_k^2 - \omega^2)^2}$$

ω is the incident laser frequency. In DMSO, the S-C bond is responsible for the longer excitation wavelength at 236 nm due to the larger electron cloud of sulfur.[99,100] This formula can be used to qualitatively estimate the NSOR constant within the same nucleus since the hyperfine interaction is not that different. For example, water has an absorption of 166.5 nm. The frequency-dependent coefficient ratio of DMSO to water is 3.2, while

the NSOR constant ratio is 4.4. This wavelength dependence can be taken advantage of to enhance the NSOR signal by using VUV light sources. Enhanced NSOR experiments would be possible with 90-340 nm light sources from the optical systems containing two cascading second-harmonic generation stages and a semiconductor amplifier.

The NSOR effect measures only the nuclear spin magnetization along the light propagation path, which could be taken advantage of to construct a 2-dimensional (2D) projection image of the injected liquid by scanning the laser path across the sample. In such a 2D image, the nuclear spins are interrogated passively without the perturbation from the gradient field, which would enable the measurement of long-range dipolar interactions.[19,20] Unlike short-range dipolar interactions, long-range dipolar interactions are not averaged out by diffusion. Effects from such interactions have been used in MR imaging contrast enhancement[101,102] and studying the dynamics of cold gases.[103,104] A 3D image is possible if one gradient is applied along the light beam. Here the D-DNP brings the advantage that a short path length is sufficient, and no multi-pass is needed. To further increase SNR in imaging applications, an array of long and thin cylindrical crystals with a high Verdet constant may be inserted into the imaging area, so optical SNR will be high enough for fast single-scan 3D imaging. This can be used in dynamic applications where for example, a chemical reaction occurs during the mixing, and 3D imaging is needed.

Our results demonstrated the possibility of using the DNP to enhance the nuclear spin polarization of samples, which increased the SNR of NSOR signal by more than 30 times in a 100 fold diluted sample compared to signal acquired in pure liquid prepolarized in a 9.4 T magnet. NSOR signals can potentially be acquired with any compound that is compatible with dissolution DNP. In contrast, traditional NSOR experiments are dependent on a spin density only available in pure liquids. This feature significantly broadens the application range of NSOR spectroscopy. NSOR signal may further be

acquired of low-frequency nuclei commonly encountered in chemistry or biochemistry, such as ^{13}C, ^{15}N, ^{29}Si, ^{31}P, and numerous inorganic elements with spin-1/2. The lower magnetization produced by these nuclear spins can be alleviated by hyperpolarization. Larger elements exhibit an enhanced NSOR effect,[18] which can further facilitate the application of DNP-NSOR spectroscopy in these cases.

Further optimization of D-DNP could lead to additional increases in SNR. For example, the sample cell's geometry can be optimized in a few different ways. A cell with a smaller in diameter would allow for an increase in sample concentration, in turn increasing the SNR proportionally. The turbulent mixing of injected liquid with the stationary liquid in the sample cell has caused a shorter effective laser path length, which is about half of the actual length that the laser travels. By optimizing the flow dynamics, the SNR could potentially be increased by up to two times.

A potential advantage of DNP is the shorter laser path length or lower sample concentration needed when the laser wavelength is near the electronic transition wavelength of the molecule. In this case, the NSOR signal will be highly enhanced, but restrictions introduced by absorption will render the static multi-pass configuration method[105] inapplicable for improvement of SNR. This limitation arises because the SNR reaches a maximum when the laser loses about 86% intensity due to absorption. With the DNP-NSOR experiment, this problem is alleviated because a smaller amount of highly polarized sample does not cause strong absorption of the laser light. The specific example of DMSO described in this paper is a case in point. DMSO exhibits a strong absorption coefficient (0.21 M cm^{-1}) near 240 nm.[100] The absorbance maximum of DMSO is at a longer wavelength than, for example, the substances considered in[43] and will be soon within reach of inexpensive semiconductor lasers or may already be within reach of light-emitting diode (LED) sources. Since DNP can be used to enhance the polarization

level in a wide range of substances, it is a general method to increase the NSOR signal, especially when the laser wavelength is close to the excitation frequency of the molecule. By scanning around the excitation frequencies, a complete profile can be obtained. In a large molecule, such an excitation profile helps to understand the electron transitions around a certain nucleus labeled by NMR frequency.

4.4 Conclusion

In summary, we have demonstrated the NSOR signal observed in a single scan. An increase in SNR by orders of magnitude was owing to the increase in nuclear spin polarization, up to the percentage level, by using D-DNP. With the increased SNR and lowered detection limits, the NSOR effect can find broadened applications in MR imaging and optical-NMR hybrid spectroscopy. By reducing the negative effects of absorption, even higher enhancement would be possible at a laser wavelength close to an electronic transition wavelength of the molecule. In MR imaging, the use of three gradient fields can be reduced to one to implement fast simultaneous 3D imaging. Non-perturbative 2D imaging can also be implemented to study distant dipolar field interactions without the influence of gradients. In the spectroscopy, molecular structural information in the excited states can be obtained from localized electronic excitations and nuclear-spin labeling. D-DNP can potentially expand the application range of NSOR based spectroscopy to include most small-molecule compounds and typical spin-1/2 nuclei.

5. CONCLUSION AND SUMMARY

Nuclear Spin Optical Rotation (NSOR) holds the potential of combining nuclear magnetic resonance (NMR) spectroscopy with optical spectroscopy. The NMR aspect reveals information on nuclear spins, while the optical spectroscopy reports information about electronic excitation. This combination gives a unique way to identify the electronic information at a specific nuclear site, which can probe the local electronic structure in a large molecule. However, the intrinsically low signal to noise ratio (SNR) has largely prevented NSOR applications. Various efforts, such as laser path length increase, laser wavelength change, and polarization with parahydrogen, have been made to increase the NSOR signal.

We increased the SNR of NSOR with the dissolution dynamic nuclear polarization (D-DNP) technique in this work. This technique increased the magnetization of the nuclear spins, which in turn linearly increased the NSOR signals. This technique does not have the limitations of other, optical related methods for increasing signal. For example, laser path length increase and wavelength change can increase the NSOR rotation angle, but at the same time increase the laser absorption. These two combined factors will ultimately limit the maximum possible SNR gain. Parahydrogen polarization has similar benefits of D-DNP and less expensive maintenance cost, but the polarization enhancement is about ten times less and only applies to limited nuclei. D-DNP has been demonstrated to increase proton and fluorine magnetization by a few thousand times, translating to the same amount of NSOR signal increase in our work.

To enable the NSOR measurements with hyperpolarization by D-DNP, several challenges related to instrumentation were overcome. First, the demand for adding

optical detection to an NMR required highly modifiable instrumentation. Second, NSOR detection needs a complex optical system to be added. Third, complications related to flow conditions during the dissolution needed to be overcome in the optical measurement.

In a high field NMR spectrometer, little space is available to add optical devices in the NMR probe. This is because of the nature of a small homogeneous field region in a high magnetic field. We opted for modifying a low field NMR instrument to accommodate the simultaneous NMR and optical measurement. To evaluate the D-DNP technique's effectiveness with the low field NMR instrument, we examined and optimized various parameters for obtaining the highest polarization level. We achieved a 5% polarization before dilution from water in the low field NMR instrument, which is about 1500 times higher than could be achieved in a 9.4 T superconducting magnet. We added an optical absorption measurement to the low field NMR system to monitor the sample flow during injection and determine the final dilution factor. We observed a decrease in laser intensity during injection, probably due to the gas bubbles and turbulent mixing of liquid. The dilution factor was determined to be about 120 on average based on the absorption of light in the mixed sample. With 1500 times increased magnetization, a single scan NSOR was theoretically possible, not considering the laser condition during the injection process.

Optics for an absorption measurement alone, as described above, is not sufficient for measuring the polarization plane change for NSOR signals. We therefore designed an optical system that split the laser beam to two halves for polarization plane rotation detection and made the beam reflect three times inside the sample for increased optical signals. To understand how the NSOR signal is affected by the liquid flow, we prepared continuous-flow NSOR measurements at different flow rates. The continuous-flow NSOR experiment is carried out by pre-polarizing samples from a superconducting magnet. Previous NSOR experiments in the low field utilized spinlock,

which increased the sensitivity but lost the spectroscopic information. By applying a Carr-Purcell-Meiboom-Gill (CPMG) pulse sequence covering both proton and fluorine frequency, we observed signals from both nuclei simultaneously. The acquisition of a J-coupling multiplet NSOR signal was also demonstrated in the low field for the first time. J-spectroscopy potentially allows structural characterization. Having both nuclear signals in the same spectrum allowed the internal calibration of the NSOR constant. We find NSOR constant of ^{19}F in trifluoroethanol is over 40 times larger than ^{1}H in water. The most important reason for such a high NSOR constant in ^{19}F is the high electron density, which increases the hyperfine interaction between the nucleus and electron. Apart from the demonstration of low field NSOR measurement, we learned that the flow rate could affect the magnetization distribution of the pre-polarized sample, which causes a dependence of effective light path length on the flow rate.

All NSOR experiments in the literature have involved stable liquid samples, either stationary or at a constant flow, probably for reasons of an easier averaging and delicate optical setup. Since D-DNP involves a rapid injection process, during which the sample condition is far from stable, the technical challenge of the D-DNP NSOR experiment is to find a way to get signals from samples under non-ideal conditions. During the DNP sample injection, gas bubbles are introduced, and liquids are partially turbulently mixed, resulting in a non-homogeneous sample solution. The partial mixing brings two issues. One is that different refractive indices between the mixture component can alter the laser path. The other involves the unknown distribution of sample magnetization. We mostly removed the gas bubbles with a custom-made four-PTFE-membrane bubble trap and corrected the altered laser path with a convex lens in front of the detector. We calculated the amount of sample is in the laser path by comparing the NSOR constant with a substance of known value. On these bases, we demonstrated the NSOR signals of fluorine and proton acquired

in a single scan for the first time in a sample diluted more than 100 fold. The NSOR constant of protons in dimethyl sulfoxide was determined using this technique. Unlike other NSOR experiments at the low field that required a reservoir of the sample, the D-DNP experiment needed less than 50 μL of samples, making this technique invaluable for compounds with limited availability. In addition, the sample dilution in this technique can alleviate the high absorption problem when the laser wavelength continues getting closer to the excitation frequency, or the laser path is long.

To conclude, we built a low field NSOR instrument and demonstrated a D-DNP NSOR measurement. We obtained a frequency coded NSOR signal in a single scan, which contained both nuclear and electronic excitation information. With the demonstration of single scan D-DNP NSOR, applications of the hybrid optical-NMR spectroscopy become reachable. Future developments based on this technique could lead to innovative optical-NMR spectroscopy that scans an NMR-UV 2D spectra. In such spectra, the nuclei position would be determined by frequency encoding of NMR, while the electronic transition close to a specific nucleus can be identified by varying the light wavelength.

REFERENCES

[1] Shi, J.; Ikäläinen, S.; Vaara, J.; Romalis, M. V. Observation of optical chemical shift by precision nuclear spin optical rotation measurements and calculations. *The Journal of Physical Chemistry Letters* **2013**, *4*, 437–441.

[2] Zhu, Y.; Hilty, C.; Savukov, I. Nuclear spin optical rotation. *eMagRes* **2019**, *8*, 205–214.

[3] Becker, E. D. A brief history of nuclear magnetic resonance. *Analytical Chemistry* **2012**, *65*, 295A–302A.

[4] Dang, H. B.; Maloof, A. C.; Romalis, M. V. Ultrahigh sensitivity magnetic field and magnetization measurements with an atomic magnetometer. *Applied Physics Letters* **2010**, *97*, 151110.

[5] Kominis, I. K.; Kornack, T. W.; Allred, J. C.; Romalis, M. V. A subfemtotesla multichannel atomic magnetometer. *Nature* **2003**, *422*, 596–599.

[6] Xu, S.; Donaldson, M. H.; Pines, A.; Rochester, S. M.; Budker, D.; Yashchuk, V. V. Application of atomic magnetometry in magnetic particle detection. *Applied Physics Letters* **2006**, *89*, 224105.

[7] Xu, S.; Crawford, C. W.; Rochester, S.; Yashchuk, V.; Budker, D.; Pines, A. Submillimeter-resolution magnetic resonance imaging at the Earth's magnetic field with an atomic magnetometer. *Physical Review A* **2008**, *78*, 013404.

[8] Savukov, I. M.; Romalis, M. V. NMR detection with an atomic magnetometer. *Physical Review Letters* **2005**, *94*, 123001.

[9] Hong, S.; Grinolds, M. S.; Pham, L. M.; Sage, D. L.; Luan, L.; Walsworth, R. L.; Yacoby, A. Nanoscale magnetometry with NV Centers in diamond. *MRS Bulletin* **2013**, *38*, 155–161.

[10] Acosta, V. M.; Bauch, E.; Ledbetter, M. P.; Santori, C.; Fu, K.-M. C.; Barclay, P. E.; Beausoleil, R. G.; Linget, H.; Roch, J. F.; Treussart, F.; Chemerisov, S.; Gawlik, W.; Budker, D. Diamonds with a high density of nitrogen-vacancy centers for magnetometry applications. *Physical Review B* **2009**, *80*, 115202.

[11] Shin, C. S.; Avalos, C. E.; Butler, M. C.; Trease, D. R.; Seltzer, S. J.; Peter Mustonen, J.; Kennedy, D. J.; Acosta, V. M.; Budker, D.; Pines, A.; Bajaj, V. S. Room-temperature operation of a radiofrequency diamond magnetometer near the shot-noise limit. *Journal of Applied Physics* **2012**, *112*, 124519.

[12] Hoult, D. I. Sensitivity of the NMR Experiment. *In eMagRes* **2007**, (eds R.K. Harris and R.L. Wasylishen).

[13] Suter, D. Optically enhanced magnetic resonance. *In eMagRes* **2007**, (eds R.K. Harris and R.L. Wasylishen).

[14] Warren, W. S.; Mayr, S.; Goswami, D.; West, A. P. Laser-enhanced NMR spectroscopy. *Science* **1992**, *255*, 1683–1685.

[15] Harris, R. A.; Tinoco, I. Laser-perturbed nuclear magnetic resonance spectroscopy and the conservation of parity. *The Journal of Chemical Physics* **1994**, *101*, 9289–9294.

[16] Evans, M. W. Optical phase conjugation in nuclear magnetic resonance: laser NMR spectroscopy. *The Journal of Physical Chemistry* **1991**, *95*, 2256–2260.

[17] Buckingham, A. D.; Parlett, L. C. High-resolution nuclear magnetic resonance spectroscopy in a circularly polarized laser beam. *Science* **1994**, *264*, 1748–1750.

[18] Savukov, I. M.; Lee, S.-K.; Romalis, M. V. Optical detection of liquid-state NMR. *Nature* **2006**, *442*, 1021–1024.

[19] Ledbetter, M. P.; Savukov, I. M.; Romalis, M. V. Nonlinear amplification of small spin precession using long-range dipolar interactions. *Physical Review Letters* **2005**,

94, 060801.

[20] Ledbetter, M. P.; Savukov, I. M.; Bouchard, L.-S.; Romalis, M. V. Numerical and experimental studies of long-range magnetic dipolar interactions. *The Journal of Chemical Physics* **2004**, *121*, 1454–1465.

[21] Meriles, C. A. Optical detection of NMR in organic fluids. *Concepts in Magnetic Resonance Part A* **2008**, *32A*, 79–87.

[22] Drude, P.; Millikan, R. A.; Mann, C. R. *The Theory of Optics*; Kessinger Publishing, LLC, 1902.

[23] Buckingham, A. D.; Stephens, P. J. Magnetic optical activity. *Annual Review of Physical Chemistry* **1966**, *17*, 399–432.

[24] Barron, L. D. *Molecular Light Scattering and Optical Activity*, 2nd ed.; Cambridge University Press, 2009.

[25] Haug, H.; Koch, S. W. *Quantum Theory of the Optical and Electronic Properties of Semiconductors: Fourth Edition*; World Scientific Publishing Company, 2004.

[26] Pagliero, D.; Dong, W.; Sakellariou, D.; Meriles, C. A. Time-resolved, optically detected NMR of fluids at high magnetic field. *The Journal of Chemical Physics* **2010**, *133*, 154505.

[27] Pagliero, D.; Meriles, C. A. Magneto-optical contrast in liquid-state optically detected NMR spectroscopy. *Proceedings of the National Academy of Sciences* **2011**, *108*, 19510–19515.

[28] Savukov, I.; Chen, H.-Y.; Karaulanov, T.; Hilty, C. Method for accurate measurements of nuclear-spin optical rotation for applications in correlated optical-NMR spectroscopy. *Journal of Magnetic Resonance* **2013**, *232*, 31–38.

[29] Zhu, Y.; Gao, Y.; Rodocker, S.; Savukov, I.; Hilty, C. Multi-nuclear detection of nuclear spin optical rotation at low field. *The Journal of Physical Chemistry Letters* **2018**, *9*, 3323–3327.

[30] Zavattini, E.; Zavattini, G.; Ruoso, G.; Raiteri, G.; Polacco, E.; Milotti, E.; Lozza, V.; Karuza, M.; Gastaldi, U.; Di Domenico, G.; Della Valle, F.; Cimino, R.; Carusotto, S.; Cantatore, G.; Bregant, M. New PVLAS results and limits on magnetically induced optical rotation and ellipticity in vacuum. *Physical Review D* **2008**, *77*, 032006.

[31] Pagliero, D.; Li, Y.; Fisher, S.; Meriles, C. A. Approach to high-frequency, cavity-enhanced Faraday rotation in fluids. *Applied Optics* **2011**, *50*, 648–654.

[32] Silver, J. A. Simple dense-pattern optical multipass cells. *Applied Optics* **2005**, *44*, 6545–6556.

[33] Li, S.; Vachaspati, P.; Sheng, D.; Dural, N.; Romalis, M. V. Optical rotation in excess of 100 rad generated by Rb vapor in a multipass cell. *Physical Review A* **2011**, *84*, 061403.

[34] Abragam, P. A.; Abragam, A. *The Principles of Nuclear Magnetism*; Clarendon Press, 1961.

[35] Kuhn, L. T., Ed. *Hyperpolarization Methods in NMR Spectroscopy*; Topics in Current Chemistry; Springer Berlin Heidelberg: Berlin, Heidelberg, 2013; Vol. 338.

[36] Walker, T. G.; Happer, W. Spin-exchange optical pumping of noble-gas nuclei. *Reviews of Modern Physics* **1997**, *69*, 629–642.

[37] Bargon, J.; Fischer, H. Kernresonanz-Emissionslinien während rascher Radikalreaktionen. *Zeitschrift für Naturforschung A* **1967**, *22*.

[38] Abragam, A.; Goldman, M. Principles of dynamic nuclear polarisation. *Reports on Progress in Physics* **1978**, *41*, 395–467.

[39] Natterer, J.; Bargon, J. Parahydrogen induced polarization. *Progress in Nuclear Magnetic Resonance Spectroscopy* **1997**, *31*, 293–315.

[40] Griffin, R. G.; Prisner, T. F. High field dynamic nuclear polarization—the renaissance. *Physical Chemistry Chemical Physics* **2010**, *12*, 5737.

[41] Nikolaou, P.; Coffey, A. M.; Walkup, L. L.; Gust, B. M.; Whiting, N.; Newton, H.; Barcus, S.; Muradyan, I.; Dabaghyan, M.; Moroz, G. D.; Rosen, M. S.; Patz, S.; Barlow, M. J.; Chekmenev, E. Y.; Goodson, B. M. Near-unity nuclear polarization with an open-source ^{129}Xe hyperpolarizer for NMR and MRI. *Proceedings of the National Academy of Sciences* **2013**, *110*, 14150–14155.

[42] Adams, R. W.; Aguilar, J. A.; Atkinson, K. D.; Cowley, M. J.; Elliott, P. I. P.; Duckett, S. B.; Green, G. G. R.; Khazal, I. G.; Lopez-Serrano, J.; Williamson, D. C. Reversible interactions with para-hydrogen enhance NMR sensitivity by polarization transfer. *Science* **2009**, *323*, 1708–1711.

[43] Ikäläinen, S.; Romalis, M. V.; Lantto, P.; Vaara, J. Chemical distinction by nuclear spin optical rotation. *Physical Review Letters* **2010**, *105*, 153001.

[44] Ikäläinen, S.; Lantto, P.; Vaara, J. Fully relativistic calculations of Faraday and nuclear spin-induced optical rotation in xenon. *Journal of Chemical Theory and Computation* **2012**, *8*, 91–98.

[45] Savukov, I. Nuclear-spin optical rotation in xenon. *Physical Review A* **2015**, *92*, 042514.

[46] Pennanen, T. S.; Ikäläinen, S.; Lantto, P.; Vaara, J. Nuclear spin optical rotation and Faraday effect in gaseous and liquid water. *The Journal of Chemical Physics* **2012**, *136*, 184502.

[47] Yao, G.-H.; He, M.; Chen, D.-M.; He, T.-J.; Liu, F.-C. Analytical theory of the nuclear-spin-induced optical rotation in liquids. *Chemical Physics* **2011**, *387*, 39–47.

[48] Buckingham, A. D.; Parlett, L. C. The effect of circularly polarized light on NMR spectra. *Molecular Physics* **1997**, *91*, 805–814.

[49] Lu, T.-T.; He, M.; Chen, D.-M.; He, T.-J.; Liu, F.-C. Nuclear-spin-induced optical Cotton–Mouton effect in fluids. *Chemical Physics Letters* **2009**, *479*, 14–19.

[50] Yao, G.-h.; He, M.; Chen, D.-m.; He, T.-j.; Liu, F.-c. New nuclear-spin-induced Cotton-Mouton effect in fluids at high DC magnetic field. *ChemPhysChem* **2012**, *13*, 1325–1331.

[51] Fu, L.-J.; Rizzo, A.; Vaara, J. Communication: Nuclear quadrupole moment-induced Cotton-Mouton effect in noble gas atoms. *The Journal of Chemical Physics* **2013**, *139*, 181102.

[52] Fu, L.-J.; Vaara, J. Nuclear spin-induced Cotton-Mouton effect in molecules. *The Journal of Chemical Physics* **2013**, *138*, 204110.

[53] Fu, L.-J.; Vaara, J. Nuclear quadrupole moment-induced Cotton-Mouton effect in molecules. *The Journal of Chemical Physics* **2014**, *140*, 024103.

[54] Fu, L.-J.; Vaara, J. Nuclear-spin-induced Cotton–Mouton effect in a strong external magnetic field. *ChemPhysChem* **2014**, *15*, 2337–2350.

[55] Vaara, J.; Rizzo, A.; Kauczor, J.; Norman, P.; Coriani, S. Nuclear spin circular dichroism. *The Journal of Chemical Physics* **2014**, *140*, 134103.

[56] Štěpánek, P.; Coriani, S.; Sundholm, D.; Ovchinnikov, V. A.; Vaara, J. Relation between molecular electronic structure and nuclear spin-induced circular dichroism. *Scientific Reports* **2017**, *7*, 46617.

[57] Ardenkjaer-Larsen, J. H.; Fridlund, B.; Gram, A.; Hansson, G.; Hansson, L.; Lerche, M. H.; Servin, R.; Thaning, M.; Golman, K. Increase in signal-to-noise ratio of > 10,000 times in liquid-state NMR. *Proceedings of the National Academy of Sciences* **2003**, *100*, 10158–10163.

[58] Günther, U. L. In *Modern NMR Methodology*; Heise, H., Matthews, S., Eds.; Topics in Current Chemistry; Springer: Berlin, Heidelberg, 2013; pp 23–69.

[59] Hilty, C.; Bowen, S. Applications of dynamic nuclear polarization to the study of reactions and reagents in organic and biomolecular chemistry. *Organic & Biomolecular Chemistry* **2010**, *8*, 3361.

[60] Bowen, S.; Hilty, C. Time-resolved dynamic nuclear polarization enhanced NMR spectroscopy. *Angewandte Chemie International Edition* **2008**, *47*, 5235–5237.

[61] Dzien, P.; Fages, A.; Jona, G.; Brindle, K. M.; Schwaiger, M.; Frydman, L. Following metabolism in living microorganisms by hyperpolarized ^{1}H NMR. *Journal of the American Chemical Society* **2016**, *138*, 12278–12286.

[62] Gal, M.; Mishkovsky, M.; Frydman, L. Real-time monitoring of chemical transformations by ultrafast 2D NMR spectroscopy. *Journal of the American Chemical Society* **2006**, *128*, 951–956.

[63] Zhu, Y.; Chen, C.-H.; Wilson, Z.; Savukov, I.; Hilty, C. Milli-tesla NMR and spectrophotometry of liquids hyperpolarized by dissolution dynamic nuclear polarization. *Journal of Magnetic Resonance* **2016**, *270*, 71–76.

[64] Espy, M. et al. Applications of ultra-low field magnetic resonance for imaging and materials studies. *IEEE Transactions on Applied Superconductivity* **2009**, *19*, 835–838.

[65] Korzhnev, D. M.; Kay, L. E. Probing invisible low-populated states of protein molecules by relxation dispersion NMR spectroscopy: An application to protein folding. *Accounts of Chemical Research* **2008**, *41*, 442–451.

[66] Skrynnikov, N. R.; Mulder, F. A. A.; Hon, B.; Dahlquist, F. W.; Kay, L. E. Probing Slow Time Scale Dynamics at Methyl-Containing Side Chains in Proteins by Relaxation Dispersion NMR Measurements: Application to Methionine Residues in a Cavity Mutant of T4 Lysozyme. *Journal of the American Chemical Society* **2001**, *123*, 4556–4566.

[67] Mulder, F. A. A.; Skrynnikov, N. R.; Hon, B.; Dahlquist, F. W.; Kay, L. E. Measurements of slow μs-ms time scale dynamics in protein side chains by ^{15}N relaxation dispersion NMR spectroscopy: Application to Asn and Gln residues in a cavity mutant of T4 lysozyme. *Journal of the American Chemical Society* **2001**,

123, 967–975.

[68] Callaghan, P. T.; Eccles, C. D.; Seymour, J. D. An earth's field nuclear magnetic resonance apparatus suitable for pulsed gradient spin echo measurements of self-diffusion under Antarctic conditions. *Review of Scientific Instruments* **1997**, *68*, 4263–4270.

[69] Callaghan, P.; Dykstra, R.; Eccles, C.; Haskell, T.; Seymour, J. A nuclear magnetic resonance study of Antarctic sea ice brine diffusivity. *Cold Regions Science and Technology* **1999**, *29*, 153–171.

[70] McDermott, R.; Trabesinger, A. H.; Mück, M.; Hahn, E. L.; Pines, A.; Clarke, J. Liquid-state NMR and scalar couplings in microtesla magnetic fields. *Science* **2002**, *295*, 2247–2249.

[71] Appelt, S.; Kühn, H.; Häsing, F. W.; Blümich, B. Chemical analysis by ultrahigh-resolution nuclear magnetic resonance in the Earth's magnetic field. *Nature Physics* **2006**, *2*, 105–109.

[72] Appelt, S.; Häsing, F. W.; Kühn, H.; Sieling, U.; Blümich, B. Analysis of molecular structures by homo- and hetero-nuclear J-coupled NMR in ultra-low field. *Chemical Physics Letters* **2007**, *440*, 308–312.

[73] Ledbetter, M. P.; Crawford, C. W.; Pines, A.; Wemmer, D. E.; Knappe, S.; Kitching, J.; Budker, D. Optical detection of NMR J-spectra at zero magnetic field. *Journal of Magnetic Resonance* **2009**, *199*, 25–29.

[74] Blanchard, J. W.; Ledbetter, M. P.; Theis, T.; Butler, M. C.; Budker, D.; Pines, A. High-resolution zero-field NMR J-spectroscopy of aromatic compounds. *Journal of the American Chemical Society* **2013**, *135*, 3607–3612.

[75] Hoult, D. I.; Bhakar, B. NMR signal reception: Virtual photons and coherent spontaneous emission. *Concepts in Magnetic Resonance* **1997**, *9*, 277–297.

[76] Xu, S.; Yashchuk, V. V.; Donaldson, M. H.; Rochester, S. M.; Budker, D.; Pines, A.

Magnetic resonance imaging with an optical atomic magnetometer. *Proceedings of the National Academy of Sciences* **2006**, *103*, 12668–12671.

[77] Budker, D.; Romalis, M. Optical magnetometry. *Nature Physics* **2007**, *3*, 227–234.

[78] Matlachov, A. N.; Volegov, P. L.; Espy, M. A.; George, J. S.; Kraus Jr., R. H. SQUID detected NMR in microtesla magnetic fields. *Journal of Magnetic Resonance* **2004**, *170*, 1–7.

[79] Zhang, W.; Ratcliffe, C. I.; Moudrakovski, I. L.; Mou, C.-Y.; Ripmeester, J. A. Distribution of gallium nanocrystals in Ga/MCM-41 mesocomposites by continuous-flow hyperpolarized ^{129}Xe NMR spectroscopy. *Analytical Chemistry* **2005**, *77*, 3379–3382.

[80] Zotev, V. S.; Owens, T.; Matlashov, A. N.; Savukov, I. M.; Gomez, J. J.; Espy, M. A. Microtesla MRI with dynamic nuclear polarization. *Journal of Magnetic Resonance* **2010**, *207*, 78–88.

[81] Armstrong, B. D.; Han, S. Overhauser dynamic nuclear polarization to study local water dynamics. *Journal of the American Chemical Society* **2009**, *131*, 4641–4647.

[82] Müller-Warmuth, W.; Meise-Gresch, K. Molecular motions and interactions as studied by dynamic nuclear polarization (DNP) in free radical solutions. *Advances in Magnetic and Optical Resonance* **1983**, *11*, 1–45.

[83] Bennati, M.; Luchinat, C.; Parigi, G.; Türke, M.-T. Water ^{1}H relaxation dispersion analysis on a nitroxide radical provides information on the maximal signal enhancement in Overhauser dynamic nuclear polarization experiments. *Physical Chemistry Chemical Physics* **2010**, *12*, 5902.

[84] Bowen, S.; Hilty, C. Rapid sample injection for hyperpolarized NMR spectroscopy. *Physical Chemistry Chemical Physics* **2010**, *12*, 5766–5770.

[85] Kaptein, R.; Dijkstra, K.; Tarr, C. A single-scan Fourier transform method for measuring spin-lattice relaxation times. *Journal of Magnetic Resonance* **1976**, *24*,

295–300.

[86] Freeman, R.; Hill, H. D. W. Fourier transform study of NMR spin–lattice relaxation by "progressive saturation". *The Journal of Chemical Physics* **1971**, *54*, 3367–3377.

[87] Miéville, P.; Jannin, S.; Bodenhausen, G. Relaxometry of insensitive nuclei: Optimizing dissolution dynamic nuclear polarization. *Journal of Magnetic Resonance* **2011**, *210*, 137–140.

[88] Kim, J.; Liu, M.; Chen, H.-Y.; Hilty, C. Determination of intermolecular interactions using polarization compensated heteronuclear overhauser effect of hyperpolarized spins. *Analytical Chemistry* **2015**, *87*, 10982–10987.

[89] Shin, C.; Kim, C.; Kolesov, R.; Balasubramanian, G.; Jelezko, F.; Wrachtrup, J.; Hemmer, P. R. Sub-optical resolution of single spins using magnetic resonance imaging at room temperature in diamond. *Journal of Luminescence* **2010**, *130*, 1635–1645.

[90] Theis, T.; Ganssle, P.; Kervern, G.; Knappe, S.; Kitching, J.; Ledbetter, M. P.; Budker, D.; Pines, A. Parahydrogen-enhanced zero-field nuclear magnetic resonance. *Nature Physics* **2011**, *7*, 571–575.

[91] Brentjens, M. A.; Bruyn, A. G. d. Faraday rotation measure synthesis. *Astronomy & Astrophysics* **2005**, *441*, 1217–1228.

[92] Crossley, W. A.; Cooper, R. W.; Page, J. L.; van Stapele, R. P. Faraday rotation in rare-earth iron garnets. *Physical Review* **1969**, *181*, 896–904.

[93] Warren, W. S.; Goswami, D.; Mayr, S. Laser enhanced NMR spectroscopy, revisited. *Molecular Physics* **1998**, *93*, 371–375.

[94] Gottardi, G.; Mesirca, P.; Agostini, C.; Remondini, D.; Bersani, F. A four coil exposure system (tetracoil) producing a highly uniform magnetic field. *Bioelectromagnetics* **2003**, *24*, 125–133.

[95] Graeme, J. G.; Graeme, J. *Photodiode Amplifiers: OP AMP Solutions*; McGraw

Hill Professional, 1996.

[96] Rice, F. A frequency-domain derivation of shot-noise. *American Journal of Physics* **2015**, *84*, 44–51.

[97] Štěpánek, P.; Kantola, A. M. Low-Concentration Measurements of Nuclear Spin-Induced Optical Rotation Using SABRE Hyperpolarization. *The Journal of Physical Chemistry Letters* **2019**, *10*, 5458–5462.

[98] Tayler, M. C. D.; Sakellariou, D. Low-cost, pseudo-Halbach dipole magnets for NMR. *Journal of Magnetic Resonance* **2017**, *277*, 143–148.

[99] Pretsch, E.; Bühlmann, P.; Affolter, C. In *Structure Determination of Organic Compounds: Tables of Spectral Data*; Pretsch, E., Bühlmann, P., Affolter, C., Eds.; Springer: Berlin, Heidelberg, 2000; pp 385–404.

[100] Drage, E. A.; Cahillane, P.; Hoffmann, S. V.; Mason, N. J.; Limão-Vieira, P. High resolution VUV photoabsorption cross section of dimethyl sulphoxide ($(CH_3)_2SO$). *Chemical Physics* **2007**, *331*, 447–452.

[101] Vathyam, S.; Lee, S.; Warren, W. S. Homogeneous NMR spectra in inhomogeneous fields. *Science* **1996**, *272*, 92–96.

[102] Warren, W. S.; Ahn, S.; Mescher, M.; Garwood, M.; Ugurbil, K.; Richter, W.; Rizi, R. R.; Hopkins, J.; Leigh, J. S. MR imaging contrast enhancement based on intermolecular zero quantum coherences. *Science* **1998**, *281*, 247–251.

[103] Santos, L.; Shlyapnikov, G. V.; Zoller, P.; Lewenstein, M. Bose-Einstein condensation in trapped dipolar gases. *Physical Review Letters* **2000**, *85*, 1791–1794.

[104] Giovanazzi, S.; Görlitz, A.; Pfau, T. Tuning the dipolar interaction in quantum gases. *Physical Review Letters* **2002**, *89*, 130401.

[105] Shi, J. Nuclear Spin Optical Rotation in Organic Liquids. Ph.D. thesis, Princeton University, 2013.